Architecture and Dynamics of Proteins and Aqueous Solvation Complexes

Architecture and Dynamics of Proteins and Aqueous Solvation Complexes

ACADEMISCH PROEFSCHRIFT

ter verkrijging van de graad van doctor
aan de Universiteit van Amsterdam
op gezag van de Rector Magnificus
prof. dr. D. C. van den Boom
ten overstaan van een door het college voor promoties
ingestelde commissie,
in het openbaar te verdedigen in de Agnietenkapel
op donderdag 19 november 2015, te 12:00 uur

door

Stephan Maria Lotze

geboren te Hildesheim, Duitsland

Promotiecommissie

promotor:	prof. dr. H. J. Bakker	Universiteit van Amsterdam
overige leden:	prof. dr. P. G. Bolhuis	Universiteit van Amsterdam
	prof. dr. W. J. Buma	Universiteit van Amsterdam
	prof. dr. K. J. Hellingwerf	Universiteit van Amsterdam
	prof. dr. A. F. Koenderink	Universiteit van Amsterdam
	dr. M. S. Pshenichnikov	Rijksuniversiteit Groningen
	prof. dr. P. Vöhringer	Universität Bonn

Faculteit der Natuurwetenschappen, Wiskunde en Informatica

ISBN 978-90-77209-94-3

The work described in this thesis was performed at the FOM-*Institute for Atomic and Molecular Physics* (AMOLF), Science Park 104, 1098 XG Amsterdam, The Netherlands. This work is part of the research programme of the *Stichting Fundamenteel Onderzoek der Materie* (FOM), which is financially supported by the *Nederlandse Organisatie voor Wetenschappelijk Onderzoek* (NWO).

Publications covered in this thesis

S. Lotze and H. J. Bakker. Influence of Förster-type energy transfer on the vibrational relaxation of anionic hydration shells. *J. Chem. Phys.* 139(4):044505, 2013 - *Chapter 4*

S. Lotze, C. C. M. Groot, C. Vennehaug and H. J. Bakker. Femtosecond Mid-Infrared Study of the Dynamics of Water Molecules in WaterAcetone and WaterDimethyl Sulfoxide Mixtures. *J. Phys. Chem. B* 119(16):5228-5239, 2015 - *Chapter 5*

S. Lotze, L. L. C. Olijve, I. K. Voets and H. J. Bakker. Observation of Vibrational Energy Exchange in a Type-III Antifreeze Protein. *J. Phys. Chem. B* 118(30):8962-8971, 2014 - *Chapter 6*

S. Lotze and H. J. Bakker. Structure and dynamics of a salt-bridge model system in water and DMSO. *J. Chem. Phys.* 142(21):212436, 2015 - *Chapter 7*

S. Lotze, J. Versluis, L. L. C. Olijve, L. van Schijndel, L. G. Milroy, I. K. Voets and H. J. Bakker. Observation of the absolute configuration of chiral molecules at aqueous interfaces. *Submitted - Chapter 8*

Other publications

T. H. van der Loop, M. R. Panman, S. Lotze, J. Zhang, T. Vad, H. J. Bakker, W. F. C. Sager and S. Woutersen. Structure and dynamics of water in nonionic reverse micelles: A combined time-resolved infrared and small angle x-ray scattering study. *J. Chem. Phys.* 137(4):044503, 2012

T. H. van der Loop, N. Ottosson, S. Lotze, E. Kentzinger, T. Vad, W. F. C. Sager, H. J. Bakker and S. Woutersen. Structure and dynamics of water in nanoscopic spheres and tubes. *J. Chem. Phys* 141(18):18C535, 2014

K. Meister, S. Strazdaite, A. L. DeVries, S. Lotze, L. L. C. Olijve, I. K. Voets, and H. J. Bakker. Observation of ice-like water layers at an aqueous protein surface. *Proc. Nat. Sci. U.S.A.* 111(50):1773217736, 2014

K. Meister, S. Lotze, L. L. C. Olijve, A. L. DeVries, J. G. Duman, I. K. Voets, and H. J. Bakker. Investigation of the Ice-Binding Site of an Insect Antifreeze Protein Using Sum-Frequency Generation Spectroscopy. *J. Phys. Chem. Lett.* 6(7):11621167, 2015

L. Liu, S. Lotze, H. J. Bakker. Vibrational Dynamics of the Bending Mode of Hydrated Protons in Nafion Membranes. *Submitted*

Contents

1 Introduction

1.1 Molecular structure and function

The conformation of molecules is a crucial factor in many aspects of live. For example, every living organism relies fundamentally on the correct functioning of complex macromolecules, which lie at the heart of the organism's cellular machinery. The replication of the genetic information encoded by deoxyribonucleic acid (DNA) is based on the interplay of several enzymes, two of the key steps of which are the unwinding of a double-stranded helix by the protein DNA helicase and the synthesis of a new strand by the DNA polymerase. For these reactions to occur in the correct manner, the involved proteins need to be in their functional conformation. Among the techniques most commonly employed as a probe of protein structure are nuclear magnetic resonance (NMR) spectroscopy and X-ray crystallography, both of which offer atomic resolution. Nearly 90% of all protein structures reported in the protein data base (www.pdb.org) have been obtained using x-ray crystallography. Since this experimental approach is based on the analysis of a diffraction pattern generated by the 3-dimensional periodic arrangements of a solid crystal, it necessarily provides only a static picture of molecules in the solid state. The conformational *dynamics*, i.e. the "jiggling and wiggling of atoms" (R.P. Feynman), cannot be tracked with this experimental approach. Although latest developments in the area of free electron lasers (FELs) have lead to the generation of ultrashort x-ray bursts and allowed to glimpse at the time-resolved changes in the diffraction pattern of a photosynthetic reaction center in response to an external trigger [1], this technique is still in its infancy and is applicable only to a limited range of samples. The atomic resolution of NMR-spectroscopy is accompanied by its applicability to liquid samples, which enables e.g. the study of biomolecules in a (near) native environment. NMR-spectroscopy also opens up the window to studies on time scales into the submicrosecond regime, allowing to monitor e.g. the transitions between conformational sub-states such as the switching between the open and closed states of enzymes [2]. Molecular processes, that occur on even faster time scales such as conformational fluctuations on nano- to picosecond time scales [3], are inaccessible to NMR-spectroscopy.

1.1.1 Hydrogen bonds and molecular conformation

Arguably the most important type of intermolecular interaction in the context of biological macromolecules is the formation of hydrogen bonds between XH..Y-groups as illustrated in Figure 1.1, where X and Y are elements with

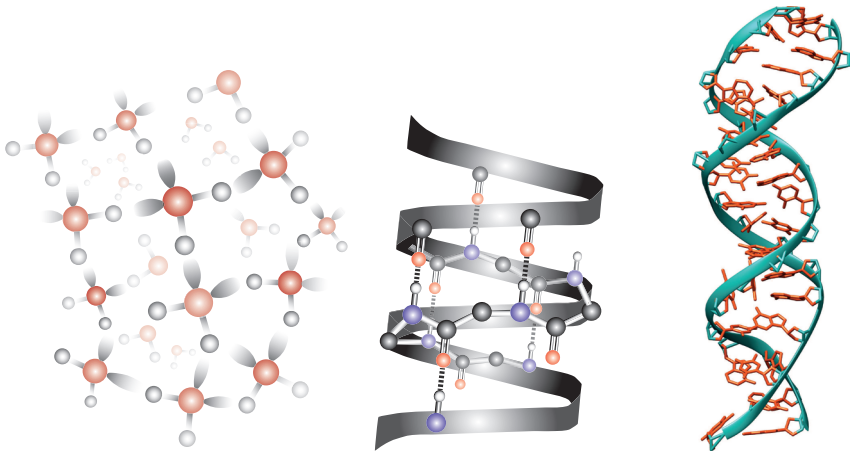

FIGURE 1.1. Structure of hydrogen bonded systems, left: the tetrahedral structure of water molecules in the condensed phase arising from the hydrogen bond interaction between OH-groups. Hydrogen bonding underlies also the formation of complex biomolecular structures such as protein α-helices shown in the middle and the DNA double helix shown on the right.

large electronegativity such as O,N,S or halides. The formation of secondary structural elements (α-helices, β-sheets) in proteins as well as the pairing of nucleobases in DNA is a direct result of the hydrogen-bonding interaction. The hydrogen-bonding interaction also lies at the heart of the unusual properties of water such as its maximum density at a temperature of 4°C. A sensitive spectroscopic marker for the hydrogen bond interaction in water and aqueous solutions is the hydroxyl stretch vibration (OH-vibration), whose spectroscopic line shape is a result of strong inhomogeneous broadening and reflects different hydrogen bond environments. Many of the dynamical processes such as the breaking and reformation of hydrogen bonds or the fluctuations around the equilibrium bond length and angle occur on femto- to picosecond timescales (10^{-12}-10^{-15}s). While these dynamical processes affect the line shapes of infrared marker modes such as the OH-vibration, they are not readily accessible to conventional absorption spectroscopy. Optical techniques based on femtosecond infrared light sources have made it possible to study these ultrafast processes in real time [4–14]. In these types of experiments, one or two intense infrared pulses are used to resonantly excite the hydroxyl stretch vibrations of water molecules and a time-delayed, weak probe pulse reports on the processes the ensemble of excited molecules has undergone during the time-interval between excitation and probe.

Intense infrared-active marker modes that are of particular relevance for the field of protein biochemistry are the vibrations of the protein backbone, in particular the amide I vibration that involves the displacement of the carbonyl group of the protein backbone. The resonance frequency and the spectroscopic

line shape of the amide I vibration are determined by the distinct hydrogen bonding patterns of protein secondary structural elements together with the solvent accessibility of the backbone. With ultrafast infrared experiments, structural and dynamic information on this vibrational mode has been obtained, which, in combination with residue-specific isotope labeling, has allowed for the development of models for the orientation and hydration pattern of membrane-associated peptides [15, 16]. The (sub-)picosecond molecular dynamics, on which these structural models are based, cannot be accessed by other types of spectroscopy and thus highlight the importance of ultrafast optical techniques.

1.1.2 Absolute configuration

An important aspect of molecular configuration is chirality, which is illustrated in Figure 1.2. If a molecule cannot be superposed on its mirror image, it is called chiral. The molecule and its mirror image are called enantiomers. Chirality is ubiquitous in biochemistry: peptides and proteins are built from chiral amino acids containing a stereogenic α-carbon atom[a], the L-enantiomer of which is the most prevalent form in nature. The chirality originating from a stereogenic carbon atom is translated to the macromolecular scale, which is encountered in e.g. poly-peptides, where L-amino acids form right-handed α-helices, whereas D-amino acids form left-handed helices. Interestingly, Linus Pauling in his first report of the structure of the α-helix [17] proposed a *left-handed* conformation, based on the (incorrect) assumption that proteins would contain D-amino acids. DNA (deoxyribonucleic acid), the carrier of genetic information in all living organisms, has in its most common form, termed B-DNA, a right-handed twist, which originates from the D-enantiomer of the sugar deoxyribose that forms its backbone [18][b]. The distinction between two enantiomers, i.e. the determination of their absolute configuration, has been a challenge for a long time, primarily because enantiomers exhibit the same physico-chemical properties in many aspects. Only few spectroscopic techniques are capable of distinguishing enantiomers. The first distinction was achieved in the 1950's, when Johannes Bijvoet and co-workers determined the absolute configuration of a tartrate-complex by means of anomalous x-ray scattering [20]. Since then, only few techniques have been added to the spectroscopic toolbox of stereochemists. Currently, the most commonly applied method to distinguish enantiomers of chiral molecules is to measure the weak difference in absorption of left and right circularly polarized light, referred to as circular dichroism. The development of new spectroscopic tools that combine the ability to distinguish between enantiomers with more detailed structural information is an active field of research [21–28], and over the past 10-20 year the usefulness of non-linear optical techniques to this purpose has been recognized and exploited [22–26].

[a] A carbon atom is referred to as stereogenic if it is tetrahedrally coordinated by four different substituents, making it impossible to overlay it with its mirror image

[b] It should be noted that also a left-handed form of DNA containing the D-enantiomer of deoxyribose is sometimes encountered in nature. This has been termed Z-DNA. [19]

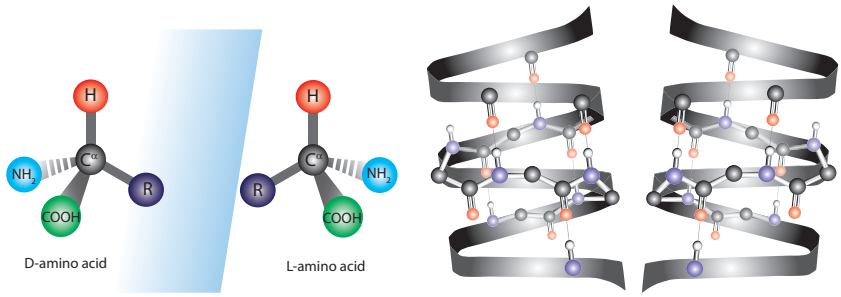

FIGURE 1.2. Examples of chirality: on the left the L- and D-enantiomers of amino acids, which possess an asymmetrically substituted C^{α}-atom and constitute a form of point chirality, are shown. On a macromolecular scale, the chirality of the amino acids translates into a well-defined handedness in the secondary structural elements of proteins such as α-helices shown on the right.

1.2 OUTLINE OF THIS THESIS

In the first part of Chapter 2 of this thesis, the theoretical foundation of the generation of femtosecond infrared pulses based on non-linear optical frequency conversion processes is laid out. In the second part of that chapter, the theory of light-matter interaction in a semi-classical description is developed. At the end of Chapter 2, molecular reorientation and the interaction (coupling) of vibrational modes are treated. In Chapter 3 the experimental setups, that have been used to collect the data for this thesis, are described. In Chapters 4 and 5 the molecular dynamics of water molecules are studied with time-resolved infrared pump-probe spectroscopy. In Chapter 4, the rate of resonant energy transfer between the hydroxyl groups (OH-groups) of water molecules and its dependence on intermolecular distances is determined. In Chapter 5, a comparative study of the vibrational relaxation and orientational dynamics of water molecules in two highly non-ideal mixtures, namely aqueous solutions of acetone and dimethylsulfoxide (DMSO), is presented. In Chapters 6, 7 and 8 we report on the structure and dynamics of complex biomolecules. In Chapter 6 the conformational fluctuations of a natural cryoprotectant molecule (antifreeze protein) are studied. In Chapter 7 a model system for salt-bridges, a ubiquitous structural motif in polypeptides, is investigated. In Chapter 8 a new technique that allows for the study of chirality at interfaces is introduced and applied to the left- and right-handed forms of an α-helical peptide.

2 Theory

2.1 Fundamentals of optics

The propagation of light in a non-magnetic ($\mu = 0$) medium without free charges ($\rho = 0$) is described by Maxwell's equations in the following form:

$$\nabla \cdot \vec{E} = \frac{\rho}{\epsilon_0} \ (A) \qquad \nabla \times \vec{E} + \frac{\partial \vec{B}}{\partial t} = 0 \quad (B) \tag{2.1}$$
$$\nabla \cdot \vec{B} = 0 \ (C) \qquad \nabla \times \frac{\vec{B}}{\mu_0} - \frac{\partial \vec{D}}{\partial t} = 0 \ (D)$$

Here, $\vec{E}$, $\vec{B}$, μ_0 and ϵ_0 denote the electric field strength in $\frac{V}{m}$, the magnetic flux density in $\frac{V \cdot s}{m^2}$, the free-space permeability in $\frac{V \cdot s}{A \cdot m}$ and the vacuum permittivity in $\frac{A \cdot s}{V \cdot m}$, respectively. Taking the curl of Eq. (2.1)D, exchanging the order of spatial and temporal derivatives, and making use of the vector identity $\nabla \times \nabla \times \vec{E} = \nabla(\nabla \cdot \vec{E}) - \nabla^2(\vec{E})$, we obtain the wave equation

$$\nabla^2 \vec{E} - \frac{1}{c^2} \frac{\partial^2 \vec{E}}{\partial t^2} = \mu_0 \frac{\partial^2 \vec{P}}{\partial t^2} \tag{2.2}$$

where $c = 1/\sqrt{\epsilon_0 \mu_0}$ denotes the speed of light in vacuum and $\vec{P}$ represents the macroscopic polarization that is induced by an electric field $\vec{E}$ in a medium. The polarization $\vec{P}$ that is generated in a medium by an external electric field $\vec{E}$ (oscillating with an angular frequency ω) is linked to this field by the frequency-dependent electric susceptibility $\overleftrightarrow{\chi}$[a]

$$\vec{P}(\omega) = \epsilon_0 \overleftrightarrow{\chi}(\omega) \vec{E}(\omega) \tag{2.3}$$

The superscript $\leftrightarrow$ denotes the fact that the electric susceptibility $\overleftrightarrow{\chi}$ is generally a tensorial quantity. In isotropic media, it reduces to a scalar quantity. The electric field $\vec{E}$ interacts with the bound charges in the material by displacing them, leading to induced dipoles, which in turn give rise to the macroscopic polarization that acts as a source term in Eq. (2.2). The solutions to Eq. (2.2) are given by plane waves of the form

$$\vec{E}(\omega, \vec{k}) = \vec{\mathcal{E}} e^{-i(\omega t - \vec{k}(\omega) \cdot \vec{r})} \tag{2.4}$$

[a] For the dielectric displacement we can write $\vec{D} = \epsilon_0 (1 + \overleftrightarrow{\chi}) \vec{E}$.

where ω and $\vec{k}$ denote the angular frequency and the wave-vector, respectively. The wave-vector $\vec{k}(\omega)$ inside a medium is related to the susceptibility $\chi(\omega)$ as

$$k^2(\omega)\frac{c^2}{\omega^2} = 1 + \chi(\omega) \tag{2.5}$$

and its real part determines the speed (phase velocity $v_p = \omega/\Re(k)$) with which a light field of frequency ω travels through the medium. Since the electric susceptibility is generally complex-valued $\chi(\omega) = \chi'(\omega) + i\chi(\omega)''$, the wave-vector can also have an imaginary component, which leads to attenuation of the light field during propagation. The extinction coefficient κ can be expressed in terms of the imaginary part of the susceptibility χ'' as

$$\chi'' = 2n\kappa \tag{2.6}$$

with $n = \sqrt{\epsilon_r}$ being the refractive index.

2.2 Nonlinear optics

In a typical experiment described in this thesis, pulsed laser sources with femtosecond pulse durations are used that create extremely high electric field strengths. To obtain an estimate for the magnitude of the electric field, we consider a pulse of 100 fs duration and 10 μJ pulse energy that is focussed into an approximately cylindrical spot with a diameter of 100 μm. This experimental geometry leads to a field strength on the order of 10^9 V/m. For comparison, the intensities which are typically encountered in e.g. commercial infrared absorption spectrometers are on the order of 10^2 V/m.[b] For the orders of magnitude higher field strengths generated by a (pulsed) laser source, the linear relation of Eq. (2.3) between the applied electric field $\vec{E}$ and the polarization generated in a material $\vec{P}$ is not valid anymore. Instead, we can express this relation by a power series expansion in the electric field $\vec{E}$:

$$\vec{P} = \epsilon_0(\overset{\leftrightarrow}{\chi}^{(1)}\vec{E} + \overset{\leftrightarrow}{\chi}^{(2)}\vec{E}^2 + \overset{\leftrightarrow}{\chi}^{(3)}\vec{E}^3 + ...) \tag{2.7}$$

The terms $\overset{\leftrightarrow}{\chi}^{(n)}$ with $n \geq 2$ are referred to as the nonlinear susceptibility. The electric polarization $\vec{P}$ in Eq. (2.7) can be separated into a term that scales linearly with the electric field and terms that are of higher order in the electric field $\vec{E}^n$:

$$\vec{P} = \vec{P}^{lin} + \vec{P}^{NL} \tag{2.8}$$

where the superscripts refer to linear and non-linear, respectively. Consequently, the wave-equation Eq. (2.2) can also be separated into a linear and a nonlinear part, which leads to the following relation between the electric field and the nonlinear polarization:

$$\nabla^2\vec{E} - \frac{\epsilon_r}{c^2}\frac{\partial^2\vec{E}}{\partial t^2} = \mu_0\frac{\partial^2\vec{P}^{NL}}{\partial t^2} \tag{2.9}$$

[b] See e.g. Newport product website for thermal (incoherent) mid-infrared lightsources http://www.newport.com/Silicon-Carbide-Light-Sources/377949/1033/info.aspx

with $\epsilon_r = 1 + \chi^{(1)}$. The nonlinear polarization $P^{\vec{N}L}$ acts as a source term that can lead to the generation of electric fields with frequencies other than those of the incoming fields. We will focus on the terms of 2^{nd} order. We will examine the case of two electric fields $\vec{E}_1$ and $\vec{E}_2$ of frequencies ω_1 and ω_2 impinging on a medium with a nonlinear susceptibility $\overset{\leftrightarrow}{\chi}^{(2)}$. The second-order polarization then contains the following terms:

$$\vec{P}(2\omega_1) = \overset{\leftrightarrow}{\chi}^{(2)} : \vec{E}_1(\omega_1)^2 \tag{2.10}$$

$$\vec{P}(2\omega_2) = \overset{\leftrightarrow}{\chi}^{(2)} : \vec{E}_2(\omega_2)^2 \tag{2.11}$$

$$\vec{P}(\omega_3 = \omega_1 - \omega_2) = \overset{\leftrightarrow}{\chi}^{(2)} : \vec{E}_1(\omega_1)\vec{E}_2^*(\omega_2) \tag{2.12}$$

$$\vec{P}(\omega_3 = \omega_1 + \omega_2) = \overset{\leftrightarrow}{\chi}^{(2)} : \vec{E}_1(\omega_1)\vec{E}_2(\omega_2) \tag{2.13}$$

$$\vec{P}(\omega_3 = 0) = \overset{\leftrightarrow}{\chi}^{(2)} : (\vec{E}_1(\omega_1)\vec{E}_1^*(\omega_1) + \vec{E}_2(\omega_2)\vec{E}_2^*(\omega_2)) \tag{2.14}$$

All of the above terms give rise to the emission of a third field $\vec{E}_3$ with frequency ω_3 and wave-vector $\vec{k}_3$, which must fulfil the condition $\omega_3 = \pm\omega_2 \pm \omega_1$. The first two equations represent the case of second harmonic generation (SHG), i.e. the generation of a light wave at twice the frequency of one of the incoming fields. The third and fourth equation describe sum and difference frequency generation, which lie at the heart of mid-infrared pulse generation described in Chapter 3 as well as vibrational sum-frequency generation (VSFG) spectroscopy reported in Chapter 8. The last equation describes a static electric polarization induced in the medium by the applied fields (optical rectification).

2.3 NONLINEAR FREQUENCY CONVERSION PROCESSES

Second-order non-linear processes can be used to generate mid-infrared pulses (λ = 3-6 μm) from the near-infrared pulses (λ = 800 nm) delivered by typical Titanium:sapphire laser systems. To describe the conversion process in non-linear optical crystals such as β-barium borate (β-BaB_2O_4, BBO), we write the electric fields $\vec{E}_1$ and $\vec{E}_2$ as harmonic plane waves $\vec{E}_i(\vec{r},t) = \vec{\mathcal{E}}_i(\vec{r})\, e^{i(\vec{k}_i\cdot\vec{r}-\omega_i t)} + c.c.$, where c.c. denotes the complex conjugate. Here, we have assumed monochromatic light fields, i.e. the use of continuous-wave lasers, which is why the field amplitude $\vec{\mathcal{E}}$ has no explicit time-dependence. The wave-equation Eq. (2.9) becomes

$$\nabla^2\vec{E} + \frac{\epsilon_r\omega^2}{c^2}\vec{E}(\vec{r}) = -\mu_0\omega^2\vec{P}^{NL} \tag{2.15}$$

The amplitudes of the electric fields $\vec{\mathcal{E}}_i(\vec{r})$ involved in the frequency conversion process vary over the distance that the nonlinear wave-interaction takes place and hence must be treated as a spatially dependent quantity. If one considers only the variation of the electric fields along the propagation direction

(z-axis), the vector fields $\vec{E}_i$ can be expressed as scalar fields $E_i(z)$ and the spatial derivative ∇^2 reduces to $\partial^2/\partial z^2$. We assume here that the amplitude $\mathcal{E}_i$ varies weakly over the distance that corresponds to one optical cycle, i.e. we assume $|\partial^2\mathcal{E}_i/\partial z^2| \ll |k_i\ \partial\mathcal{E}_i/\partial z|$, which is known as the slowly varying envelope approximation (SVEA). The rate of change of the electric field amplitude $\mathcal{E}$ for the case of sum-frequency generation ($\omega_3 = \omega_1 + \omega_2$) is given by

$$\frac{\partial\mathcal{E}_3}{\partial z} = -\frac{\mu_0\omega_3^2}{2ik_3}\chi^{(2)}\mathcal{E}_1\mathcal{E}_2\ e^{i(k_1+k_2-k_3)z} \tag{2.16}$$

where we have expressed the non-linear polarization in Eq. (2.15) as

$$P^{NL}(\omega_3 = \omega_1 + \omega_2) = \chi^{(2)}\mathcal{E}_1\mathcal{E}_2\ e^{i(k_1+k_2)z}e^{-i(\omega_1+\omega_2)t} \tag{2.17}$$

The corresponding expressions for the amplitudes of the electric fields at ω_1 and ω_2 are given by

$$\begin{aligned}\frac{\partial\mathcal{E}_2}{\partial z} &= -\frac{\mu_0\omega_2^2}{2ik_2}\chi^{(2)}\mathcal{E}_3\mathcal{E}_1^*\ e^{i(k_3-k_1-k_2)z} \\ \frac{\partial\mathcal{E}_1}{\partial z} &= -\frac{\mu_0\omega_1^2}{2ik_1}\chi^{(2)}\mathcal{E}_3\mathcal{E}_2^*\ e^{i(k_3-k_2-k_1)z}\end{aligned} \tag{2.18}$$

The factor $k_1 + k_2 - k_3 = \Delta k$ in the exponential of Eq. (2.16) is known as the phase-mismatch between the nonlinear polarization and the generated electric field. It is generally non-zero due to the refractive index dispersion of the medium, thus setting an upper limit to the distance over which the new wave of frequency ω_3 can efficiently be generated. This distance $l_c = \pi/\Delta k$ is often termed the coherence length. To achieve a high conversion efficiency, it is crucial to minimize the phase-mismatch. Otherwise, the wavefront of the field at ω_3 generated at a certain point z in the medium by the nonlinear polarization will acquire a phase shift of π with respect to the wavefront generated at another spot $z' = z + l_c$. Since the total energy stored in the three interacting fields is conserved, the inversion of the nonlinear frequency conversion process implies that energy from the wave ω_3 is converted back to ω_1 and ω_2. A simple way to overcome this limitation is the use of birefrigent crystals. By choosing the correct polarization of the light fields and the correct crystal orientation, the refractive indices of the waves can be adjusted such that the phase-match condition $k_1 + k_2 = k_3$ is fulfilled.

2.3.1 PULSED LIGHT SOURCES

A detailed derivation of the description of non-linear frequency conversion processes driven by pulsed light fields can be found in Ref. [29] and only the final result will be reproduced here. The extension to pulsed light fields can be done by writing the electric fields $E(z,t)$ in terms of their Fourier-integrals

$$E(z,t) = \int \widetilde{\mathcal{E}}(\omega+\eta)\ e^{i(kz-(\omega+\eta)t)}\ d\eta + c.c. \tag{2.19}$$

with $\widetilde{\mathcal{E}}(\omega)$ as the pulse-envelope in the frequency domain, and the dielectric displacement as

$$D(z,t) = \int \epsilon(\omega+\eta)\widetilde{\mathcal{E}}(\omega+\eta)\; e^{i(kz-(\omega+\eta)t)}\; d\eta + c.c. \tag{2.20}$$

The frequency-dependence of the dielectric constant $\epsilon(\omega)$ is accounted for by assuming that it varies only weekly over the bandwidth of the pulses such that $\epsilon(\omega+\eta) \approx \epsilon(\omega) + \eta\, \frac{\partial \epsilon}{\partial \omega}$. After neglecting terms with η^n with $n \geq 2$, one arrives at the modified version of Eq. (2.16) for a sum-frequency generation process, driven by pulsed-light fields

$$\Big(\frac{\partial}{\partial z} + \frac{1}{v_{3g}}\frac{\partial}{\partial t}\Big)\mathcal{E}_3 = -\frac{\mu_0\omega_3^2}{2ik_3}\chi^{(2)}\mathcal{E}_1\mathcal{E}_2\; e^{i\Delta kz} \tag{2.21}$$

with $v_g = (\frac{\partial k}{\partial \omega})^{-1}$ being the group velocity of the light pulse. In a dispersive medium, the group velocities v_g of the involved light fields are in general not the same, which results in a temporal walk-off between the pulse envelopes of the interacting fields. This aspect limits the maximally achievable bandwidth of the newly generated fields. To illustrate this, we will consider the case of optical parametric amplification that is employed e.g. in the conversion of the 800 nm pulses delivered from a Titanium:sapphire laser into two lower frequency components termed signal and idler. If we let the index i denote the fields (1 pump, 2 signal, 3 idler) and let $\delta\omega_i$ denote the frequency bandwidth of the i^{th} light fields, the conditions of energy and momentum conservation can be written as

$$\delta\omega_1 = \delta\omega_2 + \delta\omega_3 \qquad \delta k_1 = \delta k_2 + \delta k_3 \tag{2.22}$$

We can re-write these relations using $\delta k_i \approx \delta\omega_i \frac{\partial k_i}{\partial \omega} = \delta\omega_i\,(v_{ig})^{-1}$ to obtain the following relations for the bandwidth of the generated signal (2) and idler (3) fields:

$$\delta\omega_2 = q_2\delta\omega_1 \qquad \delta\omega_3 = q_3\delta\omega_1 \tag{2.23}$$

where $q_2 = \frac{1/(v_{1g})-1/(v_{3g})}{1/(v_{2g})-1/(v_{3g})}$ and $q_3 = 1 - q_2 = \frac{1/(v_{2g})-1/(v_{1g})}{1/(v_{2g})-1/(v_{3g})}$. From this expression, it becomes apparent that a large group velocity mismatch (GVM, $1/(v_{2g}) - 1/(v_{3g})$) between the signal and idler fields is detrimental for the bandwidth $\delta\omega_2$ and $\delta\omega_3$ of both pulses. The largest bandwidth of signal and idler pulses can thus be achieved when operating the optical parametric amplifier close to degeneracy and for type I phase-matching conditions, i.e. similar frequencies and polarization directions for signal and idler fields.

2.4 Resonant light-matter interaction

The description in the previous section is appropriate to describe parametric frequency conversion processes in lossless (non-absorbing) media. This implicitly assumes that the response of the medium is instantaneous and only persists for the duration of the light pulses. This assumption does not hold when the incoming light pulses are in resonance with a transition in the medium such as a vibrational transition. In this case, the response of the medium has a non-zero duration and can even be substantially longer than the duration of the applied electric fields. To describe the resonant interaction between a medium and a light field, a semiclassical treatment can be employed that describes the medium quantum-mechanically, but treats the electric fields classically, as in the preceding section. We will start by considering that the force that is exerted on a molecule by an external electric field is typically much weaker than the binding forces within a molecule. In this case, we can express the interaction of a molecule with an external light field as a weak, time-dependent perturbation and write a Hamiltonian of the form

$$\hat{H} = \hat{H}_0 + \hat{V}_{em}(t) \tag{2.24}$$

Here, $\hat{H}_0$ denotes the time-independent molecular system hamiltonian. The term $\hat{V}_{em} = -\vec{\hat{\mu}} \cdot \vec{E}(t)$ describes the interaction of a molecule with a quasi-monochromatic light field of the form $\vec{E} = \vec{E_0}\ \cos(\omega t)$ with $\vec{\hat{\mu}}$ being the electric dipole operator. Approximating the light-matter interaction as purely dipolar in nature is based on the assumption that the spatial variation of the electric field over the molecule is negligibly small. This is true as long as the wavelength of the electric field is much larger than the size of the molecule. For infrared light with wavelengths $\lambda = 3$ - 6 μm interacting with molecules the size of several Å, this forms a good approximation. Therefore higher order terms in the interaction can be neglected. In order to be able to calculate the influence of a time-dependent perturbation, we assume that we know the eigenstates of the static part of the hamiltonian $\hat{H}_0$ and their corresponding energy eigenvalues. In reality, $\hat{H}_0$ will have an extremely complicated form even for a simple triatomic molecule such as water, as $\hat{H}_0$ includes in its full form the description of all electronic, nuclear, rotational and translational degrees of freedom of the molecule as well as the coupling between these degrees of freedom. We will consider the very simplified situation where $\hat{H}_0$ describes a two-level system with states $|1\rangle$ and $|2\rangle$ (which we will later extend to include also the second excited state). The associated energy eigenvalues will be denoted as ϵ_1, ϵ_2 and the transition frequency between the two states as $\omega_{12} = (\epsilon_2 - \epsilon_1)/\hbar$.

2.4.1 Optical Bloch equations

To describe the time-evolution of the system under the influence of an external perturbation, we start from the time-dependent Schrödinger equation

$$i\hbar \frac{\partial |\psi(t)\rangle}{\partial t} = \hat{H}|\psi(t)\rangle \tag{2.25}$$

where $\hat{H}$ denotes the hamiltonian given by Eq. (2.24), and write the wave-function $|\psi(t)\rangle$ in the basis of eigenfunctions of $\hat{H}_0$ such that $|\psi(t)\rangle = c_1(t)|1\rangle + c_2(t)|2\rangle$. Here, we use the notation $c_1(t)|1\rangle = C_1(t)e^{-i\epsilon_1 t/\hbar}|1\rangle$, where $C_i(t)$ denotes a complex amplitude. Differentiation of Eq. (2.25) and its complex conjugate leads directly to the expression

$$i\hbar\frac{dc_1(t)}{dt} = \sum_{k=1}^{2} H_{1k}c_k(t) \tag{2.26}$$

$$i\hbar\frac{dc_2^*(t)}{dt} = -\sum_{k'=1}^{2} c_{k'}^*(t)H_{k'2} \tag{2.27}$$

where H_{nm} denotes a matrix with elements of the form $\langle n|\hat{H}|m\rangle$. Merging the above expression, we obtain

$$i\hbar(c_2^*\frac{dc_1}{dt} + c_1\frac{dc_2^*}{dt}) = i\hbar\frac{d(c_1c_2^*)}{dt} = \sum_{k=1}^{2} H_{1k}c_kc_2^* - \sum_{k'=1}^{2} c_1c_{k'}^*H_{k'2} \tag{2.28}$$

If we define a matrix ρ with elements $\rho_{nm} = c_nc_m^*$, we can rewrite Eq. (2.28) as

$$i\hbar\frac{d(c_1c_2^*)}{dt} = i\hbar\frac{d\rho_{12}}{dt} = (H\rho - \rho H)_{12} \tag{2.29}$$

or more generally

$$i\hbar\frac{d(c_nc_m^*)}{dt} = i\hbar\frac{d\rho_{nm}}{dt} = (H\rho - \rho H)_{nm} \tag{2.30}$$

This matrix ρ is called the density matrix, and we can identify the diagonal entries $\rho_{11} = |c_1|^2$ and $\rho_{22} = |c_2|^2$ as the populations of the states $|1\rangle$ and $|2\rangle$, i.e. the probability of finding the system in the states $|1\rangle$ and $|2\rangle$, respectively. The off-diagonal entries $\rho_{12} = c_1c_2^* = C_1C_2^*\,e^{i(\epsilon_2-\epsilon_1)t/\hbar}$ and $\rho_{21} = c_2c_1^* = C_2C_1^*\,e^{-i(\epsilon_2-\epsilon_1)t/\hbar}$ describe to what extent a fixed phase-relation (*a coherence*) between the wave-functions of state $|1\rangle$ and $|2\rangle$ exists.
Letting the operator associated with the matrix ρ_{mn} be represented by $\hat{\rho} = |\psi\rangle\langle\psi|$[c] and introducing the commutator of two operators as $[\hat{A},\hat{B}] = [\hat{A}\hat{B}-\hat{B}\hat{A}]$, we can rewrite Eq. (2.30) as

$$i\hbar\frac{d\hat{\rho}}{dt} = [\hat{H},\hat{\rho}] \tag{2.32}$$

This equation is known as the Liouville-von-Neumann equation. It describes the time-evolution of the density operator $\hat{\rho}$ and its matrix elements ρ_{nm}. We

[c] One can verify that this is equivalent to the definition introduced in Eq. (2.29) by expressing $|\psi\rangle$ in a given set of basis functions and evaluating the expression for an element ρ_{nm}

$$\rho_{nm} = \langle n|\psi\rangle\langle\psi|m\rangle = \sum_{n',m'} c_{n'}^*c_{m'}\langle n|m'\rangle\langle n'|m\rangle = c_n\langle n|n\rangle c_m^*\langle m|m\rangle = c_nc_m^* \tag{2.31}$$

will see that it provides a convenient way of calculating expectation values of operators.
In order to calculate the macroscopic polarization P given by $P = N\langle\mu\rangle$ with N being the number density of induced dipoles from the quantum-mechanical equations, we need to calculate the expectation value of the dipole moment operator $\langle\mu\rangle = \langle\psi|\vec{\hat{\mu}}|\psi\rangle$. To that end, we first write the static and the time-varying parts of the total hamiltonian in Eq. (2.24) in terms of the eigenfunctions of $\hat{H}_0$ as

$$\hat{H}_0 = \epsilon_1(|1\rangle\langle 1|) + \epsilon_2(|2\rangle\langle 2|) \tag{2.33}$$

$$\hat{V}_{em} = -\vec{\hat{\mu}} \cdot \vec{E}(t)\,(|1\rangle\langle 2| + |2\rangle\langle 1|) \tag{2.34}$$

In matrix representation, we directly obtain

$$H_0 = \begin{pmatrix} \epsilon_1 & 0 \\ 0 & \epsilon_2 \end{pmatrix} \quad , \quad V_{em} = \begin{pmatrix} 0 & -\vec{\mu}_{12} \cdot \vec{E}(t) \\ -\vec{\mu}_{21} \cdot \vec{E}(t) & 0 \end{pmatrix} \tag{2.35}$$

where $\vec{\mu}_{12}$ denotes $\langle 1|\vec{\hat{\mu}}|2\rangle$. We can now use the density matrix to obtain an expression for $\langle\mu\rangle$:

$$\langle\psi|\vec{\hat{\mu}}|\psi\rangle = \sum_{m,n} c_m^* c_n \langle m|\vec{\hat{\mu}}|n\rangle = \sum_{m,n} \rho_{nm}\mu_{mn} = \sum_n (\rho\mu)_{nn} = \mathrm{Tr}(\rho\mu) \tag{2.36}$$

where Tr denotes the trace of the matrix. Combining Eqs. (2.35) and (2.36), one sees that the expectation value of the dipole operator $\langle\vec{\hat{\mu}}\rangle$ is related to the off-diagonal elements ρ_{12} and ρ_{21} of the density matrix:

$$\langle\hat{\mu}\rangle = \mathrm{Tr}(\rho\mu) = \mu_{12}\rho_{21} + \mu_{21}\rho_{12} \tag{2.37}$$

The time-dependence of these off-diagonal elements can be calculated with the help of the Liouville-von-Neumann equation Eq. (2.32) together with Eq. (2.35), and we arrive at the following expression

$$\frac{d\rho}{dt} = \begin{pmatrix} \frac{i}{\hbar}\vec{\mu} \cdot \vec{E}(t)(\rho_{21} - \rho_{12}) & -\frac{i}{\hbar}\vec{\mu} \cdot \vec{E}(t)(\rho_{11} - \rho_{22}) + i\omega_{12}\,\rho_{12} \\ \frac{i}{\hbar}\vec{\mu} \cdot \vec{E}(t)(\rho_{11} - \rho_{22}) - i\omega_{12}\,\rho_{21} & \frac{i}{\hbar}\vec{\mu} \cdot \vec{E}(t)(\rho_{12} - \rho_{21}) \end{pmatrix} \tag{2.38}$$

where we have written $\vec{\mu}_{12} = \vec{\mu}_{21} = \vec{\mu}$.

PERTURBATIVE EXPANSION OF THE DENSITY MATRIX In order to describe effects such as transient absorption changes observed in pump-probe experiments, we need to go beyond interactions that are linear in the electric field $\vec{E}$. To that end, we expand the density matrix perturbatively in powers of electric field, i.e. we write for the electric field $\vec{E} = \lambda\vec{E}$ and ρ as a power series of the form

$$\rho = \rho^{(0)} + \lambda\rho^{(1)} + \lambda^2\rho^{(2)} + ... \tag{2.39}$$

where λ constitutes a parameter with values ranging between 0 and 1 that describes the strength of the interaction. If we perform this expansion for the matrix elements in Eq. (2.38), we arrive after collecting terms of equal power in λ, at the following expression for the time-dependence of the elements of the density matrix in n^{th}-order:

$$\frac{d}{dt}\rho_{12}^{(n)} = -\frac{i\vec{\mu}\cdot\vec{E}(t)}{\hbar}(\rho_{11}^{(n-1)} - \rho_{22}^{(n-1)}) + i\omega_{12}\,\rho_{12}^{(n)} \tag{2.40}$$

$$\frac{d}{dt}\rho_{21}^{(n)} = \frac{i\vec{\mu}\cdot\vec{E}(t)}{\hbar}(\rho_{11}^{(n-1)} - \rho_{22}^{(n-1)}) - i\omega_{12}\,\rho_{21}^{(n)} \tag{2.41}$$

$$\frac{d}{dt}\rho_{11}^{(n)} = \frac{i\vec{\mu}\cdot\vec{E}(t)}{\hbar}(\rho_{21}^{(n-1)} - \rho_{12}^{(n-1)}) \tag{2.42}$$

$$\frac{d}{dt}\rho_{22}^{(n)} = \frac{i\vec{\mu}\cdot\vec{E}(t)}{\hbar}(\rho_{12}^{(n-1)} - \rho_{21}^{(n-1)}) \tag{2.43}$$

If we define $\widetilde{\rho}_{12} = \rho_{12}e^{-i\omega t}$ (and $\widetilde{\rho}_{21} = \rho_{21}e^{i\omega t}$) and rewrite the electric field as $\vec{E}(t) = \frac{1}{2}(\vec{E}_0(t)e^{-i\omega t} + \vec{E}_0^*(t)e^{i\omega t})$ with $\vec{E}_0(t)$ denoting the pulse-envelope in the time-domain, we can write for the time-dependence of the density matrix for a two-level system

$$\frac{d}{dt}\widetilde{\rho}_{12}^{(n)} = -\frac{i\vec{\mu}\cdot\vec{E}_0^*(t)}{2\hbar}(\rho_{11}^{(n-1)} - \rho_{22}^{(n-1)}) - i(\omega-\omega_{12})\,\widetilde{\rho}_{12}^{(n)} \tag{2.44}$$

$$\frac{d}{dt}\widetilde{\rho}_{21}^{(n)} = \frac{i\vec{\mu}\cdot\vec{E}_0(t)}{2\hbar}(\rho_{11}^{(n-1)} - \rho_{22}^{(n-1)}) + i(\omega-\omega_{12})\,\widetilde{\rho}_{21}^{(n)} \tag{2.45}$$

$$\frac{d}{dt}\widetilde{\rho}_{11}^{(n)} = \frac{i\vec{\mu}}{2\hbar}(\vec{E}_0^*\widetilde{\rho}_{21}^{(n-1)} - \vec{E}_0\widetilde{\rho}_{12}^{(n-1)}) \tag{2.46}$$

$$\frac{d}{dt}\widetilde{\rho}_{22}^{(n)} = \frac{i\vec{\mu}}{2\hbar}(\vec{E}_0\widetilde{\rho}_{12}^{(n-1)} - \vec{E}_0^*\widetilde{\rho}_{21}^{(n-1)}) \tag{2.47}$$

where we have made the rotating wave approximation, i.e. we have neglected rapidly oscillating terms such as $e^{\pm i2\omega t}$ since those will contribute only negligibly after integration.
The above equations are known as the optical Bloch equations that describe the time-evolution of a two-level systems under the influence of a classical light field. We focus first on the off-diagonal elements, since these are related to the polarization of the medium. Eq. (2.44) constitutes an inhomogeneous differential equation that can be solved by variation of constants. Doing so, one obtains

$$\widetilde{\rho}_{12}^{(3)}(t) = \int_{-\infty}^{t} -\frac{i\vec{\mu}\vec{E}_0^*(t')}{2\hbar}(\rho_{11}^{(2)}(t') - \rho_{22}^{(2)}(t'))e^{-i(\omega-\omega_{12})(t-t')}dt' \tag{2.48}$$

$$\widetilde{\rho}_{21}^{(3)}(t) = \int_{-\infty}^{t} \frac{i\vec{\mu}\vec{E}_0(t')}{2\hbar}(\rho_{11}^{(2)}(t') - \rho_{22}^{(2)}(t'))e^{i(\omega-\omega_{12})(t-t')}dt' \tag{2.49}$$

The integrand describes the phase-evolution of frequency components ω of the electric field relative to the resonance frequency ω_{12} of the system. Working

back in the perturbation expansion, we obtain for the diagonal elements of the density matrix in 2nd order:

$$\rho_{11}^{(2)}(t) = \int_{-\infty}^{t} -\frac{i\vec{\mu}}{2\hbar}(\vec{E}_0^*(t')\widetilde{\rho}_{21}^{(1)}(t') - \vec{E}_0(t')\widetilde{\rho}_{12}^{(1)}(t'))dt' \tag{2.50}$$

$$\rho_{22}^{(2)}(t) = \int_{-\infty}^{t} -\frac{i\vec{\mu}}{2\hbar}(\vec{E}_0(t')\widetilde{\rho}_{12}^{(1)}(t') - \vec{E}_0^*(t')\widetilde{\rho}_{21}^{(1)}(t'))dt' \tag{2.51}$$

For the off-diagonal element $\rho_{21}^{(1)}$ in the above equation, we can write:

$$\widetilde{\rho}_{12}^{(1)}(t) = \int_{-\infty}^{t} -\frac{i\vec{\mu}\vec{E}_0^*(t')}{2\hbar}(\rho_{11}^{(0)}(t') - \rho_{22}^{(0)}(t'))e^{-i(\omega-\omega_{12})(t-t')}dt' \tag{2.52}$$

$$\widetilde{\rho}_{21}^{(1)}(t) = \int_{-\infty}^{t} \frac{i\vec{\mu}\vec{E}_0(t')}{2\hbar}(\rho_{11}^{(0)}(t') - \rho_{22}^{(0)}(t'))e^{i(\omega-\omega_{12})(t-t')}dt' \tag{2.53}$$

The term $(\rho_{11}^{(0)} - \rho_{22}^{(0)})$ is the population difference between the ground and the excited state before any interactions with the electric fields has taken place. For most molecular vibrations at room temperature $\widetilde{\rho}_{22}^{(0)} \approx 0$. From the above equations, we can understand the following pathways through the density matrix:

- The interactions $\widetilde{\rho}_{11}^{(0)} \xrightarrow{\vec{E}_0} \widetilde{\rho}_{21}^{(1)}$ and $\widetilde{\rho}_{11}^{(0)} \xrightarrow{\vec{E}_0^*} \widetilde{\rho}_{12}^{(1)}$ are excitations of the *ket* and the *bra*, respectively, leading to the generation of new off-diagonal elements (*coherences*)

- The interactions $\widetilde{\rho}_{12}^{(1)} \xrightarrow{\vec{E}_0} \widetilde{\rho}_{22}^{(2)}$ and $\widetilde{\rho}_{21}^{(1)} \xrightarrow{\vec{E}_0^*} \widetilde{\rho}_{22}^{(2)}$ are excitations of the *ket* and the *bra*, respectively, leading to the generation of new diagonal elements (*populations*)

- The interaction $\widetilde{\rho}_{21}^{(1)} \xrightarrow{\vec{E}_0^*} \widetilde{\rho}_{11}^{(2)}$ and $\widetilde{\rho}_{12}^{(1)} \xrightarrow{\vec{E}_0} \widetilde{\rho}_{11}^{(2)}$ are de-excitations of the *ket* and the *bra*, respectively, leading to the generation of new diagonal elements (*populations*)

- The interactions $\widetilde{\rho}_{11}^{(2)} \xrightarrow{\vec{E}_0} \widetilde{\rho}_{21}^{(3)}$ and $\widetilde{\rho}_{22}^{(2)} \xrightarrow{\vec{E}_0} \widetilde{\rho}_{21}^{(3)}$ are excitation of the *ket* and de-excitation of the *bra*, respectively, leading to the generation of new off-diagonal elements (*coherences*)

- The interactions $\widetilde{\rho}_{11}^{(2)} \xrightarrow{\vec{E}_0^*} \widetilde{\rho}_{12}^{(3)}$ and $\widetilde{\rho}_{22}^{(2)} \xrightarrow{\vec{E}_0^*} \widetilde{\rho}_{12}^{(3)}$ are excitation of the *bra* and de-excitation of the *ket*, respectively, leading to the generation of new off-diagonal elements (*coherences*)

We can summarize this as follows:

- An interaction with a field $\vec{E}$ either excites a *ket* or de-excites a *bra*
- An interaction with a field $\vec{E}^*$ either excites a *bra* or de-excites a *ket*
- An odd number of interactions is required to generate off-diagonal elements
- An even number of interactions is required to generate new diagonal elements

2.4.2 PUMP-PROBE SPECTROSCOPY OF TWO- AND THREE-LEVEL SYSTEMS

We specify the electric field as the sum of pump (pu) and probe (pr) fields and account also for their propagation directions by including the wave-vectors

$$\begin{aligned}\vec{E}(\vec{r},t) = (\vec{E}_{pu,0}(\vec{r},t)\, e^{-i\omega t + i\vec{k}_{pu}\cdot\vec{r}} + \vec{E}^*_{pu,0}(\vec{r},t)\, e^{+i\omega t - i\vec{k}_{pu}\cdot\vec{r}}) \\ +(\vec{E}_{pr,0}(\vec{r},t)\, e^{-i\omega t + i\vec{k}_{pr}\cdot\vec{r}} + \vec{E}^*_{pr,0}(\vec{r},t)\, e^{+i\omega t - i\vec{k}_{pr}\cdot\vec{r}})\end{aligned} \tag{2.54}$$

where we have assumed both fields to have the same frequency components. Each interaction with an electric field thus imprints a factor $e^{\pm i\vec{k}\cdot\vec{r}}$ on the generated 3^{rd}-order polarization. In a pump-probe experiment, the generated polarization $P^{(3)}$ results from two interactions with the pump field and thus the generated signal can in principle carry any of the wave-vector combinations given by $\vec{k}_s = \pm\vec{k}_{pu} \pm \vec{k}_{pu} \pm \vec{k}_{pr}$. By measuring changes in the transmission of the probe-pulse, we implicitly select a signal with $\vec{k}_s = \vec{k}_{pu} - \vec{k}_{pu} + \vec{k}_{pr} = \vec{k}_{pr}$, corresponding to a pathway generated by interactions with the fields $\vec{E}_{pu}$, $\vec{E}^*_{pu}$ and $\vec{E}_{pr}$. We let the time at which the interaction of the system with a field $\vec{E}$ or $\vec{E}^*$ occurs be denoted by t'_1, t'_2, t'_3. We will consider the case that the pump pulse interacts with the sample first, i.e. we enforce the following time-ordering of interactions:

- $\vec{E}_{pr}(t'_3)\vec{E}_{pu}(t'_2)\vec{E}^*_{pu}(t'_1)$
- $\vec{E}_{pr}(t'_3)\vec{E}^*_{pu}(t'_2)\vec{E}_{pu}(t'_1)$

with $t'_3 > t'_2 > t'_1$. The different pathways that fulfil the above time-ordering and contribute to a 3^{rd}-order signal with $\vec{k}_s = \vec{k}_{pr}$ can be illustrated in the form of Feynman-diagrams as shown in Figure 2.1. In this diagrammatic notation, an arrow pointing to the right represents an electric field $\vec{E}$ carrying a phase-factor $e^{-i\omega t + i\vec{k}\cdot\vec{r}}$, and an arrow pointing to the left represents the complex conjugate $\vec{E}^*$ with $e^{+i\omega t - i\vec{k}\cdot\vec{r}}$. An arrow pointing towards the diagram represents excitation, an arrow away de-excitation or emission. Let us consider the first diagram of Figure 2.1(top left): the system is initially described by an equilibrium density matrix containing only diagonal elements until the first interaction with the electric field $\vec{E}_{pu}$ at time t'_1, which leads to creation of the off-diagonal element $\widetilde{\rho}^{(1)}_{21}$ according to Eqn. (2.53). This is indicated by the notation $|2\rangle\langle 1|$ and the system is said to be in a *coherence* state until the next interaction with an electric field at time t'_2. The interaction with $\vec{E}^*_{pu}$ at t'_2 creates a new diagonal element $\widetilde{\rho}^{(2)}_{11}$ according to Eq. (2.50). The time-interval $t'_3 - t'_2$ until the third interaction represents the experimentally controlled pump-probe delay. During this time-interval population relaxation can occur. The third electric field interaction at time t'_3, resulting from the probe field $\vec{E}_{pr}$, generates again an off-diagonal element $\widetilde{\rho_{21}}^{(3)}$. We see from Eqn. (2.49) that the field being emitted as a result of this 3^{rd}-order polarization reports

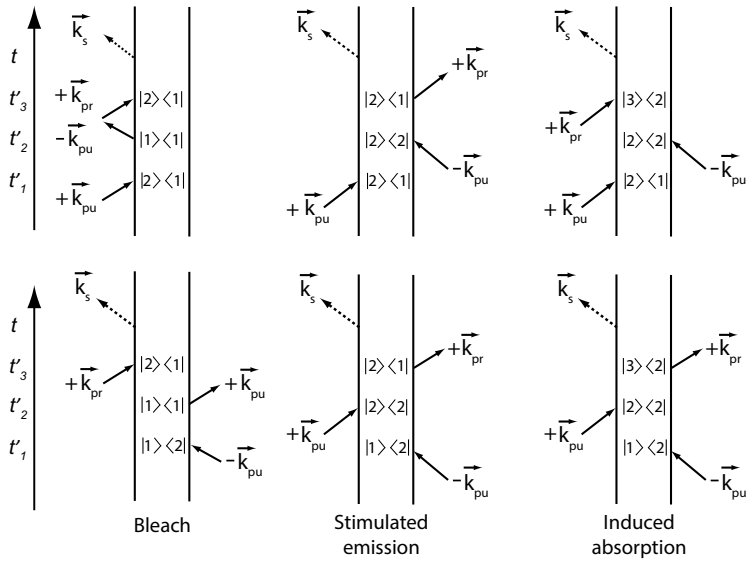

FIGURE 2.1. Pathways through the density matrix describing a two-level system illustrated by Feynman-diagrams. The time points at which the system interacts with the electric fields of pump or probe pulses are denoted by t'_1, t'_2, t'_3. The diagrams that give rise to emission of a signal at time t in the direction $\vec{k}_s = \vec{k}_{pr}$ are shown. It is assumed that the pump pulse interacts with the system before the probe pulse and that the pulse envelopes have only negligible overlap in time. The top row represents the *non-rephasing* diagrams, where the off-diagonal elements $\widetilde{\rho}_{12}$ and $\widetilde{\rho}_{21}$ of the density matrix acquire a phase during the time interval $(t - t'_3)$ that is the same as the one acquired during $(t'_2 - t'_1)$. The lower row represents the *rephasing* diagrams, corresponding to the opposite phase-evolution during the time intervals $(t'_2 - t'_1)$ and $(t - t'_3)$.

on the population differences present in the system at the time that these are interrogated by the probe pulse and thus allows to follow vibrational relaxation processes in time.

In a pump-probe experiment, we have no experimental control over the time-interval $(t'_2 - t'_1)$, and we cannot control if the interaction with $\vec{E}_{pu}$ or $\vec{E}^*_{pu}$ comes first. We see from Figures 2.1 that the order of interactions $\vec{E}_{pr}(t'_3)\vec{E}_{pu}(t'_2)\vec{E}^*_{pu}(t'_1)$ give rise to off-diagonal elements in the density matrix that acquire a phase during the time interval $(t - t'_3)$ that is opposite to the one acquired during $(t'_2 - t'_1)$. These pathways are usually referred to as *rephasing* pathways. The upper row in Figure 2.1 shows that the pathway $\vec{E}_{pr}(t'_3)\vec{E}^*_{pu}(t'_2)\vec{E}_{pu}(t'_1)$ gives rise to off-diagonal elements that acquire the same phase during the time intervals $(t-t'_3)$ and $(t'_2-t'_1)$. These pathways are usually referred to as *non-rephasing* pathways. While in a pump-probe experiment always the sum of all contributing pathways is measured, other implementations of 3^{rd}-order non-linear spectroscopy such as 2- or 3-pulse photon-echo

experiments allow to selectively measure rephasing or non-rephasing diagrams. The systems usually encountered in infrared pump-probe spectroscopy, i.e. anharmonic oscillators, are better described as a 3-level system. We therefore need to include transitions to the second excited state, denoted here as $|3\rangle$. These transitions give rise to two additional diagrams shown on the right side of Figure 2.1. As will be shown in Section 2.5, for an anharmonic oscillator the transition $|2\rangle \rightarrow |3\rangle$ is red-shifted with respect to the fundamental transition $|1\rangle \rightarrow |2\rangle$, and these two new diagrams thus give rise to a red-shifted induced absorption that becomes only possible after population has been prepared in the first excited state by two preceding field interactions. In contrast, the diagrams in the left and the middle column of Figure 2.1 create a signal at the fundamental transition frequency of an oscillator, and result from the bleaching, i.e. the decreased absorption due to reduced ground state population, and the stimulated emission from the first excited state.

THE EMITTED SIGNAL In the diagrams of Figure 2.1, the emission of the field originating from $P^{(3)}$ is represented by a dashed arrow. We can use Eqs. (2.48)-(2.53) and Eq. (2.36) to calculate the n-th order non-linear polarization as

$$P^{(n)}(t) = N\langle\hat{\mu}\rangle = N\,\mathrm{Tr}(\hat{\rho}^{(n)}\hat{\mu}) \tag{2.55}$$

Eq. (2.55) together with the wave equation Eq. (2.9), provide a complete description for the electric field that is detected in a 3^{rd}-order nonlinear optical spectroscopy such as pump-probe, 2D-IR and photon-echo experiments. The pump-induced absorption changes that are measured by the probe pulse can be seen as resulting from the interference between $\vec{E}_{pr}$ and the electric field radiated by the 3^{rd}-order polarization $P^{(3)}$. It can be shown that the experimentally observed, pump-induced absorption change in a pump-probe experiment is given by

$$\Delta\alpha = -\log_{10}\Big(\frac{I_{pr}}{I^{\circ}_{pr}}\Big) \approx -\log_{10}\Big(\Im\frac{P^{(3)}E_{pr}}{E_{pr}E^{*}_{pr}}\Big) \tag{2.56}$$

where I_{pr} and I°_{pr} denote the intensity of the probe pulse in the presence and absence of the pump field, respectively.
We see that taking the trace in Eq. (2.55) adds another factor of $\vec{\mu}$ so that the total 3^{rd}-order response (polarization) scales with $\vec{\mu}^4$. In contrast, a first-order polarization obtained from Eq. (2.55) scales with $\vec{\mu}^2$. Since the absorption cross-section is related to the transition dipole moment as $\sigma \propto |\vec{\mu}|^2$, the important consequence arises that *linear* optical phenomena such as absorption scale linearly with the absorption cross-section σ, but a non-linear, 3^{rd}-order signal scales with σ^2. This scaling allows to e.g. observe pump-probe spectra of strongly absorbing chromophores ($\sigma_{solute} \gg \sigma_{solvent}$) in strongly dilute solutions ($c_{solute} \ll c_{solvent}$) with very small background signal from the solvent, as the 3^{rd}-order response in a pump-probe experiment is given by $c\sigma^2$. In contrast, the absorption band of this chromophore in the linear spectrum may be of sim-

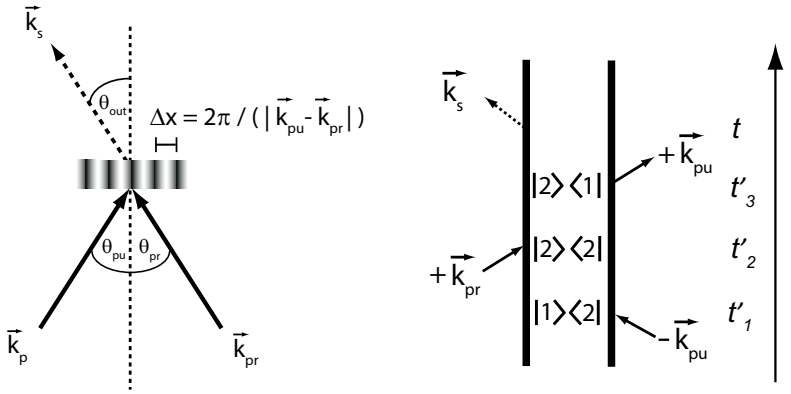

FIGURE 2.2. Coherent artifact arising from the interaction of the sample with the light fields in the order *pump-probe-pump*. If pump and probe pulses overlap in time, the interference between the two light fields results in a spatial intensity (and hence excitation) modulation in the sample with a periodicity of $\Delta x = 2\pi/|\vec{k}_{pu} - \vec{k}_{pr}| = \lambda_{pu}/2\sin\theta_{pu}$, where it is assumed that both beams have the same angle of incidence ($\theta_{pu} = \theta_{pr}$). The electric field radiated by the 3^{rd}-order polarization can be viewed as the pump pulse that is diffracted off this population grating in the direction $\vec{k}_s = \vec{k}_{pr}$. This can be seen when considering the condition for the first order diffraction peak formed by a grating with periodicity Δx given by $\Delta x(\sin\theta_{pu} + \sin\theta_{out}) = \lambda_{pu}$, which is fulfilled for $\theta_{out} = \theta_{pr}$. The coherent artifact thus leads to an additional signal emitted into the direction of the probe pulse, as long as pump and probe pulses overlap in time. One of in total three Feynman-diagrams contributing to this signal is shown on the right. The other diagrams can be found e.g. in Ref. [30].

ilar amplitude or even smaller than the solvent bands due to the overwhelming presence of solvent molecules, as the first-order signal scales as $c\sigma$.

ARTIFACTS Additional pathways need to be considered if the pump and probe pulses overlap in time and interaction of the system with light fields in the order *pump-probe-pump* can occur. These pathways constitute an unwanted artifact during the time that the envelopes of pump and probe pulses overlap in time, arising from the finite duration of these pulses. When pump and probe beams with wave-vectors $\vec{k}_{pu}$ and $\vec{k}_{pr}$, respectively, are crossed in the sample and overlap in time, they create an interference pattern in the sample characterized by a periodicity of $\Delta x = 2\pi/(|\vec{k}_{pu} - \vec{k}_{pr}|)$. This periodic intensity variation translates into a spatially dependent excitation probability, i.e. a spatial variation in the population difference $(\rho^{(2)}_{11} - \rho^{(2)}_{22})$ across the sample. This is often referred to as a population grating, and it can be shown that the 3^{rd}-order field arising from this time-ordering is emitted in the same direction as if it were the result of the pump pulse being diffracted off this population grating, as illustrated in Figure 2.2. The effect, often called the *coherent artifact*, gives rise to an additional absorption change during the time-overlap of pump and probe pulses, that does *not* reflect population relaxation [31, 32]. Hence, care

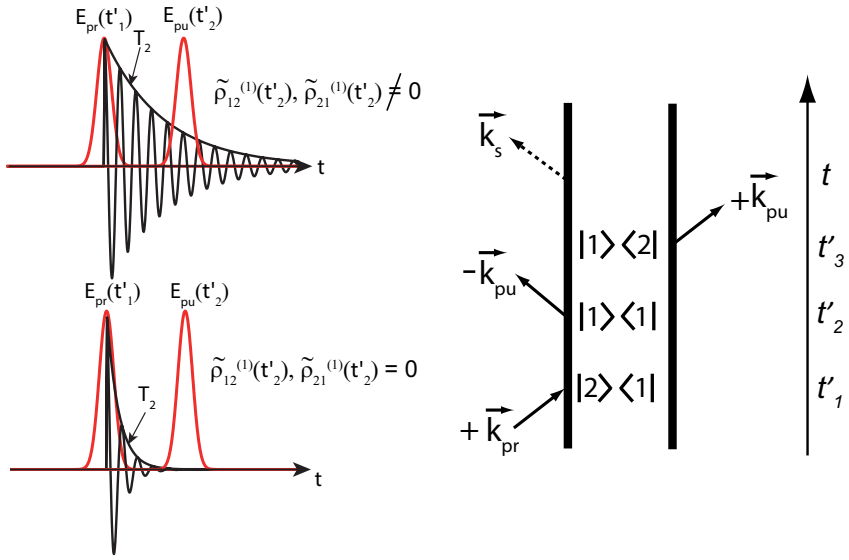

FIGURE 2.3. Perturbed free induction decay arising from the interaction of the sample with the light fields in the order *probe-pump-pump*. If the probe pulse precedes the pump pulse and the dephasing time T_2 is long compared to the pulse durations, a non-zero first-order polarization associated with the off-diagonal elements $\tilde{\rho}_{12}^{(1)}$ and $\tilde{\rho}_{21}^{(1)}$ is present already in the sample at the time that the pump pulse enters it. New diagonal elements of second order ($\rho_{11}^{(2)}, \rho_{22}^{(2)}$) given by Eq. (2.50) will thus be generated and, after another interaction with the pump field, give rise to a non-zero 3^{rd}-order polarization and thus to a change of the emission in the probe direction for *negative* delay times. In the case of rapid dephasing as schematically outlined below, the polarization has completely decayed at the time that the pump pulse interacts with the system ($\tilde{\rho}_{12}^{(1)}, \tilde{\rho}_{21}^{(1)} = 0$) and no third-order signal is generated at negative delay times. One of in total three Feynman-diagrams illustrating the origin to this signal is shown on the right. The other diagrams can be found e.g. in Ref. [30].

has to be taken when analyzing the transient absorption changes around time delay zero of a pump-probe experiment.

An additional 3^{rd}-order signal can be observed for spectrally narrow resonances. If the dephasing time T_2 of a transition, which is approximately given by the inverse line width of the absorption band, is long compared to the duration of the light pulses, the signal generated by the time-ordering *probe-pump-pump* needs to be accounted for. In that case, a non-zero transient absorption change can be observed at *negative* delay times, i.e. before the pump pulse excites the sample. This feature has been termed the *perturbed free induction decay* and is the result of the presence of non-zero off-diagonal elements in the density matrix induced by the probe at the time at which the pump-pulse interacts with the sample (t'_2). It leads to a signal at negative delay times that rises approximately

with the dephasing time T_2 of the transition [33, 34]. Its origin is schematically outlined in Figure 2.3.

2.4.3 LINE SHAPES IN THE CONDENSED PHASE

In the condensed phase, molecules that are described by the hamiltonian $\hat{H}_0$ are typically strongly interacting with the surrounding molecules. Hence, the system-part of the hamiltonian $\hat{H}_0$ is not only dependent on the intramolecular coordinates, but also on the dynamics of the surrounding molecules (*the bath*), the coordinates of which we collectively write as Q and consequently $\hat{H}_0 = \hat{H}_0(Q)$. Additionally, the system and bath dynamics may be coupled to each other and hence terms of the form $\hat{H}_{SB}(Q, q)$, that depend on both system and bath coordinates, need to be included in $\hat{H}_0$. Besides irreversible relaxation of a light-induced excitation, these couplings can lead to a modulation of the transition frequency ω_{12} monitored in a pump-probe experiment that reflects the randomly fluctuating forces exerted by the bath on the vibrational oscillator. These modulations are called spectral diffusion processes.
We can define a frequency-frequency correlation function (FFCF) as $C_{\omega_{12}\omega_{12}}(t) = \langle \delta\omega_{12}(\mathrm{t{=}0})\delta\omega_{12}(t)\rangle$, where we define $\langle\omega_{12}\rangle = \omega_{12} + \langle\delta\omega_{12}\rangle$, to describe the modulation of the transition frequency. The correlation function $C_{\omega_{12}\omega_{12}}(t)$ is often assumed to decay exponentially in time:

$$C_{\omega_{12}\omega_{12}}(t) = \Delta_s \, e^{-t/\tau_c} \tag{2.57}$$

where Δ_s represents the width of the frequency distribution and τ_c represents a characteristic decay time-constant. We will illustrate the effect of a fluctuating bath on the spectroscopic line shape by considering the linear absorption spectrum, which is obtained from the Fourier-transform of the first-order polarization response. For an ensemble of oscillators with a randomly fluctuating transition frequency $\omega_{12}(t)$, we can write

$$S(\omega) \propto FT\Big\{\Big\langle e^{-i\int_0^t \omega_{12}(t')dt'} e^{-t/2T_1}\Big\rangle\Big\} \tag{2.58}$$

$$= FT\Big\{\Big\langle e^{-i\omega_{12}t} e^{-i\int_0^t \delta\omega_{12}(t')dt'} e^{-t/2T_1}\Big\rangle\Big\} \tag{2.59}$$

where FT denotes the Fourier transform and $\Big\langle ... \Big\rangle$ denotes an ensemble average over all oscillators. The finite lifetime $\mathrm{T_1}$ of the upper state gives rise to a non-zero line width $1/(2\pi T_1)$ (in units of 1/s) even in the absence of any frequency modulation processes, an effect that is called lifetime broadening. It can be shown [35, 36] that if the fluctuations in the transition frequency ω_{12} are the result of many statistically independent processes, Eq. (2.58) can be approximated by the introduction of the line shape function $g(t)$, which is related to the FFCF by $g(t) = \frac{1}{2}\int_0^t d\tau' \int_0^t d\tau'' \langle\delta\omega_{12}(\tau'')\delta\omega_{12}(\tau')\rangle$. Writing out the integration explicitly leads to

$$g(t) = \Delta_s^2\tau_c^2(e^{-t/\tau_c} + \frac{t}{\tau_c} - 1) \tag{2.60}$$

The linear absorption spectrum can then be rewritten as

$$S(\omega) \propto FT\Big\{e^{-i\omega_{12}t}e^{-g(t)}e^{-t/2T_1}\Big\} \tag{2.61}$$

Eq. (2.61) is simply a different way of writing the ensemble averaged phase-fluctuations that are accumulated over time as described by the factor $e^{-i\int_0^t \omega_{12}(t')dt'}$ in Eq. (2.58). Depending on the time-scales on which the modulations occur, we can distinguish two limiting cases:

- For $\Delta_s\tau_c \gg 1$, Eq. (2.60) reduces to $g_{inhom}(t) = \frac{\Delta_s^2 t^2}{2}$, which can be seen by expanding the exponential up to second order. Δ_s reflects a degree of inhomogeniety that is not changing on the time-scale of the experiment, and this functional form of the line shape function $g(t)$ leads to a *Gaussian* distribution of frequencies in Eq. (2.61). This is termed the *inhomogeneous* limit.

- In the case of rapid frequency modulations ($\Delta_s\tau_c \ll 1$), Eq. (2.60) reduces to $g_{hom}(t) = \Delta_s^2\tau_c t$, which leads to a purely exponential decay in Eq. (2.61) and hence a *Lorentzian* line shape function after Fourier transformation. This is called the *homogeneous* limit and the decay time $\mathrm{T}_2 = 1/(\Delta_s^2\tau_c)$ is called the homogeneous lifetime.

It is worth noting that in the homogeneous limit the line width $1/(\pi T_2) = \Delta_s^2\tau_c/\pi$ (in 1/s) is *narrower* than the actual frequency distribution Δ_s. This seemingly counterintuitive effect can be understood from the following considerations: if oscillators in the experimentally probed ensemble experience slow frequency fluctuations (characterized by a long correlation time τ_c), they will quickly acquire a significant phase-difference, leading to a loss of mutual coherence between them (dephasing). In contrast, if these modulations of the resonance frequencies are very short lived (short τ_c), the oscillators tend (on average) towards the center frequency of the distribution Δ_s and get less rapidly out of phase with each other, thus leading to a slower dephasing process and a *narrower* linewidth. This is reflected in the inverse scaling of the dephasing time T_2 with the correlation time τ_c.

2.5 VIBRATIONAL COUPLINGS

The vibrational modes of a molecule are often described as independent harmonic oscillators but this is in fact a very crude approximation. To realistically model the vibrational dynamics of a molecule, the interaction with other vibrational modes within the same molecule (intramolecular couplings) as well as the interactions with other molecules in spatial proximity need to be accounted for. These interactions include mechanical couplings between different molecular vibrations, the coupling to low-frequency modes such as hydrogen-bond vibrations, as well as electrostatic interactions between the (transition) dipoles. While in a purely harmonic system, the restoring force scales linearly with the displacement of the oscillator from its equilibrium position, for most molecular vibrations this is a good approximation only at small displacements. A realistic potential has a dissociation limit and a restoring force that decreases as the oscillator displacement increases. This can be incorporated with a vibrational hamiltonian of the form $\hat{H}_{vib} = \hat{T}_{kin} + \hat{V}_{pot}(\hat{q}_i)$, with $\hat{V}_{pot}(\hat{q}_i)$ denoting the potential energy, that includes terms that are of third or higher order in the position (operator) such as $\hat{q}_1^3$, $\hat{q}_1^4$, $\hat{q}_1^2\hat{q}_2$, $\hat{q}_1^2\hat{q}_2^2$. In the following, we will first introduce a set of operators (ladder operators) that provide a convenient way to describe the effect of anharmonic couplings and then apply these to the specific case of quartic anharmonicity and two near-resonantly coupled, anharmonic oscillators.

2.5.1 LADDER OPERATORS

If we let $|n\rangle$ denote the n^{th} eigenstate of a harmonic oscillator, we can introduce the operators $\hat{a}$ and $\hat{a}^\dagger$ as

$$\hat{a} = \frac{1}{\sqrt{2}}\left(\sqrt{\frac{m\omega}{\hbar}}\hat{q} + i\,\frac{\hat{p}}{\sqrt{m\omega\hbar}}\right) \qquad \hat{a}^\dagger = \frac{1}{\sqrt{2}}\left(\sqrt{\frac{m\omega}{\hbar}}\hat{q} - i\,\frac{\hat{p}}{\sqrt{m\omega\hbar}}\right)$$

where m and ω represent the reduced mass and the resonance frequency of the harmonic oscillator. It can be shown that they fulfil the following relations

$$\begin{aligned} \hat{a}^\dagger|n\rangle &= \sqrt{(n+1)}|n+1\rangle \\ \hat{a}|n\rangle &= \sqrt{(n)}|n-1\rangle \end{aligned} \tag{2.62}$$

The operators $\hat{a}^\dagger$ and $\hat{a}$ have thus been termed creation and annihilation operators or ladder operators. We can now express the momentum and position operators $\hat{p}$ and $\hat{q}$ in terms of these new operators as

$$\hat{p} = \sqrt{\frac{m\omega\hbar}{2}}\left(\frac{\hat{a} - \hat{a}^\dagger}{i}\right) \qquad \hat{q} = \sqrt{\frac{\hbar}{2m\omega}}\left(\hat{a} + \hat{a}^\dagger\right) \tag{2.63}$$

The hamiltonian of a harmonic oscillator $\hat{H}_{HO}$ can thus be written as

$$\hat{H}_{HO} = \hbar\omega\Big(\hat{a}^\dagger\hat{a} + \frac{1}{2}\hat{\mathcal{I}}\Big) \tag{2.64}$$

with $\hat{\mathcal{I}}$ being the identity operator. The equivalence of Eq. (2.64) with the more common definition of the harmonic oscillator hamiltonian $\hat{H} = \frac{\hat{p}^2}{2m} + \frac{1}{2}m\omega^2\hat{q}^2$ can be easily seen by inserting Eq. (2.63) into this expression and making use of the commutation relation $[\hat{q}, \hat{p}] = i\hbar\hat{\mathcal{I}}$, where $\hat{\mathcal{I}}$ denotes the identity operator.[d]

2.5.2 The quartic anharmonic oscillator

We now wish to investigate how the introduction of anharmonicity into the potential energy operator $\hat{V}_{pot}$ affects the energy levels of an oscillator. In the following, we will use the numbering $|0\rangle$, $|1\rangle$, $|2\rangle$ ... to denote the ground state, the first, and the second excited state of the oscillator, respectively. We will cover the case of a quartic anharmonicity term ($k_4\hat{q}^4$) and explicitly calculate the first order correction to the n^{th}energy levels of the oscillator. We can write this correction as

$$\Delta E_n^{(1)} = E_n^{(0)} - E_n^{(1)} = k_4\langle n|\hat{q}^4|n\rangle \tag{2.65}$$

Using Eq. (2.63), it is apparent that we can replace $\hat{q}$ by a term proportional to $(\hat{a} + \hat{a}^\dagger)$. Writing out Eq. (2.65) leads to an expression that includes a sum over terms of the form $\hat{a}^n(\hat{a}^\dagger)^m$ with $m + n = 4$. We can simplify this expression by noting that only terms with $m = n = 2$ are energy conserving, i.e. the number of quanta of excitation equals the number of annihilated quanta and thus energy conservation is fulfilled. Collecting all terms $\hat{a}^n(\hat{a}^\dagger)^m$ with $m = n = 2$ and making repeated use of Eq. (2.62), we arrive at an expression for the energy shift to first order:

$$\Delta E_n^{(1)} = \frac{k_4\hbar^2}{4m^2\omega^2}\Big(6n^2 + 6n + 3\Big) \tag{2.66}$$

where m and ω denote the reduced mass and the resonance frequency of the (harmonic) oscillator, respectively. We see that as a consequence of including an anharmonic term in $\hat{V}_{pot}(\hat{q}_i)$ the eigenvalues of $\hat{H}_{vib}$ are no longer equally spaced as in the case of a strictly harmonic potential. Classically, this can be understood as a restoring force that depends on the amplitude of the displacement and, as we have reasoned in the beginning of this section, the restoring forces become weaker as the oscillator displacement becomes large. Consequently, the force constant k_4 has a *negative* sign and so has $\Delta E_n^{(1)}$. This has the important consequence that the eigenvalues of the *anharmonic* hamiltonian $\hat{H} = \frac{\hat{p}^2}{2m} + \frac{1}{2}m\omega^2\hat{q}^2 + k_4\hat{q}^4$ converge with increasing quantum number. This results in a transition frequency from the first to the second vibrationally excited state ($|1\rangle \rightarrow |2\rangle$) which is shifted to lower frequencies compared to the fundamental transition frequency ($|0\rangle \rightarrow |1\rangle$). This unequal spacing of the energy levels of an anharmonic oscillator is a necessary requirement to observe a pump-probe signal or any other 3^{rd}-order spectroscopic signal. For a harmonic oscillator, the 3^{rd}-order response vanishes exactly since the responses arising from transitions between states $|n\rangle \leftrightarrow |n+1\rangle$ and $|n+1\rangle \leftrightarrow |n+2\rangle$ cancel each

[d] Along the same lines, one can also show that $\hat{a}$ and $\hat{a}^\dagger$ satisfy the commutation relation $[\hat{a}, \hat{a}^\dagger] = \frac{1}{i\hbar}[\hat{q}, \hat{p}] = \hat{\mathcal{I}}$.

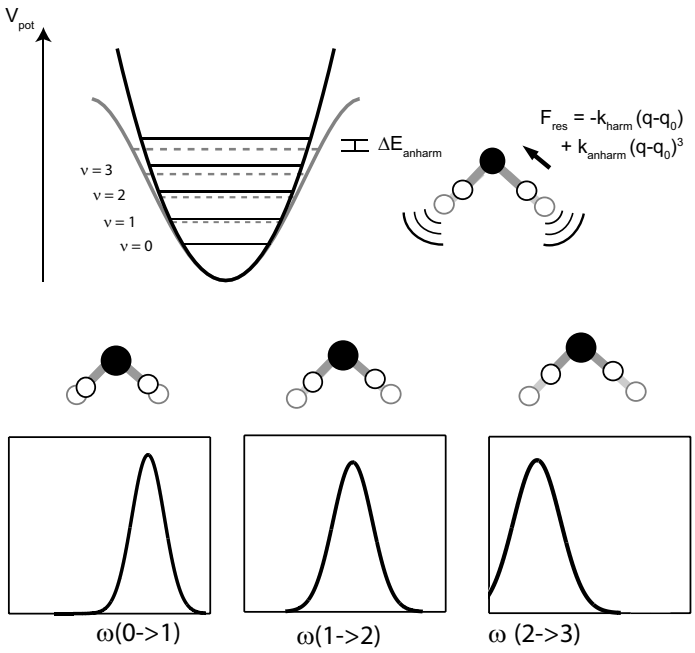

FIGURE 2.4. Illustration of the effect of quartic diagonal anharmonicity on the energy levels of a quantum mechanical oscillator described by the hamiltonian $\hat{H} = \frac{\hat{p}^2}{2m} + \frac{1}{2}m\omega^2\hat{q}^2 + k_4\hat{q}^4$. The term proportional to $\hat{q}^4$ leads to a lowering of the n^{th} energy eigenvalues relative to the energy level of a quantum harmonic oscillator. The energy levels converge with increasing quantum number according to Eq. (2.65). The effect on the transition frequencies between states n and $n+1$ and the associated absorption spectrum is illustrated in the bottom panels: the convergence of the energy levels leads to a red-shift of the $n \rightarrow n+1$-transition frequency relative to the $0 \rightarrow 1$-transition with increasing quantum number n.

other exactly.

2.5.3 NEAR RESONANTLY COUPLED OSCILLATORS

We will consider now the case of two coupled oscillators, for which we write the full hamiltonian as

$$\hat{H} = \hat{H}_1 + \hat{H}_2 + \hat{V}_{coup}(\hat{q}_1, \hat{q}_2) \tag{2.67}$$

We will assume the simplest form for the coupling term $\hat{V}_{coup}$, i.e. a bilinear coupling, which we write as

$$\hat{V}_{coup}(\hat{q}_1, \hat{q}_2) = k_{12}\hat{q}_1\hat{q}_2 \tag{2.68}$$

It will become clear later on that that it is important to include the effect of anharmonicity in the expressions for $\hat{H}_1$ and $\hat{H}_2$. We will let Δ_i denote the an-

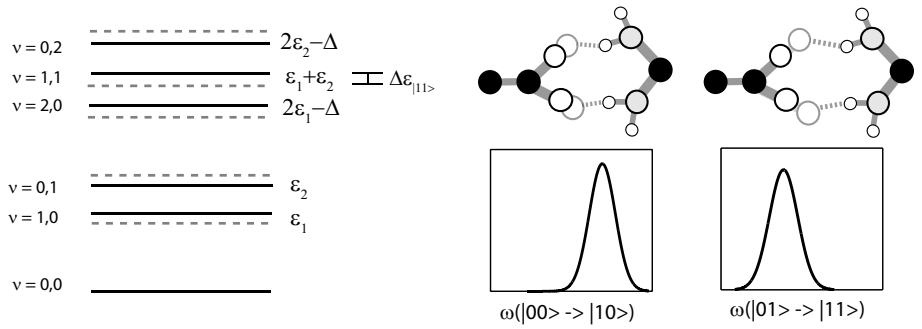

FIGURE 2.5. Energy level diagram for two weakly coupled, anharmonic oscillators. The coupling between the two oscillators leads to a shift of the energy levels relative to the uncouples states. Since state $|11\rangle$ is lowered by an amount $\Delta\epsilon_{|11\rangle}$ from the sum of the energies of the first excited states $\epsilon_1 + \epsilon_2$, the transition $|01\rangle \rightarrow |11\rangle$ is red-shifted from the transition $|00\rangle \rightarrow |10\rangle$. The coupling between molecular vibrations can thus experimentally be observed by selectively exciting the fundamental transition of one oscillator ($|00\rangle \rightarrow |01\rangle$) and probing the absorption changes of the other oscillator. A non-zero transient absorption change will be observed at the frequency of the fundamental transition of the second oscillator as a result of the red-shift of the absorption spectrum. This mechanism gives rise to cross-peaks in a two-dimensional IR-spectrum and is illustrated on the right side of this figure for the case where the coupling results from an intermolecular interaction.

harmonicity of the oscillator, i.e. the amount by which the second excited state differs from the the harmonic value $\Delta = 2\epsilon_{|n=1\rangle} - \epsilon_{|n=2\rangle}$. Making again use of creation and annihilation operators and assuming for simplicity $\Delta_1 = \Delta_2 = \Delta$, we can write for Eq. (2.67)[e]

$$\hat{H} = \sum_{i=1}^{2}\left[\hbar\omega_i\left(\hat{a}_i^\dagger\hat{a}_i + \frac{1}{2}\hat{\mathcal{I}}\right) + \frac{\Delta}{2}\hat{a}_i^\dagger\hat{a}_i^\dagger\hat{a}_i\hat{a}_i\right] + k'_{12}(\hat{a}_1 + \hat{a}_1^\dagger)(\hat{a}_2 + \hat{a}_2^\dagger) \qquad (2.69)$$

where $k'_{12} = -\frac{1}{2}k_{12}\hbar\sqrt{\frac{1}{\omega_1\omega_2 m_1 m_2}}$ as can be seen by comparison with Eq. (2.63). If we write out the last term in Eq. (2.69), we obtain terms of the form $\hat{a}_1\hat{a}_2$ and $\hat{a}_1^\dagger\hat{a}_2^\dagger$. These terms are non-quantum conserving terms, i.e. they create or annihilate excitations on oscillators 1 and 2 simultaneously and thus couple states that differ by two quanta of excitation. Unless the coupling constant is extremely large, these terms lead to negligible mixing and energy shifts. In contrast, terms of the form $\hat{a}_1\hat{a}_2^\dagger$ and $\hat{a}_1^\dagger\hat{a}_2$ couple energetically closely lying states by creating an additional excitation on one oscillator while annihilating an excitation on the other.

We can express the hamiltonian in Eq. (2.69) in a basis that includes the ground states as well as the first two excited states of two oscillators, and we will denote these states as $|00\rangle, |01\rangle, |10\rangle, |11\rangle, |02\rangle, |20\rangle$. If we let β_{12} denote

[e] $\frac{\Delta}{2}\langle n = 2|\hat{a}^\dagger\hat{a}^\dagger\hat{a}\hat{a}|n = 2\rangle = \Delta$

elements of the form $k'_{12}\langle 01|\hat{a}_1\hat{a}_2^\dagger|10\rangle$, this leads to the matrix [35]

$$H = \begin{pmatrix} 0 & & & & & \\ & \epsilon_1 & \beta_{12} & & & \\ & \beta_{12} & \epsilon_2 & & & \\ & & & 2\epsilon_1 - \Delta & 0 & \sqrt{2}\beta_{12} \\ & & & 0 & 2\epsilon_2 - \Delta & \sqrt{2}\beta_{12} \\ & & & \sqrt{2}\beta_{12} & \sqrt{2}\beta_{12} & \epsilon_1 + \epsilon_2 \end{pmatrix} \tag{2.70}$$

Here, the term β_{12} couples only states that are close in energy. This makes Eq. (2.70) block-diagonalizable, i.e. the matrix can be diagonalized with respect to its one-excitation states and separately with respect to the 2-excitation states. While for the degenerate case $\omega_1 = \omega_2 = \omega$, the elements of the diagonal hamiltonian matrix can be found analytically (see e.g. Chapter 6 of [35]), this is not feasible for the non-degenerate case, but can be done numerically in a straight-forward way. Thus in order to be able to calculate the energy levels and hence the frequencies at which cross- and diagonal peaks can be expected in a 2DIR-experiment, only an expression for the coupling strength β_{12} is required. An explicit expression for the off-diagonal anharmonicity can be obtained by treating the coupling as a weak perturbation and using 2^{nd}-order perturbation theory [37, 38]:

$$\Delta\epsilon_{|11\rangle} \equiv \epsilon^{(2)}_{|11\rangle} - \epsilon^{(0)}_{|11\rangle} = \frac{2\beta_{12}^2}{\epsilon^0_{|11\rangle} - \epsilon^0_{|20\rangle}} + \frac{2\beta_{12}^2}{\epsilon^0_{|11\rangle} - \epsilon^0_{|02\rangle}} \tag{2.71}$$

We have included only states from the two-quanta manifold in the sum, since terms involving states from the 1-quanta manifold contribute only negligibly due to the energy spacing in the denominator of Eq. (2.71). Evaluating the previous expression and neglecting terms that are quadratic in the site anharmonicity Δ, we arrive at the expression

$$\Delta\epsilon_{|11\rangle} = -\frac{4\Delta\beta_{12}^2}{\epsilon_{|10\rangle} - \epsilon_{|01\rangle}} \tag{2.72}$$

where we have used $\epsilon_{|20\rangle} = 2\epsilon_{|10\rangle} - \Delta$ and $\epsilon_{|02\rangle} = 2\epsilon_{|01\rangle} - \Delta$. Thus we see that the off-diagonal anharmonicity in a 2D-IR experiment is related to the energy splitting between the two oscillators $\epsilon_{|10\rangle} - \epsilon_{|01\rangle}$, the coupling strength β_{12} and the diagonal anharmonicity Δ. The latter factor is especially relevant: we see from the form of Eq. (2.72) that *cross*-anharmonicity can only be observed for two coupled *anharmonic* oscillators, i.e. for a non-zero diagonal anharmonicity Δ. A hamiltonian matrix describing coupled *harmonic* oscillators can always be diagonalized, and in this case a cross-anharmonic response cannot be observed.

2.5.4 Vibrational couplings and their relation to molecular structure

The physical nature of the coupling constant β has not been vital up to this point of the discussion. In many instances, it can be approximated by the

simple transition dipole coupling (TDC) model. This model approximates the interaction of oscillators in spatial proximity as purely dipolar in nature. For a more complete description of the coupling mechanism, multipolar electrostatic interactions as well as through-bond effects should be included, which comes at the expense of a less intuitive and computationally more demanding procedure [39, 40]. Within the TDC-model, the expression for β is given by [30, 37]

$$\beta_{ij} = \frac{\vec{\mu}_i \cdot \vec{\mu}_i - 3\,(\vec{n}_{ij} \cdot \vec{\mu}_i)(\vec{n}_{ij} \cdot \vec{\mu}_j)}{\vec{r}_{ij}^{\,3}} \tag{2.73}$$

Here, $\vec{\mu}_i$, $\vec{\mu}_j$ denote the transition-dipoles of two vibrational modes i and j, $\vec{r}_{ij}$ denotes the distance vector between the dipoles and $\vec{n}_{ij}$ is a unit vector along $\vec{r}_{ij}$. Thus we see that the electrostatic interaction between vibrational modes is strongly distance- and orientation dependent. This type of interaction is of relevance for vibrational oscillators in close spatial proximity such as the OH-groups in liquid water (Chapter 4) or the amide moieties (C=O-groups) in a protein (Chapter 6). The TDC model provides a simple and efficient way of calculating the effects of transition dipole coupling on e.g. the experimental 2D-IR experiment. To describe the 2D-IR-response in the spectral region of the amide vibrations for a complex molecule such as a peptide or a protein comprising several coupled amide oscillators, the effects of distance and orientation dependent electrostatic coupling can be calculated from Eq. (2.73). This expression can be combined with the atomic coordinates from a high resolution molecular structure obtained from X-ray crystallography or nuclear magnetic resonance spectroscopy. The anharmonicity Δ and the transition dipole strength $|\vec{\mu}_i|$ of an individual amide group, which are required to calculate the off-diagonal anharmonicity in Eq. (2.72), can be experimentally determined from a simple model compound such as N-methyl acetamide, which contains a single amide unit. With these parameters, the 2D-IR spectrum can be calculated. Dynamical effects arising from the interactions with the fluctuating bath, leading to relaxation and spectral diffusion processes, can be obtained e.g. from a molecular dynamics simulation.

2.6 ORIENTATIONAL RELAXATION

2.6.1 THE ANISOTROPY PARAMETER

In Chapter 5, the orientational dynamics of water (HDO) molecules in binary mixtures with DMSO and acetone are studied by polarization-resolved pump-probe spectroscopy with mid-infrared pulses that are resonant with the OD-stretch vibration. The quantity of interest is the anisotropy parameter R(t), which is determined from the transient absorption signal obtained under parallel ($\Delta\alpha_\parallel$) and perpendicular ($\Delta\alpha_\perp$) polarization of pump and probe pulses as

$$R(\omega,t) = \frac{\Delta\alpha_\parallel(\omega,t) - \Delta\alpha_\perp(\omega,t)}{\Delta\alpha_\parallel(\omega,t) + 2\Delta\alpha_\perp(\omega,t)} \tag{2.74}$$

While water molecules are typically randomly distributed in thermal equilibrium, the excitation of the OD-stretch vibration with a linearly polarized pump pulse leads to the preparation of an anisotropic distribution of excited HDO molecules. The excitation probability of a molecule via a dipolar light-matter interaction is related to the angle θ between the transition dipole vector $\vec{\mu}$ and the electric field vector $\vec{E}_0$ and can be written in terms of Fermi's golden rule as

$$W_{01} = \frac{2\pi}{\hbar^2}\vec{E}_0^2 \ \cos^2(\theta)|\langle 0|\vec{\hat{\mu}}|1\rangle|^2 \ \delta(\omega \pm \omega_{01}) \tag{2.75}$$

where $|0\rangle$ and $|1\rangle$ denote the two states involved in the transition. The excitation pulse preferentially excites those molecules that have their transition dipoles oriented parallel to the polarization axis of the pump pulse, which is reflected in the $\cos^2(\theta)$-factor in Eq. (2.75). We will treat the problem in spherical coordinates and assume a coordinate system in which the polarization vector of the excitation pulse coincides with the z-axis, as schematically outlined in Figure 2.6. The distribution of molecules with transition dipole moments $\vec{\mu}$ is assumed to be isotropic, and the distribution of excited molecules will therefore be independent of the azimuthal angle ϕ, and only depend on the relative angle between $\vec{\mu}$ and $\vec{E}_{exc}$. The anisotropic distribution of excited molecules prepared by the pump pulse can thus be written as[f]

$$p(\theta) = \frac{3}{4\pi}\cos^2\theta = \frac{1}{4\pi}[1 + 2P_2(\cos\theta)] \tag{2.76}$$

where $P_2(\cos\theta)$ denotes the second Legendre polynomial defined as $P_2(\cos\theta) = 1/2(3\cos^2\theta - 1)$. In order to evaluate the values that can be expected for the experimentally determined anisotropy parameter R(t), we will consider the case that the probe pulse interrogates the ensemble of excited molecules before any reorientation has taken place. If we let χ denote the angle between the

[f] $p(\theta)$ represents a probability density function and is therefore required to be normalized. The normalization constant is obtained by calculating $\int d\Omega\cos^2\theta = \int_0^{2\pi} d\phi \int_0^{\pi} \sin\theta d\theta \cos^2\theta = {}^{4\pi}/_{3}$.

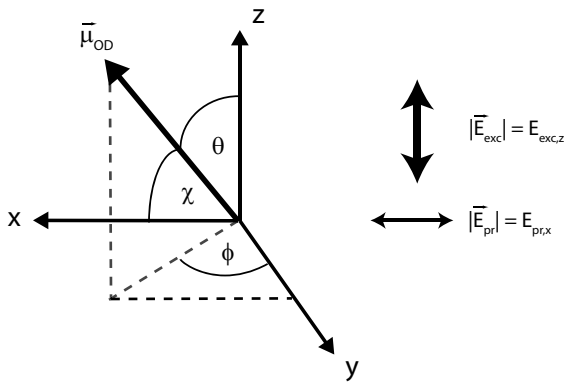

FIGURE 2.6. Coordinate system used to calculate the transient absorption changes $\Delta\alpha_\perp$, $\Delta\alpha_\parallel$ observed in a polarization-resolved experiment in response to excitation of an ensemble of molecules with a linearly polarized light pulse with its polarization vector parallel to the z-axis of the coordinate system. θ denotes the angle between the transition dipole moment $\vec{\mu}$ and the z-axis of the coordinate system, and ψ refers to the angle between $\vec{\mu}$ and the x-axis. ϕ denotes the azimuthal angle.

polarization vector of the probe pulse and the transition dipole $\vec{\mu}$ as indicated in Figure 2.6, we can write for the transient absorption changes obtained with a probe pulse with polarization perpendicular to the excitation pulse ($|\vec{E}_{pr}| = E_{pr,x}$)

$$\Delta\alpha_\perp = \int_0^\pi \sin\theta\, d\theta \int_0^{2\pi} d\phi\, p(\theta) \sin^2\theta \sin^2\phi = {}^1\!/_5 \tag{2.77}$$

where we have written the solid angle $d\Omega$ as $\sin\theta\, d\theta\, d\phi$ and substituted $\cos^2\chi$ by $\sin^2\theta \sin^2\phi$. For the transient absorption change obtained with a probe pulse with the same polarization as the excitation pulse ($|\vec{E}_{pr}| = E_{pr,z}$), we can write

$$\Delta\alpha_\parallel = \int_0^\pi \sin\theta\, d\theta \int_0^{2\pi} d\phi\, p(\theta) \cos^2\theta = {}^3\!/_5 \tag{2.78}$$

Substituting these values in Eq. (2.74), it follows that we can expect a value of $^2\!/_5$ for the anisotropy parameter at the earliest pump-probe delay times, i.e. before reorientation affects the outcome of the measurement. The scrambling of the anisotropy as a function of time will be treated in the next section.

2.6.2 THE TIME-DEPENDENCE OF THE ANISOTROPY PARAMETER

So far we have only considered the anisotropy value that is to be expected if an anisotropic ensemble of molecules is prepared via (dipolar) excitation by a linearly polarized light pulse. Molecular motions however will lead to a loss of

orientational correlation between the excited molecules, thus causing the excited molecules to become isotropically distributed. This is equivalent to saying that all excited molecules are equally distributed over the surface of a unit sphere with area 4π and thus we can write for the long-time behavior of Eq. (2.76) $p(t \to \infty) = {}^1\!/_{4\pi}$. We will treat the reorientational motion of excited molecules as rotational diffusion on a sphere of unit radius. The distribution of excited molecules is independent of ϕ at all times t. The probability that a molecule with transition dipole $\vec{\mu}$ has an orientation given by θ at time t will be denoted as $p(\theta, t)$. The time-evolution of this probability is then given by the diffusion equation

$$\frac{\partial p(\theta,t)}{\partial t} = -D_r \Delta_\theta p(\theta,t) \tag{2.79}$$

where D_r is the angular diffusion constant and Δ_θ denotes the operator $\frac{1}{r^2 \sin^2\theta}[\sin\theta \frac{\partial}{\partial\theta} \sin\theta \frac{\partial}{\partial\theta}]$ with $r = 1$ for the radius of a unit sphere. If we know the function $G(\theta_t\, t|\theta_0, t_0)$, which represents the conditional probability that the orientation will be θ_t at time t, given that it was θ_0 at t_0, we can write for the distribution $p(\theta, t)$ at time t:

$$p(t,\theta_t) = \int_0^{2\pi} d\phi_0 \int_0^{\pi} \sin\theta_0 d\theta_0 G(\theta_t, t|\theta_0, t_0) p(t_0, \theta_0) \tag{2.80}$$

The function $G(\theta_t, t|\theta_0, t_0)$ is the Green's function solution to the diffusion equation Eq. (2.79), which can be written in terms of the Legendre polynomials $P^l(\cos\theta)$ of rank l:

$$G(\theta_t, t|\theta_0, t_0) = \sum_{l=0} e^{-l(l+1)D_r t}\, P^l(\cos\theta_t) P^l(\cos\theta_0) \tag{2.81}$$

Substituting Eq. (2.81) into Eq. (2.80) and using Eq. (2.76) for $p(t_0, \theta_0)$, we obtain for the probability of a molecule having an orientation θ_t at time t

$$p(\theta_t, t) = \frac{1}{4\pi}[1 + 2e^{-6D_r t} P_2(\cos\theta_t)] \tag{2.82}$$

where we have made use of the orthogonality relation of the Legendre polynomials. In analogy to Eq. (2.78) and Eq. (2.77), we can now write an expression for the time-dependence of the transient absorption changes $\Delta\alpha_\parallel$ and $\Delta\alpha_\perp$ for parallel and perpendicularly polarized excitation and probe pulses:

$$\Delta\alpha_\parallel(t) = \int d\Omega_t p(t,\theta_t) \cos^2\theta_t \tag{2.83}$$

$$= \int d\Omega_t \int d\Omega_0 G(\theta_t, t|\theta_0, t_0) p(t_0, \theta_0) \cos^2\theta_t$$

$$\Delta\alpha_\perp(t) = \int d\Omega_t p(t,\theta_t) \sin^2\theta_t \sin^2\phi_t$$

$$= \int d\Omega_t \int d\Omega_0 G(\theta_t, t|\theta_0, t_0) p(t_0, \theta_0) \sin^2\theta_t \sin^2\phi_t$$

where we have introduced $\int d\Omega$ as shorthand for $\int_0^{2\pi} d\phi \int_0^{\pi} \sin\theta d\theta$. Substituting Eq. (2.82) in Eq. (2.83), we obtain

$$\Delta\alpha_{\parallel}(t) = \frac{1}{3} + \frac{4}{15}e^{-6D_r t} \tag{2.84}$$

$$\Delta\alpha_{\perp}(t) = \frac{1}{3} - \frac{2}{15}e^{-6D_r t} \tag{2.85}$$

From these results, we obtain the time-dependence of the anisotropy parameter as defined in Eq. (2.74)

$$R(t) = \frac{2}{5}e^{-6D_r t} \tag{2.86}$$

We can see an important consequence of Eq. (2.82), namely that the decay time that is measured in an experiment depends on the order l as $\tau_r = \frac{1}{D_r l(l+1)}$. While the angular diffusion constant D_r is obviously a molecular parameter, the decay times that are obtained under different experimental configurations can thus differ. A pump-probe experiment such as described in this thesis, probes the second-rank orientational correlation function ($l = 2$), whereas dielectric relaxation experiments measure the first rank ($l = 1$) correlation function. The associated decay time constants thus differ by a factor of 3 in the case of diffusive reorientation. This subtlety has to be kept in mind when comparing experimental data obtained for the same sample with different techniques.
This section is largely based on: T. Tao Bioplymers, 1968; G. Lipari & A. Szabo Biophys.J. 1980, B. Berne & Pecora, Dynamic Light Scattering.

3 Experimental section

In the following, the three experimental setups that have been used in collecting the data for this thesis are presented.

3.1 One-color infrared pump-probe setup

The experiments described in Chapters 4 and 5 were performed with a femtosecond mid-infrared setup based on a commercial regenerative Titan:sapphire amplifier system (Spectra Physics Hurricane), delivering 100 fs-pulses centered around 800 nm and a pulse energy of 1 mJ at a repetition rate of 1 kHz. About 700 μJ of the pulses are used to pump a commercial optical parametric amplifier (OPA, Spectra Physics) based on β-barium borate (BBO). The OPA is seeded by a white-light continuum generated by focussing a small fraction of the 800 nm-beam into a sapphire plate. The white-light seed and a fraction of the 800 nm-pump beam are then overlapped in a BBO-crystal, leading to the generation of signal and idler beams in the wavelength ranges of λ_S = 1250-1330 nm (signal) and λ_I = 2000-2200 nm (idler). The signal beam is filtered out by a dichroic mirror and the idler is used to seed a second amplification process in the same BBO-crystal driven by $\sim$ 570 μJ of the 800 nm-pump beam, yielding final pulse energies of 40 μJ (signal) and 20 μJ (idler). The desired wavelengths are selected by angle tuning of the BBO-crystal. The resulting idler beam is frequency doubled in a second BBO-crystal to a wavelength of 1000-1100 nm and is subsequently used as a seed for parametric amplification pumped by the remaining part ($\sim$ 300 μJ) of the 800 nm-beam in either a lithium niobate ($LiNbO_3$) or a potassium titanyl phosphate ($KTiPO_4$) crystal, leading to the generation of mid-infrared pulses with a center wavelength of λ_{IR} = 3-4 μm and a pulse length of $\sim$ 150 fs. Pulse energies are typically in the range of 5-9 μJ. Residual signal and (doubled) idler beams are filtered out by a germanium-based long-wave pass (LWP) filter with a cut-off wavelength of 2.5 μm.
The mid-infrared pulses are used in a pump-probe experiment as schematically depicted in Figure 3.1. Reflections from the front and the back side of a calcium fluoride (CaF_2) wedge are used as probe and reference beams, respectively. The transmitted part ($\sim$ 90%) is used as the pump beam. Its plane of polarization is rotated by a $\lambda/2$-plate to an angle of 45° relative to the plane of polarization of the probe beam. A chopper running at half the repetition of the laser system is placed in the beam path of the pump to block every other shot, so that long term drifts are minimized and only pump-induced absorption changes are monitored. The probe beam is delayed in time by sending it over a motorized delay stage. All beams are focussed by a gold-coated off-axis parabolic mirror

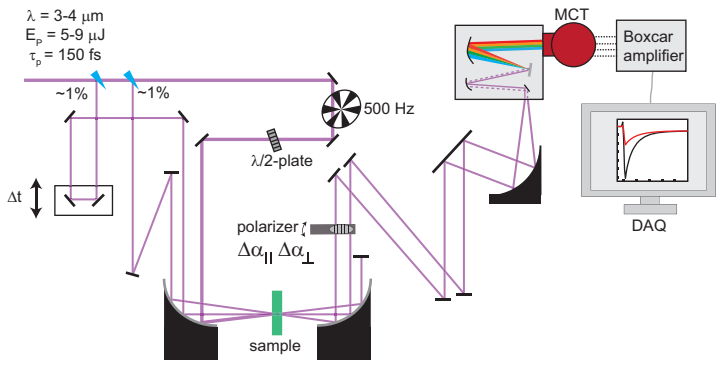

FIGURE 3.1. Schematic outline of the infrared pump-probe experiment that was used for the experiments in Chapters 4 and 5 of this thesis. The mid-infrared pulses are delivered from an a optical parametric amplifier/difference frequency generation stage as described in the text and split into three parts. The pump-beam resonantly excites the the OH-stretch (OD-stretch) vibration of water molecules, and a weak, time-delayed probing pulse measures the pump-induced absorption changes. The probe and the reference pulse are frequency-dispersed by a spectrograph and imaged on an MCT-array detector of 2x32 pixels.

with a focal length of $f = 100$ mm into the sample and recollimated by an identical mirror. The sample itself is usually a liquid layer of 1-100 μm thickness, sandwiched between two CaF_2 windows. The polarization components of the probe beam parallel and perpendicular to the pump beam are selected by a wire grid polarizer on CaF_2, placed behind the sample, that can be rotated over 90°. The probe and reference beams are sent into an imaging spectrograph (Lot Oriel) and imaged on a 2x32 pixel array of a mercury cadmium telluride (MCT)-based infrared detector (Infrared Associates), placed in the exit plane of the spectrograph. The signal is amplified by a gated boxcar-integrator and digitized by a 16-bit A/D-converter card (Measurement Computing). The transient absorption change is calculated as

$$\Delta\alpha = -\log_{10} \frac{I_{pr}/I^o_{pr}}{I_{ref}/I^o_{ref}} \tag{3.1}$$

where I_{pr} and I_{ref} denote the recorded intensity of probe and reference beams in the presence of the pump, and I^o_{pr} and I^o_{ref} denote the probe and reference intensity in the absence of the pump. Dividing the recorded probe intensity I_{pr} by the intensity of the reference beam I_{ref} eliminates pulse-to-pulse fluctuations and increases the signal-to-noise ratio of the experiment. If we let $\Delta\alpha_{\|}$ denote the absorption change monitored with the polarization component of the probe beam that is parallel to the plane of polarization of the pump beam and $\Delta\alpha_{\|}$ the absorption change with the perpendicularly polarized component of the probe beam, we can calculate the isotropic absorption change $\Delta\alpha_{iso}$ as

$$\Delta\alpha_{iso}(\omega,t) = \frac{1}{3}(\Delta\alpha_{\parallel}(\omega,t) + 2\Delta\alpha_{\perp}(\omega,t)) \tag{3.2}$$

The isotropic signal is unaffected by orientational effects and reflects vibrational relaxation and spectral diffusion. In addition, we also construct the anisotropy parameter R(ω,t) given by Eq. (2.74), which reflects the orientation of the transition dipole moment of the probed vibration.

3.2 TWO-DIMENSIONAL INFRARED SETUP

The experimental setup for two-dimensional infrared (2D-IR) spectroscopic experiments in Chapters 6 and 7 is shown in Figure 3.2. The experiments were performed with a frequency-domain implementation of two-dimensional spectroscopy (*spectral hole burning*) that makes use of spectrally narrow excitation pulses. In this experiment, mid-infrared pulses with a center wavelength of ~ 6 μm were generated in a commercial high-energy optical parametric amplifier (HE-Topas, Light Conversion) pumped by 35 fs 800 nm pulses with a pulse energy of 4.5 mJ delivered by a commercial regenerative Titanium:sapphire amplifier (Legend Elite Duo, Coherent) at a repetition rate of 1 kHz. The first parametric amplification step in a BBO-crystal is seeded by a white-light continuum, generated by focussing a small fraction of 800 nm-light into a sapphire-plate. Signal and idler beams with wavelength of $\lambda_S \approx 1.4$ μm and $\lambda_I \approx 1.8$ μm, respectively, are then further amplified to final pulse energies of 1.125 mJ (signal) and 0.875 mJ (idler) in two subsequent BBO-crystals. Mid-infrared pulses with a pulse energy of ~ 25 μJ and a bandwidth of 350 cm^{-1} are generated *via* a type I difference-frequency generation (DFG) process by overlapping the signal and idler beams in a 0.6 mm thick silver thiogallate crystal ($AgGaS_2$, cut-angle $\theta = 39°$). After the generation of the mid-infrared pulses, the residual signal and idler beams are filtered out by a germanium-based long-wave pass filter with a cut-off wavelength of 4 μm. The use of a longer cut-off wavelength (compared to the one-color infrared pump-probe setup) is required to filter out infrared light at 3 μm, resulting from a second harmonic generation process of the mid-infrared pulses at 6 μm that is close to being phase-matched in the $AgGaS_2$ crystal.

The mid-infrared pulses are split in pump, probe and reference pulses as described in Section 3.1. The pump light is directed into an air-spaced, tunable Fabry-Perot etalon, consisting of two parallel, highly reflecting mirrors (reflectivity R = 90%). The spacing between the mirrors and thus the optical path length difference, that determines which frequency components interfere constructively and destructively, can be adjusted to generate spectrally narrow excitation pulses from the broad-band mid-infrared pulses. The narrow-band excitation pulses have a Lorentzian-shape profile with a full-width at half maximum of 12-15 cm^{-1}, which corresponds in the time-domain to a single-sided exponential with a characteristic decay time τ in the range of 500-600 fs, as inferred from two-photon absorption in an indium-arsenide wafer. Pump, probe

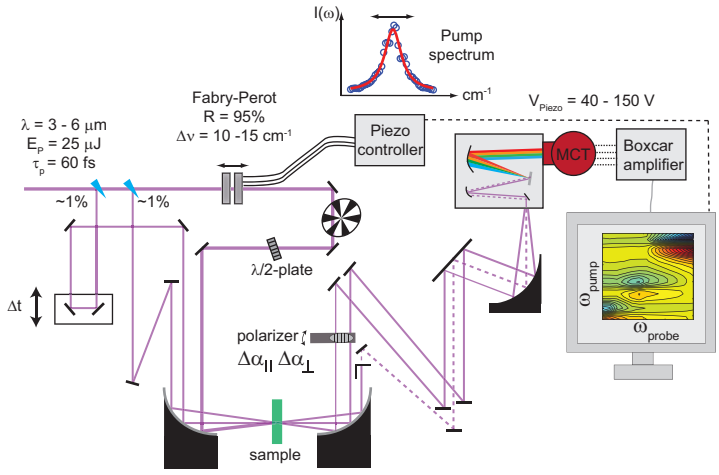

FIGURE 3.2. A transmission through the sample, a small fraction of the narrow-band pump pulse is directed into the spectrograph and dispersed on a 32-pixel MCT-array. The measured pump-pulse spectrum is then used as the input signal for the feedback-loop that controls the piezo-driven mirror mount. To compensate for the drift of the piezo-actuators on a time-scale of minutes, a reoptimization of the mirror positions after every delay scan is required (typically ∼5 mins) is required.

and reference beams are focussed by a gold-coated off-axis parabolic mirror with a focal length of $f = 75$ mm into the sample and recollimated by an identical mirror. The measurement of the pump-induced absorption changes $\Delta\alpha_{\parallel}$, $\Delta\alpha_{\perp}$ is performed in essentially the same way as was described in Section 3.1. A two-dimensional data set is assembled by scanning the spectrally narrow pump pulse over the desired frequency range, which requires adjusting the spacing between the mirrors of the etalon. In practice, this is achieved by placing one of the two mirrors on a piezo-driven mount and monitoring the pulse spectrum by directing a weak reflection of the pump light from a CaF_2-window into the spectrograph and imaging it on the MCT detector. The signal from the MCT detector is used in an automated feedback routine to drive the piezo-actuators, thereby allowing the tuning of the spectrally narrow excitation pulse to the desired center frequency.

3.3 SUM-FREQUENCY GENERATION SPECTROSCOPY SETUP

The surface sum-frequency generation experiment is based on a commercial Titanium:sapphire regenerative amplifier (Coherent Legend Elite) that delivers 35 fs pulses centered at 800 nm with a pulse energy of 3.5 mJ at a repetition rate of 1 kHz. Approximately two thirds of the output is used to pump a home-built optical parametric amplifier (OPA) based on β-barium borate, generating sig-

nal and idler pulses around 1270 nm and 2150 nm, respectively. Mid-infrared pulses are generated by mixing the signal and idler pulses in a type I difference frequency mixing process (DFG) in a 0.6 mm thick silver thiogallate crystal ($AgGaS_2$). The resulting femtosecond mid-infrared pulses (IR) are centered around 3200 cm^{-1}, have a bandwidth of $\sim$ 350 cm^{-1} and a pulse energy of 8 - 10 μJ. About 450 μJ of the 800 nm-output is sent through an air-spaced etalon to generate pulses with a narrow spectral bandwidth of $\sim$ 15 cm^{-1} centered around 800 nm.

The SFG technique probes the elements of the second-order susceptibility tensor $\chi^{(2)}$. The polarizations of the IR, visible (= 800 nm) and the detected sum-frequency light determine which elements are probed. The polarizations are denoted with s or p, depending on whether the light is polarized perpendicular (s-polarized) or parallel (p-polarized) to the plane of incidence of the beams. A polarization configuration psp implies that the detected SFG-light is p-polarized, the visible (VIS) is s-polarized, and the mid-infrared beam is p-polarized. The polarizations of the VIS and the IR beams are set by means of $\lambda/2$-plates in combination with a wire-grid polarizer (IR) or a Glan-Laser-prism (VIS). The VIS and the IR beams are focused on the sample surface by lenses with focal lengths of f = 200 mm and f = 100 mm, respectively. The beams are sent to the sample with an angle of incidence of $\sim 50°$ and $\sim 55°$, respectively, and are spatially and temporally overlapped at the sample to generate light at the sum-frequency (SFG). For intensity (non-phase-resolved) SFG-measurements, the generated SFG-light is sent into a spectrograph, after filtering out the residual 800 nm light, and dispersed on a thermoelectrically-cooled EMCCD-camera (Andor Technologies). A polarizing beam-splitter cube in the detection path is used to select the polarization of the generated SFG-light. The SFG-spectra are normalized to a non-resonant reference SFG-signal from a z-cut quartz crystal. The signal is integrated for typically 10 minutes in both direct and phase-resolved SFG-experiments.

Phase-resolved SFG spectra are obtained by interfering the SFG light generated by the sample with the SFG light generated from a local oscillator. The lay-out is schematically depicted in Figure 3.3. The IR- and the VIS-beam are first focused on a bare gold mirror to generate a local oscillator (LO) before they are refocused by a spherical mirror together with the LO-beam on the sample. The LO-beam from gold is time-delayed ($\sim$ 2 ps) by transmitting it through a fused silica plate. The SFG-signals from gold and from the sample propagate collinearly through the detection path and generate a spectral interferogram on the CCD-camera after being dispersed by a spectrograph. In Figure 3.4A, a spectral interferogram from a phase-resolved SFG-experiment recorded under ssp-polarization is shown. The fringe pattern originates from the interference between the time-delayed LO-SFG-signal (E_{LO}) and the SFG-signal generated from an aqueous sample (E_{sample}). The recorded intensity of the heterodyne-detected SFG (HD-SFG) signal is given by:

$$I_{HD-SFG}(\omega) \propto |E_{sample}(\omega)|^2 + |E_{LO}(\omega)|^2 \qquad (3.3)$$
$$+E^*_{sample}(\omega)E_{LO}(\omega)e^{i\omega\Delta t} + E_{sample}(\omega)E^*_{LO}(\omega)e^{-i\omega\Delta t}$$

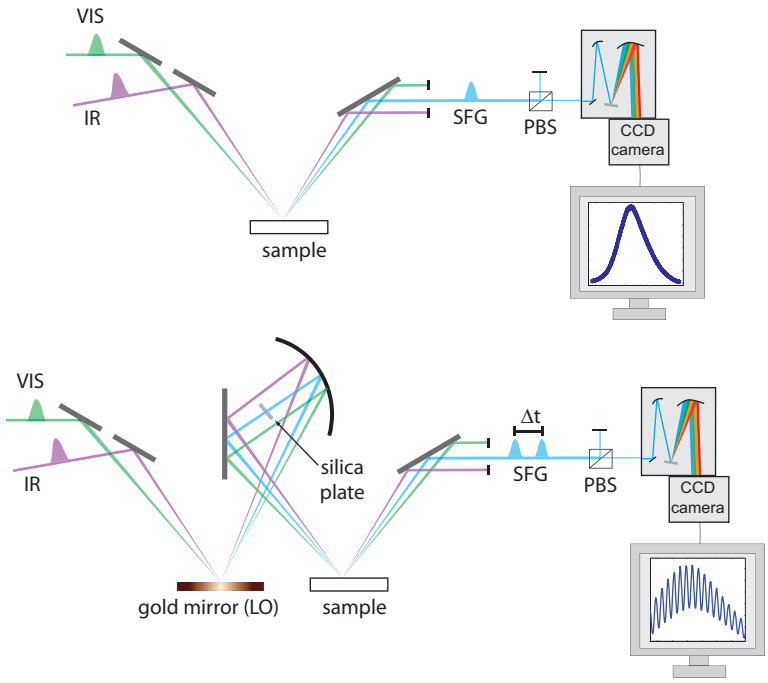

FIGURE 3.3. Top: schematic of the experimental geometry of the sum-frequency generation spectroscopy setup used for intensity (non-phase resolved) measurements. Mid-infrared pulses (IR) are generated by a home-built optical parametric amplifier and spectrally narrow upconversion pulses (VIS, $\Delta\tilde{\nu}$ ≈15 cm^{-1}) are generated by transmission of a fraction of the 800 nm laser fundamental through an air-spaced etalon. The desired polarization of the generated SFG-light is selected with a polarizing beam splitter (PBS) and subsequently frequency-dispersed in a spectrograph and imaged on a CCD-camera. Bottom: Experimental arrangement used for phase-resolved measurements. A non-resonant SFG-field (local oscillator, LO) is generated from the surface of a bare gold mirror and delayed in time by transmission through a silica plate. Subsequently, all three beams (IR, VIS, LO) are recombined on the sample surface, where a second SFG-generation process takes place. The interference between the SFG-field generated at the sample and the time-delayed local oscillator leads to a fringe pattern in the detected interferogram.

The cross-term $E_{sample}E_{LO}^{*}e^{-i\omega\Delta t}$ of this equation contains the electric field of the SFG-signal originating from the sample and therefore offers access to the complex non-linear susceptibility. As was shown in Section 2.2, the SFG-field is related to the non-linear susceptibility as $E_{SFG} \propto \chi^{(2)}E_{VIS}E_{IR}$. To retrieve the complex-valued $\chi^{(2)}$ of the sample, an inverse Fourier transformation of the recorded interferogram $FT^{-1}[I_{HD-SFG}(\omega)]$ is performed. The imaginary part of the complex time-domain signal obtained in this way is shown in Figure 3.4B. The desired cross-term indicated in Figure 3.4B can now be isolated by setting the signal at $t \leq 0.8$ ps to zero and subsequently Fourier-transforming the

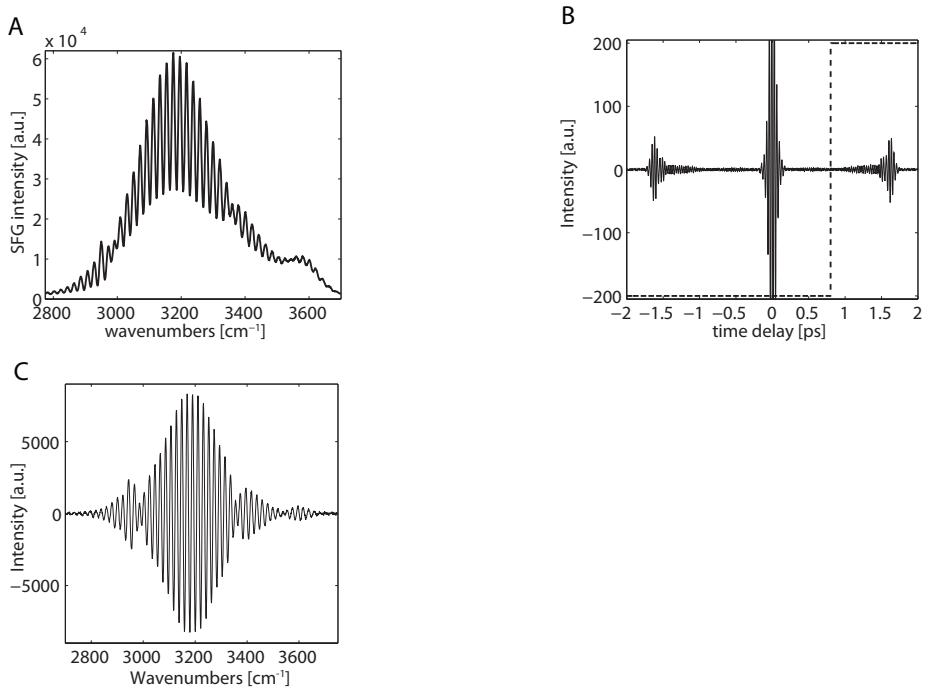

FIGURE 3.4. (A) Spectral interferogram recorded from an aqueous solution of an antifreeze protein under ssp-polarization setting. (B) Imaginary part of the time-domain signal obtained by applying an inverse Fourier transformation to the data in panel (A). The data for delay times $t \leq 0.8$ ps (indicated by the dashed line) are set to zero. (C) Imaginary part of the complex SFG-spectrum from the sample obtained by Fourier transformation of the filtered signal in panel (B).

filtered time-domain signal back to the frequency domain. In practice, the signal for $t \leq 0.8$ ps is filled with random numbers from a gaussian distribution with zero mean and a width comparable to the experimental noise level to avoid artifacts in the Fourier transformation arising from discontinuities in the signal. The imaginary part of the cross-term $E_{sample}(\omega)E^*_{LO}(\omega)e^{-i\omega\Delta t}$ obtained after filtering is shown in Figure 3.4C. The non-linear susceptibility $\chi^{(2)}_{sample}(\omega)$ is then obtained by dividing the signal shown in Figure 3.4C by a reference signal, which is obtained by replacing the sample with a z-cut quartz crystal with a known $\chi^{(2)}$. After applying the same filtering process as outlined above, $\chi^{(2)}_{sample}(\omega)$ is obtained as

$$\chi^{(2)}_{sample}(\omega) = \chi^{(2)}_{ref} \frac{E_{sample}(\omega)E^*_{LO}(\omega)e^{-i\omega\Delta t}}{E_{ref}(\omega)E^*_{LO}(\omega)e^{-i\omega\Delta t}} \tag{3.4}$$

where $\chi^{(2)}_{ref}$ and E_{ref} denote the nonlinear susceptibility of the (reference) quartz-crystal and the SFG-field generated from the crystal, respectively.

4 Vibrational energy transfer in anionic hydration shells

We study the influence of Förster energy transfer on the vibrational relaxation dynamics of anionic hydration shells by performing time-resolved mid-infrared spectroscopy on the OH-stretch vibration of water molecules in aqueous solutions of sodium iodide. We observe that Förster energy transfer leads to a pronounced acceleration of the vibrational relaxation. We describe the observed dynamics with a model in which we include Förster vibrational energy transfer between the different hydroxyl groups in solution. With this model we can quantitatively describe the experimental data over a wide range of isotopic compositions and salt concentrations. Our results show that resonant energy transfer is an efficient mechanism assisting in the vibrational relaxation of anionic hydration shells.

4.1 Introduction

The introduction of ions into the hydrogen-bonding network of liquid water leads to a disruption of the tetrahedral hydrogen-bonding arrangement, as was first observed with linear absorption and Raman experiments [41]. An important question related to ions in water concerns the range over which ions influence the structure of aqueous salt solution. Based on viscosity measurements and thermodynamics properties, the influence of ions on the hydrogen bonding network of water has been discussed in terms of "structure makers" and "structure breakers" , an idea that was first introduced in the 1930s by Cox and Wolfenden [42]. The term "structure makers" refers to small ions with a high charge density such as F^-, which are thought to have an ordering effect on the hydrogen bonding network, whereas "structure breakers" generally refers to larger ions with a low charge density such as Cs^+, that presumably lead to a weakening of the overall hydrogen bonding strength of water [43].
Over the past decade, time-resolved infrared spectroscopy has proven to be a useful technique to study the dynamics of water molecules both in the pure liquid and in the hydration shells of ions [6, 11, 12, 14, 44–48]. The hydroxyl stretch vibration (OH- or OD-stretch) has been the focus of most of the mid-infrared pump-probe-studies on aqueous salt solutions, since this mode forms

a highly sensitive spectroscopic marker for the local environment of a water molecule [6,9,11,12,14,44–49]. These spectroscopic studies have yielded valuable information on the vibrational [46, 47] and reorientational [6, 11, 44, 48] dynamics of water and on the dynamics of its hydrogen bonding network [11, 45, 49]. For example, the reorientational motion and the spectral diffusion dynamics of water molecules residing in the hydration shell of halide anions have both been found to show a very slow component in comparison to the dynamics of pure water [11, 13, 50]. The lifetime of the hydroxyl stretch vibration has been found to vary substantially in different hydrogen bonding environments. Several studies on aqueous salt solutions have shown that the formation of a hydrogen bond to a halide ion leads to a substantial increase in the lifetime of the hydroxyl-stretch vibration [11,47]. Similarly, for water contained in AOT reverse micelles, it was observed that the water molecules forming weak hydrogen bonds to the sulfonate groups of the AOT surfactants show a significantly slower vibrational relaxation with a T_1 time constant on the order of 3 ps [51, 52]. The groups of Fayer and Gaffney studied how long a water molecule resides in the hydration shell of an ion. In their studies, they observe an exchange between water molecules residing in anionic hydration shells and bulk water molecules that takes place on a timescale of 7 ps for BF_4^- [12] and 9 ps for ClO_4^- [13]. In both studies the rotation of water molecules out of the hydration shell was found to take place via large angular jumps. This mechanism of water reorientation has been predicted by Laage & Hynes [50]. The same mechanism is also active in bulk water [53].

Nearly all of the previously mentioned time-resolved infrared experiments have been performed on either the OD-stretch vibration of HDO molecules dissolved in H_2O or the inverse system (OH-stretch of HDO in D_2O) [8,9,11,45–49,54–56]. However, in real life, aqueous solutions usually contain pure H_2O, which has properties that are distinct from the aforementioned isotopic mixtures. One important feature of neat H_2O is the presence of efficient Förster resonant energy transfer between the OH-stretch vibrations. Förster resonant energy transfer has been studied both in neat H_2O and D_2O [57–59], and has been found to lead to an ultrafast redistribution of the excitation energy over neighboring OH (OD)-groups. In isotopic solutions resonant energy transfer is suppressed because of the increase in average distance between OH (OD) groups.

In view of this previous work, it is interesting to see how Förster resonant energy transfer affects the vibrational dynamics of water molecules in aqueous salt solutions. In this paper, we use aqueous solutions of sodium iodide as a model system to study the influence of Förster energy transfer on the vibrational relaxation dynamics of anionic hydration shells.

4.2 EXPERIMENTAL SECTION

The experiments in this chapter were performed with the one-color mid-infrared pump-probe setup described in Section 3.1. We measure the vibrational relaxation dynamics of the OH stretch vibration of HDO and H_2O molecules for

solutions of NaI in mixtures of H_2O/D_2O. The femtosecond pulses required for this study are generated by a series of nonlinear frequency conversion processes that are pumped with the pulses of a commercial Ti:sapphire regenerative amplifier (Spectra-Physics Hurricane). About 500 μJ of the amplifier output is split off to pump a white-light seeded optical parametric amplifier (OPA, Spectra Physics) based on BBO (β-barium borate), generating signal and idler pulses with a wavelength around 1250 nm and 2200 nm, respectively. The idler pulses are frequency-doubled in a second BBO-crystal, and the resulting pulses at 1100 nm are used as a seed for parametric amplification in a $KTiOPO_4$-crystal (potassium titanyl phosphate) that is pumped by the remaining 300 μJ of 800 nm light, leading to amplification of the doubled idler and generation of mid-IR pulses at the difference frequency. The resulting mid-IR pulses have a wavelength of $\sim$2.8 μm and have a duration of 180 fs, an energy of 5 μJ, and a spectral width of approximately 150 cm^{-1}.
We use the pulses in a pump-probe experiment as described in Section 3.1. We study aqueous solutions with NaI concentrations ranging from 1 to 6 mol/kg. NaI was purchased from Sigma Aldrich and used without further purification. The fraction of hydrogen

$$f_H = \frac{[H_2O]}{[H_2O] + [D_2O]} \tag{4.1}$$

was varied between 0.04 and 1, with $f_H = 1$ corresponding to neat H_2O. The samples were held between two CaF_2 windows separated by Teflon spacers with thicknesses ranging from 3.8 to 25 μm. Samples containing neat H_2O were measured without spacer to avoid complete absorption of the infrared light due to the large absorption cross section of H_2O in the frequency region of the OH stretch vibration. The estimated length of these samples is $\sim$1 μm. We measured linear absorption spectra of the samples with a Perkin-Elmer spectrometer. In all experiments we tuned the center frequency of the mid-IR pulses to the maximum of the linear absorption spectrum.

4.3 Results

4.3.1 Linear absorption spectra of HDO

Figure 4.1 shows linear absorption spectra in the OH stretch region for neat HDO:D2O ($f_H = 0.04$) and for aqueous NaI solutions of the same isotopic composition with salt concentrations ranging from 1 mol/kg to 4 mol/kg. The OH stretch band is centered at 3400 cm^{-1} for neat HDO:D_2O, and shifts to higher frequencies upon the addition of NaI, an effect that has been observed before for aqueous solutions containing halide ions [11, 12, 47, 60]. The blueshift results from the weakening of the hydrogen bonds upon the formation of anionic hydration shells. In particular, water molecules that donate a hydrogen bond to Cl^-, Br^- or I^- ions absorb at a higher frequency than water molecules that

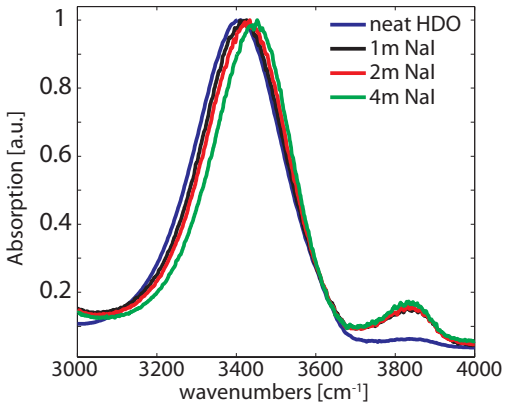

FIGURE 4.1. Linear absorption spectra of the OH-stretching region for aqueous NaI solutions ($f_H = 0.04$) and neat HDO:D_2O.

donate a hydrogen bond to the oxygen atom of another water molecule. In the following, we will distinguish anion-bound and water-bound water molecules, the latter referring to water molecules for which both hydroxyl groups donate hydrogen bonds to the oxygen atoms of other water molecules.

4.3.2 VIBRATIONAL RELAXATION OF WATER MOLECULES IN NaI SOLUTIONS

Figure 4.2A shows transient absorption spectra that were measured for a 4m NaI solution ($f_H = 0.04$) at delay times ranging from 0.2 ps to 10 ps. The concentration of OH-groups in this sample is sufficiently low to avoid Förster resonant energy transfer between the OH stretch vibrations [57]. Hence, this solution allows the study of the separate vibrational relaxation dynamics of anion-bound and water-bound water molecules. At early delay times, the spectra show a strong negative peak centered around 3420 cm^{-1}, originating from the bleaching of the ground state and stimulated emission from the first excited state. The excited state absorption (1→2 transition) is red-shifted by 200 cm^{-1} from the fundamental transition and lies outside the spectral window of the experiment. At late delay times (> 12 ps), the transient absorption spectra have the shape of a thermal difference spectrum, showing an induced absorption on the blue side and a bleaching-like signature in the red wing of the spectrum. This final spectrum results from the heating of the sample following the vibrational relaxation of the excited OH stretch vibrations. This signal does not change over the time scale of the experiment (∼1 ns).
The signal decays clearly faster on the red side of the spectrum than on the blue side. In Figure 4.2B we plot the transient absorption changes as a function of delay time at three different probe frequencies. The absorption changes have been corrected for the ingrowing heating signal. The signals are plotted on a

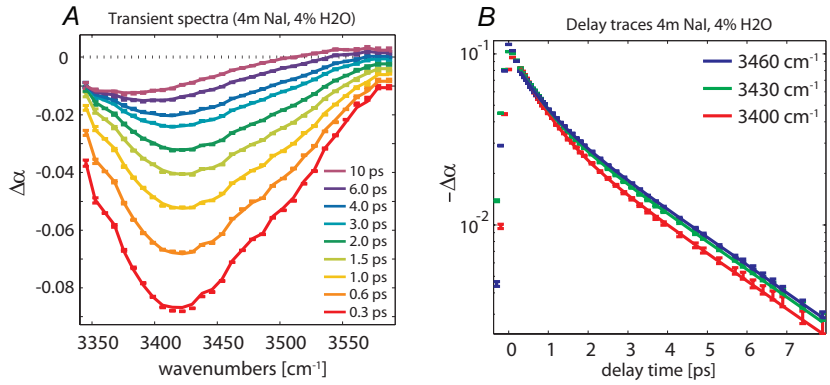

FIGURE 4.2. (A) Transient spectra of a 4 mol/kg NaI solution ($f_H = 0.\ 04$) at delay times of 0.3, 0.6, 1, 1.5, 2, 3, 4, 6 and 10 ps. (B) Heat-corrected delay traces of the same sample at frequencies of 3400, 3430 and 3460 cm^{-1}. The excitation frequency was centered at ∼3430 cm^{-1}.

logarithmic scale to show the strong non-exponential character of the decay. We observe a fast decay within the first two picoseconds, followed by a slower second decay process with a lifetime of several picoseconds. The amplitude of the slow component increases with frequency. We assign the fast component to water-bound HDO molecules showing a vibrational relaxation time constant of 740 fs [61, 62]. The slow component is assigned to the OH groups of HDO molecules forming a hydrogen bond to the I^- anion [46, 47].

4.3.3 THE INFLUENCE OF THE H/D-RATIO ON THE RELAXATION KINETICS

To investigate how the relaxation dynamics depend on the isotopic composition of the sample, we varied the fraction of hydrogen f_H from 0.04 to 1. For a given f_H, the sample thickness was adjusted to give an absorbance of ∼1 unit of optical density (OD) at the maximum of the OH-stretch absorption band. Figure 4.3 we show a comparison between the transient absorption changes for different concentrations of NaI at an elevated H/D-ratio of $f_H = 0.2$. The decay curves in Figure 4.3B have been corrected for the ingrowing heat signal. We observe a clear slow-down of the vibrational relaxation with increasing salt concentration, which can be understood from the increase of the fraction of iodide-bound HDO molecules.

Figure 4.4A shows that an increase of f_H leads to a rise of the final heat-signal relative to the magnitude of the initial bleach. This observation can be understood from the higher density of OH oscillators. For $f_H = 0.25$, 0.5 and 1, the energy of the pump-pulse that is absorbed by the sample is dumped in a smaller volume than in the case of $f_H = 0.04$, leading to a larger rise in temperature and thus to a stronger heating signal. Figure 4.4B shows decay curves that have been corrected for the ingrowing heating signal and reveal the

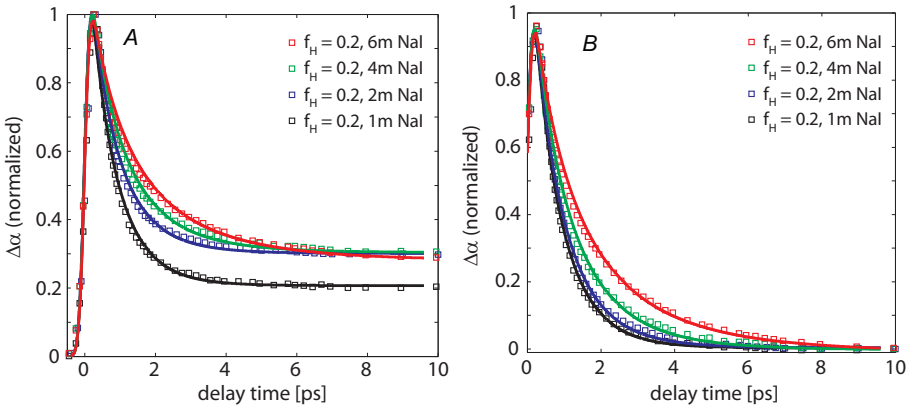

FIGURE 4.3. (A) Transient absorption as a function of delay time for solutions containing 1, 2, 4 and 6 m of NaI and a fraction of hydrogen $f_H = 0.2$. All signals are measured at a probe frequency of 3450 cm^{-1}. The excitation pulses were centered at frequencies between 3400 and 3450 cm^{-1}. The solid lines are obtained with the kinetic model described in the text. Panel (B) shows the transient absorption changes (squares) together with the kinetic model (solid lines) after correction for the time-dependent grow-in of the heating signal. The vibrational relaxation slows down upon increasing the concentration of NaI.

contribution to the decay curves that is due to vibrational relaxation only. A rise in the fraction of hydrogen in the sample clearly leads to an acceleration of the vibrational relaxation, ultimately leading to a nearly complete decay of the signal within 1.5 ps for $f_H = 1$ (dashed red curve). It is clear that neither of the two water components (water-bound and iodide-bound HDO) that were observed for $f_H = 0.04$ can be responsible for this fast decay. It is well known, however, that bulk H_2O-molecules have an extremely short vibrational lifetime of 200 fs [58, 63]. Hence we conclude that the presence of a significant fraction of H_2O-molecules at higher values of f_H opens up an additional, highly efficient vibrational relaxation channel. It is conceivable that the fast component in the decay curves is not only due to H_2O-molecules that are directly excited by the pump pulse, but also represents H_2O molecules that are excited by resonant energy transfer from the other water species in the sample. These other water species may thus employ nearby H_2O molecules to relax their vibrational energy.

4.3.4 FÖRSTER ENERGY TRANSFER

Förster energy transfer has been observed before for isotopic mixtures of neat water [57, 59], and leads to very efficient energy transfer among the hydroxyl stretch vibrations of the most abundant isotopic species. Förster energy transfer leads to a decay of the probability to find the excitation on the originally excited oscillator. Assuming a statistical distribution (radially and orientationally), Förster energy transfer leads to the following time-dependent survival

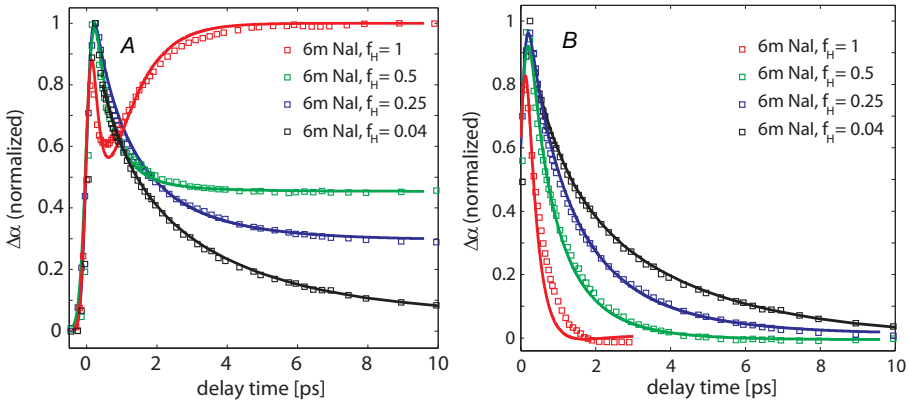

FIGURE 4.4. (A) Transient absorption as a function of delay time for solutions with f_H varying from 0.04 (black squares) to 1 (red squares) and a NaI concentration of 6m. All signals are measured at a probe frequency of 3450 cm^{-1}. The excitation pulses were centered at a frequency of 3450 cm^{-1}. The solid lines are obtained with the kinetic model described in the text. Panel (B) shows the transient absorption changes (squares) and the kinetic model (solid lines) after correction for the time-dependent grow-in of the heating signal. The vibrational relaxation accelerates upon increasing f_H.

probability of the excited oscillator:

$$S(t) = \exp(-\frac{4}{3} \cdot \pi^{3/2} \cdot C_{OH} \cdot \sqrt{R_0^6/T_1}) \tag{4.2}$$

where C_{OH} denotes the number density of the OH-groups, R_0 the Förster-radius and T_1 the pure vibrational relaxation time, unaffected by energy transfer. The term $\sqrt{R_0^6/T_1}$ represents the coupling between the donor and acceptor hydroxyl vibrations. The parameter T_1 enters in this expression to define the Förster radius R_0 as the distance between donor and acceptor for which energy transfer plays a role within the lifetime T_1. Hence, the value of the Förster-radius is referenced with respect to a T_1 value. Here we define the Förster radius R_0 with respect to T_1= 200 fs, the vibrational lifetime of the O-H stretch vibrations of bulk H_2O. We keep this reference T_1 the same in fitting equation Eq. (4.2) to all studied solutions. As a result, the obtained values for R_0 are representative for the magnitudes of the average dipole-dipole couplings of the studied solutions. S(t) is the probability that an initially excited OH-group still remains excited after some time t, i.e. it represents the probability that the excitation has not yet hopped to another OH-group. It should be noted that the description of resonant energy transfer in terms of Eq. (4.2) also accounts for intramolecular energy transfer between OH-groups located on the same molecule, albeit in an approximate manner. Eq. (4.2) is derived assuming a statistical distribution of OH oscillators (with a concentration of 111 M for pure H_2O), that starts at zero donor-accepter distance. Hence, intramolecular energy transfer is represented

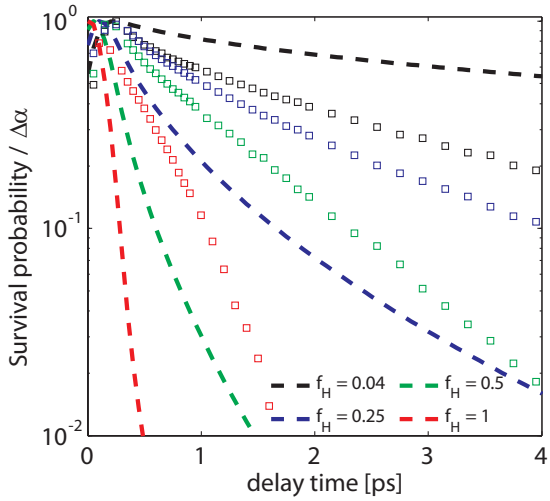

FIGURE 4.5. Comparison of the decay of the survival probability according to Eq. (4.2) (dashed lines), reflecting the energy exchange, and the vibrational relaxation for different fraction of hydrogen, corrected for the grow-in of the heat signal (points). The concentration of NaI is 6 mol/kg for all curves. The vibrational relaxation curves have been normalized to unity for better comparison and the S(t)-curves have been convolved with a Gaussian of fwhm = 250 fs to include the effects of the duration of the laser pulses used in the experiment. Only in the isotopically most dilute sample ($f_H = 0.04$) the vibrational relaxation occurs faster than the exchange of energy.

by the transfer between OH groups at typical mutual distances <2 Å. Obviously, this description is an approximation as the true intramolecular distance of the two O-H groups in H_2O is clearly not statistical.

In Figure 4.5 we show heat-corrected transient absorption changes for a 6 m NaI solution with fractions of hydrogen of $f_H = 0.04, 0.25, 0.5, 1$. We compare these data with the decay of the survival probability according to Eq. (4.2). We use values of $T_1 = 200$ fs and $R_0 = 2.1$ Å from Ref. [57], that were obtained from a pump-probe study on mixtures of HDO:D_2O. We calculate the number density of the accepting OH-oscillators from the given fraction of hydrogen via $C_{OH} = 2 \cdot f_H \cdot N_A \cdot \rho_{H_2O} / M_{H_2O}$, where N_A, ρ_{H_2O} and M_{H_2O} denote Avogadro's constant, the density of liquid H_2O and the molar mass of H_2O, respectively. Figure 4.5 shows that the decay of the survival probability is highly sensitive to the value of f_H. For $f_H = 0.04$, S(t) decays slowly over a timescale of several picoseconds. The comparison with the corresponding transient absorption changes reveals that the decay of the survival probability is slower than the vibrational relaxation, which implies that for $f_H = 0.04$ intermolecular coupling between the OH-groups of the water-bound or iodide-bound HDO-molecules is negligible. When increasing f_H to 0.25, the decay of the survival probability becomes strongly accelerated, leading to a drop to ∼50% of its initial value within the first 500 fs. This finding implies that the excitation undergoes several

'hopping' events from one OH-group to another before it relaxes. The effect of energy exchange on the relaxation dynamics is also notable when comparing the decay curves for different values of f_H (Figure 4.4B). The biexponential behavior that we observe for $f_H = 0.04$ is essentially absent for $f_H = 0.25$, 0.5 and 1. Instead we observe a quasi-monoexponential decay, indicative of an averaging of the lifetimes of different water species in the sample (water-bound HDO/H_2O, iodide-bound HDO/H_2O), a behavior that is caused by the exchange of excitation on a time scale shorter than the vibrational relaxation. We conclude that the rapid exchange of population causes a speed-up of the vibrational relaxation, namely by enabling the water-bound and anion-bound HDO-molecules to transfer their excitation to rapidly relaxing water-bound and anion-bound H_2O molecules.

4.3.5 Modeling the vibrational relaxation for all f_H

From Figures 4.4B and 4.5, it is obvious that the addition of hydrogen does not only lead to an averaging, but also to a strong acceleration of the decay. We wish to establish a global model that is able to describe the experimentally obtained decay curves at any fraction of hydrogen and any concentration of NaI. To this purpose we first need to determine the relative abundance of each of the different water species (anion-bound HDO/H_2O, water-bound HDO/H_2O). The amount of each water species in the sample can be quantified from only two parameters. The first parameter is the equilibrium constant K_{eq} of the isotope exchange reaction of water and heavy water:

$$H_2O + D_2O \longleftrightarrow 2\ HDO \tag{4.3}$$

that has been measured with NMR-spectroscopy [64]. From the equilibrium constant of this reaction, that is defined as,

$$K_{eq} = \frac{[HDO]^2}{[D_2O] \times [H_2O]} = 3.86 \tag{4.4}$$

the amount of each of the three isotopomers in the sample at each f_H can be obtained. The second parameter required to determine the relative abundance of each water species is the hydration number of the iodide ion. We obtain this hydration number from a description that was used in Ref. [46] that accounts for the presence of unoccupied sites in the hydration shell of the iodide ion.

$$K_{iodide} = \frac{[OH \cdots I]}{[I_S] \times [OH \cdots O]} \tag{4.5}$$

where $[I_s]$ denotes the concentration of unoccupied sites in the ion's hydration shell. When the association constant K_{iodide} and the maximum number of water molecules in the first hydration shell are known, the fraction of anion-bound and water-bound OH-groups can be calculated at any concentration of NaI. We use a value for K_{iodide} of 0.25 as used in Ref. [46], and assume a maximum number of 8 water molecules to reside in the hydration shell of the I^- ion. Hence,

$[OH \cdots I]+[I_s] = 8 \times [I^-]$. Eqs. 4.4 and 4.5 are used to calculate the amount of water-bound HDO, anion-bound HDO, water-bound H_2O and anion-bound H_2O. The kinetic model that we employ to describe the experimentally observed relaxation dynamics is illustrated in Figure 4.6. We assume the presence of three excited states, namely water-bound and anion-bound HDO and H_2O (bound to water or to the anion) molecules that have different intrinsic vibrational lifetimes. Each of the three species is allowed to exchange energy with each of the other species via Förster-energy transfer. By differentiation of Eq. (4.2), one obtains the following expression for the time-dependent Förster-rate k_F:

$$k_F(t) = \frac{2}{3} \cdot \pi^{3/2} \cdot C_{OH} \cdot \sqrt{R_0^6/T_1} \cdot t^{-1/2} \tag{4.6}$$

with T_1 = 200 fs and the number density of accepting OH-groups C_{OH} being calculated as outlined in the previous section. The coupled rate-equations are outlined in the appendix and numerically solved by a 4th-order Runge-Kutta algorithm, including the cross-correlate of the pump and probe pulses. The vibrational lifetimes of all three excited states are available from previous studies [47, 61, 63]. Following previous studies on the vibrational relaxation of bulk H_2O [58, 63], we include an intermediate state in the relaxation of H_2O with a lifetime of 800 fs that accounts for the delayed rise of the heat signal. The intrinsic vibrational lifetime of the O-H groups of H_2O molecules that donate one or two hydrogen bonds to I^- ions is not known, as the vibrational relaxation of these species will always be dominated by intramolecular energy transfer and/or energy transfer to the very fast relaxing H_2O molecules that show a T_1 of 200 fs. However, the rapid initial decay of the signal for f_H = 1 of Figure 4.4A shows that the intrinsic T_1 time constant of iodide-bound H_2O molecules must be fast and close to 200 fs. If the T_1 of iodide-bound H_2O would have been significantly longer than 200 fs, the initial decay would have slowed down with increasing iodide concentration, because the initial decay represents the averaged vibrational relaxation of bulk-like and iodide-bound H_2O molecules. We observe a similar rapid initial decay at all studied NaI concentrations and f_H = 1. Therefore, in modeling the data we take the intrinsic relaxation behavior of the I^- bonded H_2O molecules to be the same as for bulk H_2O molecules.

We perform a fit of 20 experimental datasets with a model that employs only a single adjustable parameter, namely the Förster-radius R_0. Figures 4.3A and 4.4A show that the fitted curves are in excellent agreement with the experimental data at all salt concentrations and all fractions of hydrogen. We find the Förster-radius R_0 to depend slightly on the concentration of sodium iodide, having values of 2.5 ± 0.2 Å at 1m and 2m NaI, 2.4 ± 0.2 Å at 4m NaI and 2 ± 0.2 Å at 6m NaI. For comparison, the Förster-radius of neat H_2O was found to be 2.1 Å [57].

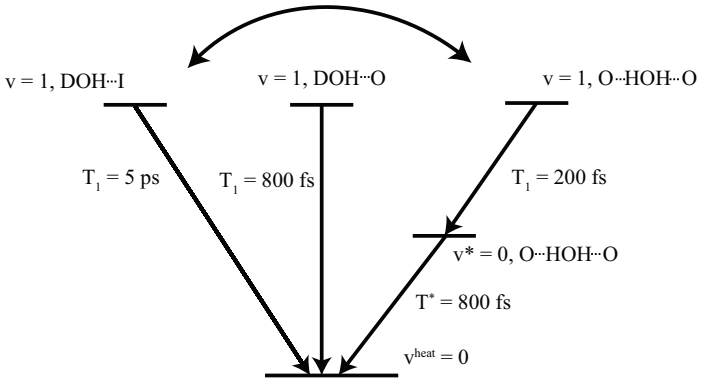

FIGURE 4.6. The kinetic model used to fit the experimental data for f_H = 0.15, 0.2, 0.25, 0.5, and 1, and NaI concentrations of 1, 2, 4, and 6 m. The time-dependent Förster-rate $k_F(t)$ is calculated as outlined in the text. The vibrational T_1 relaxation time constants are obtained from the literature.

4.4 DISCUSSION

We observe that an increase in the fraction of hydrogen leads to an acceleration of the vibrational relaxation of all water OH vibrations present in aqueous solutions of NaI. This acceleration of all water OH groups can be explained from the rapid resonant energy transfer between the different water species and the intrinsically fast relaxation of H_2O. For water hydroxyl groups with an intrinsically slow relaxation like the OH groups of HDO molecules donating a hydrogen bond to I^-, the resonant energy transfer to H_2O opens up an additional efficient relaxation channel. The comparably long relaxation time of the HDO molecules donating a hydrogen bond to I^- has been explained in terms of a reduced anharmonic coupling between the excited OH stretch vibration and the $OH\cdots I^-$ hydrogen-bonding mode [47]. The fast decay of the stretch band of H_2O molecules has been explained by the Fermi-resonance of the OH stretch vibrations with the overtone of the bending mode [63, 65].

In Figure 4.4B it is seen that the fitted curve for f_H =1 (solid red line, representing the convolution of the cross-correlate and the vibrational relaxation with T_1 = 200 fs) deviates from the heat-corrected data points at later delay times. This deviation may originate from the description of the rise of the thermal signal with a single (exponential) time constant. It is conceivable that at salt concentrations as high as 6 mol/kg this assumption is not fully appropriate anymore and that the dynamics of the heat rise are heterogeneous in nature, and should thus be modeled by a distribution of time constants rather than a single time constant.

Our modeling of the resonant energy transfer in terms of the survival probability (Eq. (4.2)) is based on the assumption of a randomly oriented distribution of acceptor molecules. Furthermore, we assume that the transfer of the vibrational excitation occurs irreversibly. The assumption of a statistical distribution

is of course a simplification of the actual physical picture. The validity of these assumptions has been studied in a recent paper by the Skinner group [66]. In this study, it was found that the effects of the reversibility of the energy transfer and the influence of the relative orientation and spatial distribution of the OH oscillators on the rate of resonant energy transfer counteract each other to some extent, making Eq. (4.2) a reasonable approximation to describe the dynamics of Förster energy transfer in liquid water. The rate of resonant energy transfer between different types of oscillators depends on the overlap of the homogeneous lineshapes and the cross sections [67]. The rate of energy transfer from iodide-bound to water-bound water molecules can thus differ from the rate of energy transfer between bulk water molecules. For the iodide bound water, the absorption band is narrower and the cross-section is somewhat larger, leading to an increase of the resonant energy transfer rate. On the other hand, the central frequencies of the OH$\cdots$I and OH$\cdots$O vibrations differ, leading to a decrease of the rate of energy transfer. It is to be expected that these effects more or less compensate each other, thus explaining why the fitted Förster-radius does not change dramatically with increasing NaI concentration. The small decrease of the Förster-radius from 2.5 $\pm$ 0.2 Å at 1m to 2 $\pm$ 0.2 Å at 6m NaI most likely results from a dilution effect: the Na^+ and I^- ions take up space, thereby increasing the average distance between the hydroxyl groups of the water molecules.

4.5 Conclusions

We measured the vibrational relaxation dynamics of the OH-stretch vibration in aqueous solutions of sodium iodide of different isotopic composition. For low fractions of hydrogen ($f_H = 0.04$), we observe two separately decaying water species that we assign to water-bound and iodide-bound HDO molecules. Increasing the hydrogen fraction leads to a drastic change in the relaxation behavior. We observe fast Förster-energy transfer of the vibrational excitation between the different water species present in the sample, i.e. the ion hydration shell and the bulk water. For HDO molecules in the hydration shell of the anion the resonant energy transfer to H_2O molecules opens up a new vibrational relaxation channel that is much faster than the intrinsic vibrational relaxation. Hence, the resonant energy transfer strongly accelerates the vibrational energy relaxation of the anionic hydration shells. For $f_H > 0.25$, the Förster energy transfer is faster than the intrinsic vibrational relaxation rates of all the water species, and a single decay rate is observed that forms a weighted average of the relaxation rates of the different species. We model the data with a kinetic model that includes the Förster energy transfer between the different water species. This model provides an excellent description of the data for all studied NaI concentrations and isotope compositions. From the model we find that the Förster radius decreases from 2.5 $\pm$ 0.2 Å at 1m NaI to 2 $\pm$ 0.2 Å at 6m NaI. This means that the Förster energy transfer becomes somewhat slower at higher salt concentrations, most probably because the average distance between the water

molecules increases as a result of the dilution of water due to the presence of Na^+ and I^- ions.

4.6 APPENDIX

The coupled rate-equations for the relaxation scheme outlined in Figure 4.6 read as follows:

$$\frac{d[DOH\cdots I]}{dt} = -\frac{1}{T_1^{DOH\cdots I}}[DOH\cdots I] - k_F(t)[DOH\cdots I] + k_F(t) f_{DOH\cdots I}([DOH\cdots O] + [DOH\cdots I] + [HOH]) \quad (4.7)$$

$$\frac{d[DOH\cdots O]}{dt} = -\frac{1}{T_1^{DOH\cdots O}}[DOH\cdots O] - k_F(t)[DOH\cdots O] + k_F(t) f_{DOH\cdots O}([DOH\cdots O] + [DOH\cdots I] + [HOH]) \quad (4.8)$$

$$\frac{d[HOH]}{dt} = -\frac{1}{T_1^{HOH}}[HOH] - k_F(t)[HOH] + k_F(t) f_{HOH}([DOH\cdots O] + [DOH\cdots I] + [HOH]) \quad (4.9)$$

$$\frac{d[HOH^*]}{dt} = \frac{1}{T^{HOH}}[HOH] - \frac{1}{T^*}[HOH^*] \quad (4.10)$$

$$\frac{d[v^{heat}=0]}{dt} = \frac{1}{T^*}[HOH^*] + \frac{1}{T^{DOH\cdots I}}[[DOH\cdots I] + \frac{1}{T^{DOH\cdots 0}}[DOH\cdots O] \quad (4.11)$$

Each of the three excited states $[DOH\cdots I]$, $[DOH\cdots O]$ and $[HOH]$ decays with its respective T_1-lifetime. We have used values of $T_1^{DOH\cdots I} = 5$ ps, $T_1^{DOH\cdots O} = 800$ fs, $T_1^{O\cdots HOH\cdots O} = 200$ fs and $T^* = 800$ fs [47, 61, 63]. In addition, each excited state transfers population to the other two excited states via Förster-energy transfer, which is described by the second term in Eqs. (4.7)-(4.9). The time-dependent Förster-rate $k_F(t)$ is calculated according to Eq. (4.6). At the same time, each state gains population from the other excited states according to its relative abundance in the sample. The back transfer is accounted for by the last term in Eqs. (4.7)-(4.9). The relative weighting factors f_i in Eqs. (4.7)-(4.9) are calculated from Eqs. (4.4) and (4.5). Numerical integration of the above rate equations is performed with a 4th-order Runge-Kutta algorithm and yields the population of all involved states at every time

point t. We have introduced a scaling factor of 2.5 for the contribution of H_2O molecules at all salt concentration and fractions of hydrogen to account for the larger absorption cross-section of this species in comparison to water-bound and iodide-bound HDO.

5 Dynamics of water molecules in DMSO and acetone

We study the vibrational relaxation dynamics and the reorientation dynamics of HDO molecules in binary water-dimethylsulfoxide (DMSO) and water-acetone mixtures with polarization-resolved femtosecond mid-infrared spectroscopy. For low solute concentrations we observe a slowing down of the reorientation of part of the water molecules that hydrate the hydrophobic methyl groups of DMSO and acetone. For water-DMSO mixtures the fraction of slowed-down water molecules rises much steeper with solute concentration than for water-acetone mixtures, showing that acetone molecules show significant aggregation already at low concentrations. At high solute concentrations, the vibrational and reorientation dynamics of both water-DMSO and water-acetone mixtures show a clear distinction between the dynamics of water molecules donating hydrogen bonds to other water molecules and the dynamics of water donating a hydrogen bond to the S=O/C=O group of the solute. For water-DMSO mixtures both types of water molecules show a very slow reorientation. The water molecules forming hydrogen bonds to the S=O group reorient with a time constant that decreases from 46±14 ps at X_{DMSO}=0.33 to 13±2 ps at X_{DMSO} = 0.95. The water molecules forming hydrogen bonds to the C=O group of acetone show a much faster reorientation with a time constant that decreases from 6.1±0.2 ps at X_{acet} = 0.3 to 2.96±0.05 ps at X_{acet} = 0.9. The large difference in reorientation time constant of the solute-bound water for DMSO and acetone can be explained from the fact that the hydrogen bond between water and the S=O group of DMSO is much stronger than the hydrogen bond between water and the C=O group of acetone. We attribute the strongly different behavior of water in DMSO-rich and acetone-rich mixtures to their difference in molecular shape.

5.1 Introduction

Both acetone and DMSO molecules are polar, amphiphilic molecules possessing hydrophobic groups in the form of two methyl-groups. Despite their

apparent similarity in terms of their molecular formula, acetone and DMSO show large differences in many of their physical properties such as the dipole moment (μ(DMSO) = 3.96 D, μ(acetone) = 2.9 D), the dielectric constant ($\epsilon(DMSO) = 48$, ϵ(acetone) = 21) [68] and the phase transition temperatures (T_{melt}(acetone) = -94.5°C, T_{melt}(DMSO) = 18.5°C, T_{boil}(acetone) = 56°C, T_{boil}(DMSO) = 191.6°C) [69]. These differences likely find their origin in the different structures of DMSO and acetone. The geometry of DMSO differs from that of acetone due to the presence of a lone electron pair on the sulphur atom of DMSO, causing the molecule to adapt a trigonal-bipyramidal shape, which implies that the S=O group is tilted out of the C-S-C plane. For acetone the C=O group is in the C-C-C plane, making the molecule essentially planar.

Aqueous solutions of both compounds have long been known to show highly non-ideal behavior, exhibiting a strongly non-linear behavior with sample composition in various physicochemical properties such as the enthalpy of mixing [70, 71], the viscosity [72, 73], the dielectric relaxation times [74, 75] and the self-diffusion coefficients [76, 77]. For example, a water-dimethylsulfoxide (DMSO) mixture with a molar fraction $X_{DMSO} = 0.33$ ($X_{wat} = 0.67$) has a freezing point of -70 °C [78], whereas pure water and DMSO have freezing points of 0 and 17 °C. This latter property, together with DMSO's ability to permeate the cell wall [79], has led to its widespread use as a cryoprotective agent in many cell-biological and medical applications [78, 80–83]. At the same time, the ability to penetrate the cell-wall has also been linked to the neurotoxic effects of DMSO [84].

The deviation from ideal behavior indicates that the aqueous mixtures of both compounds are strongly affected by hydrogen-bonding interactions with water molecules. Especially for DMSO-water mixtures, evidence for strong associative interactions has been found, and the non-ideal behavior has been explained from the formation of stable DMSO-water complexes with a well-defined stoichiometry of 1:1 or 1:2 [85–87]. The exact structure of such complexes is still a matter of debate. Using molecular dynamics simulations, Borin and Skaf [85] observed the prevalence of 1:2 DMSO-water complexes with both water molecules donating a hydrogen bond to the S=O group over a large composition range, only at low water content a stronger tendency for water molecules to bridge two DMSO-molecules via hydrogen bonds was found. Neutron diffraction studies of water-DMSO mixtures [88] and simulation work based on molecular dynamics [86, 87] came to similar conclusions. In contrast, electronic structure calculations by Reiher and co-workers [89] showed that the most stable configuration of 1:2 DMSO-water complexes is formed by a configuration in which the oxygen atom of the S=O group acts as a hydrogen-bond acceptor for only one water molecule, with the second water molecule binding preferentially to this water molecule. In recent work employing two-dimensional infrared and optical Kerr-effect spectroscopy, Wong *et al.* showed that the spectral diffusion dynamics and reorientation of water molecules are significantly affected by the presence of DMSO, and it was suggested that the observed dynamics are linked to the collective reorientation of solute-solvent complexes [90].

Molecular dynamics simulations and far-infrared absorption experiments

have provided evidence that water-acetone mixtures possess a less associative character than water-DMSO mixtures and instead tend to segregate into solute and solvent clusters [91, 92]. A comparative neutron-scattering and molecular-dynamics simulation study of aqueous DMSO and acetone solutions [93] came to similar conclusions, and the differences between binary aqueous DMSO and acetone solutions were explained from differences in the strength of the hydrogen bonds formed between water and the solute molecules. However, other studies found evidence for the presence of an essentially random distribution of water molecules in acetone [94, 95].
Here, we report on a femtosecond infrared study of the hydrogen-bond dynamics in the binary mixtures of water-acetone and water-DMSO over a wide composition range. We study the isotropic and anisotropic vibrational dynamics of water molecules in these mixtures with molar fractions of water X_{wat} ranging from 0.05 to 1, thereby covering both the situation where acetone and DMSO act as a solute in a dilute aqueous solution (low X_{sol}), and the regime of high X_{sol}, where acetone and DMSO act as a solvent and water molecules take the role of the solute.

5.2 Experiment

We measure the vibrational relaxation dynamics of the OD stretch vibration of HDO molecules in binary water-acetone and water-DMSO mixtures with molar fractions of solute in the range X_{sol} = 0 - 0.95. The femtosecond pulses required for this study are generated by a series of nonlinear frequency conversion processes that are pumped with the pulses of a commercial Ti:sapphire regenerative amplifier (Spectra-Physics Hurricane). The amplifier system delivers 100 fs-pulses centered around 800 nm with a pulse energy of 0.8 mJ. About 500 μJ of the amplifier output is split off to pump a white-light seeded optical parametric amplifier (OPA, Spectra Physics) based on β-barium borate (BBO), generating signal and idler pulses with a wavelength around 1333 nm and 2000 nm, respectively. The idler pulses are frequency-doubled in a second BBO-crystal, and the resulting pulses are used as a seed for parametric amplification in a lithium niobate ($LiNbO_3$) crystal pumped by the remaining 300 μJ of 800 nm pulses, leading to the generation of mid-infrared pulses with a wavelength of 3.8 - 4 μm (2500 - 2600 cm^{-1}) and a duration of 180 fs. The mid-infrared pulses have a pulse energy of 7 - 9 μJ and a spectral width of approximately 115 cm^{-1}.
The generated mid-infrared pulses are used in a pump-probe experiment as described in Section 3.1. The samples consisted of aqueous (8% HDO:H_2O) mixtures of acetone or DMSO, and were held between two CaF_2 windows separated by Teflon spacers with thicknesses ranging from 50 to 500 μm. Acetone ($\geq$ 99% purity, HPLC-grade) and DMSO (water-free, 99.9 % purity) were obtained from Sigma Aldrich and were used without further purification.

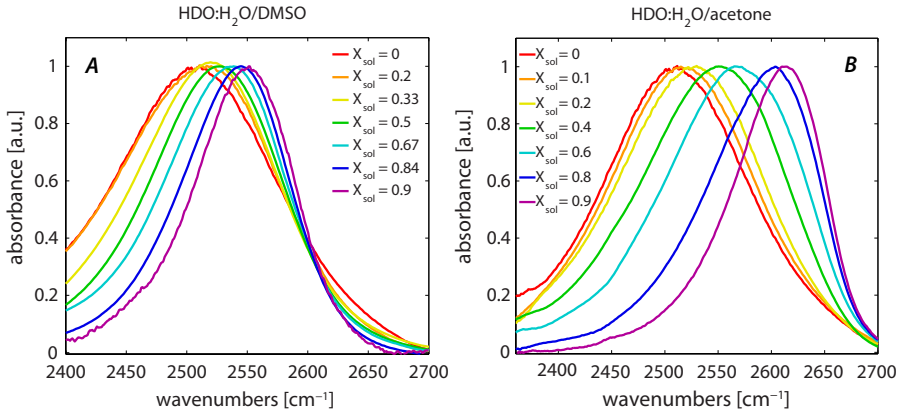

FIGURE 5.1. Linear absorption spectra of the OD-stretch region of solutions of (A) DMSO and (B) acetone in 8% HDO:H_2O for various sample compositions. The spectra in panel (A) and (B) have been corrected for the solvent background by subtracting the absorption spectrum of either neat H_2O or a solution of H_2O in DMSO or acetone. The latter procedure has been applied to samples with $X_{sol} \geq 0.2$ in order to properly subtract resonances around 2575 - 2650 cm^{-1}, that arise from either acetone or DMSO molecules and the exact resonance frequency of which is sensitive to sample composition and hence to X_{sol}.

5.3 RESULTS AND DISCUSSION

5.3.1 LINEAR INFRARED SPECTRA

In Figure 5.1 we show FTIR-spectra of the OD-stretch region of solutions of either acetone or DMSO in 8% HDO:H_2O over the whole concentration range studied, i.e. for molar fractions of solute X_{sol} ranging from 0 to 0.9. For both solutes, the width of the OD-stretch absorption band is independent of solute concentration for $X_{sol} \leq 0.2$, and has approximately the same value (fwhm $\approx$ 155 cm^{-1}) as for neat HDO:H_2O. This observation indicates that the dissolution of modest quantities of acetone or DMSO does not lead to a severe disruption of the hydrogen-bond network of water. Increasing the molar fraction of the solute causes a pronounced blueshift of the OD-stretch absorption band, which is generally attributed to a weakening of the hydrogen-bond strength of water. The blueshift is accompanied by a reduction in linewidth down to approximately 85 cm^{-1} and 95 cm^{-1} full width at half maximum at $X_{sol} = 0.9$ for water-DMSO and water-acetone, respectively, suggesting that the distribution of hydrogen-bond strengths in the mixtures becomes substantially less inhomogeneous with increasing solute fraction. For HDO molecules in water-acetone, the OD-stretch absorption band becomes increasingly asymmetric with increasing acetone content, whereas for water-DMSO solutions the band retains a Gaussian shape at all compositions.

5.3.2 Nonlinear infrared spectra and vibrational relaxation dynamics

Figure 5.2 shows transient absorption spectra of the OD-stretch vibration of HDO-molecules in aqueous DMSO ($X_{sol} = 0.06$) and acetone ($X_{sol} = 0.05$) solutions for delay times ranging from 0.5 ps to 20 ps. The transient spectra show a negative response that peaks around 2500 - 2510 cm^{-1}, originating from the bleaching of the ground state ($\nu = 0$) and stimulated emission from the first excited state ($\nu = 1$) of the oscillator. The positive feature in the transient spectrum observed on the red side of the spectra originates from excited state absorption ($\nu = 1 \rightarrow 2$). The spectra at late delay times have the shape of a temperature-difference spectrum and result from the thermalization of the vibrational excitation and the energy redistribution over low-frequency degrees of freedom. We find that the data can be well described by a model in which the excited state of the OD-stretch vibration relaxes via an intermediate state to the heated ground state. The intermediate state is included in this model to account for the delayed rise of the thermal signal with respect to the decay of excited state of the OD-stretch vibration. We assume that the intermediate state has the same absorption spectrum as the ground state, meaning that its associated (differential) transient absorption spectrum equals zero at all frequencies. Relaxation from the intermediate state to the ground state likely represents the adaptation of the hydrogen bonding network to the dissipation of the energy of the vibrational excitation. This model has been successful in describing the vibrational relaxation dynamics of the OD-stretch band in neat HDO:H_2O [56,96], and has also been successfully applied to describe the relaxation of the same mode in aqueous solutions of small, amphiphilic solutes [97].

The results of the fits are shown in Figure 5.2(C,D). This figure shows the vibrational relaxation time T_1 of the OD-stretch vibration of HDO-molecules in water-acetone and water-DMSO mixtures as a function of X_{sol}. We observe that with increasing concentration of either solute, the vibrational lifetime increases from 1.65 ps ($X_{sol} = 0$) to 2.66 ps at $X_{sol} = 0.22$ (water-DMSO) and to 2.55 ps at $X_{sol} = 0.2$ (water-acetone), respectively. The gradual increase in T_1 with increasing concentration of solute agrees with the results of previous studies of aqueous solutions of other amphiphilic molecules of comparable size, such as tetramethylurea, proline and N-methylacetamide [98]. The vibrational lifetimes of Figure 5.2C also agree well with the lifetimes recently reported by Wong *et al.* [90].

In Figure 5.3 we show isotropic transient absorption changes of the OD-stretch vibration of HDO-molecules with DMSO and acetone in large excess ($X_{sol} = 0.9$). The maximum of the bleaching signal is clearly shifted to higher frequencies, when compared to the transient spectra in Figure 5.2. The shifts in the transient spectra of 100 cm^{-1} in the case of water-acetone (Figure 5.3B) and 50 cm^{-1} in the case of water-DMSO (Figure 5.3A) are consistent with the blueshifts of the OD-stretch absorption band in the linear spectra shown in Figure 5.1(A,B). The transient spectra in Figure 5.3 show a pronounced slowing down of the vibrational relaxation of the OD-stretch vibration compared

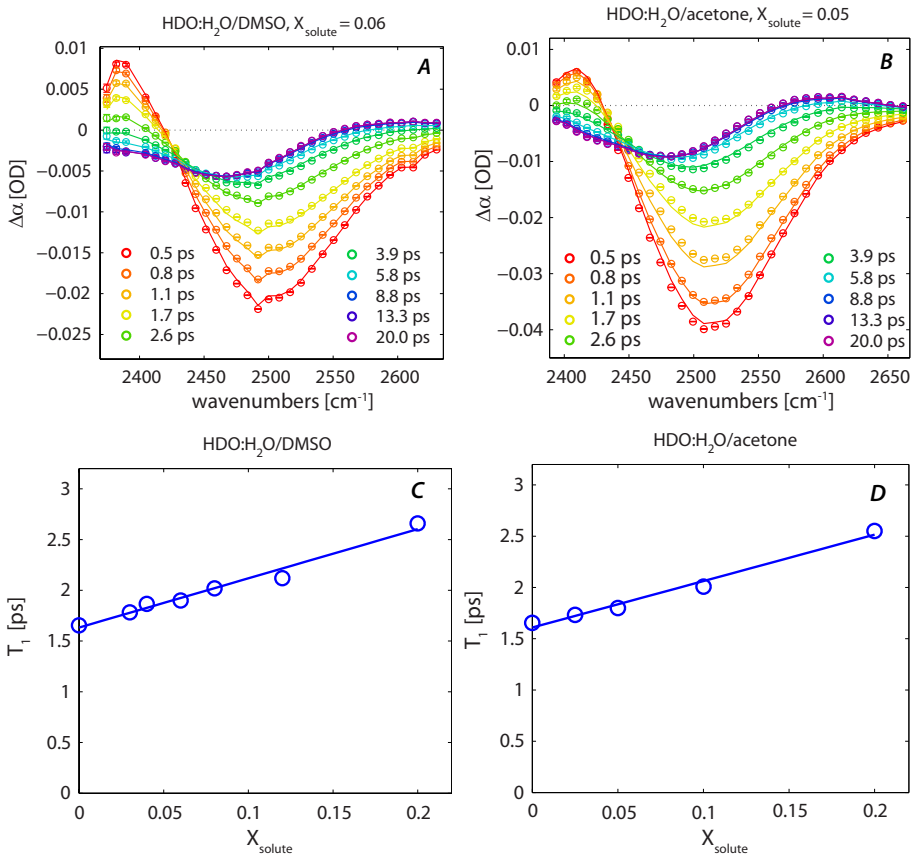

FIGURE 5.2. Isotropic transient spectra of (A) water-DMSO solutions with X_{sol} = 0.06 and (B) water-acetone solutions with X_{sol} = 0.05. Open circles are datapoints and solid lines are a fit to the model outlined in the text. Panel (C) and (D) show the vibrational lifetimes of the OD-stretch vibration (T_1-times) that have been extracted from the fit of the model outlined in the text to the experimental datasets obtained from water-DMSO and water-acetone mixtures, respectively. The solid lines in panel (C) and (D) are a guide to the eye.

to Figure 5.2(A,B). The transient spectra of Figure 5.3 also show a blueshift with increasing delay time, suggesting the presence of subensembles of HDO-molecules exhibiting different vibrational lifetimes. In order to account for the presence of different water species, we fit the data of Figure 5.3(A,B) with a model that includes two excited states that relax to a common, heated ground state. We employ this model in the analysis of all water-acetone and water-DMSO data sets with $X_{sol} > 0.2$. The initial populations of the two excited states are allowed to vary in the minimization routine, while the spectral amplitudes are constrained to be equal. This description provides an excellent

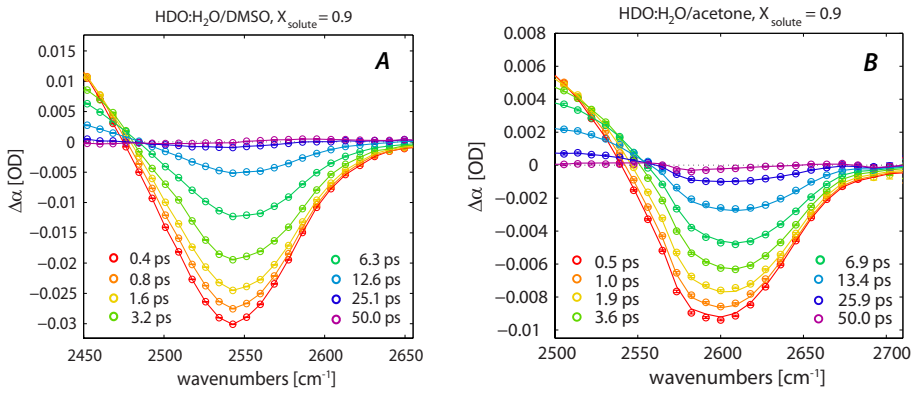

FIGURE 5.3. Isotropic transient spectra of (A) water-DMSO solutions with X_{sol} = 0.9 and (B) water-acetone solutions with X_{sol} = 0.9. The open circles represent the data points and the solid lines are a fit to the model described in the text.

description of the transient spectral data at all delay times, which shows that the inhomogeneity of the absorption band persists within the experimental time window of ∼10 ps. Hence, there is no rapid exchange between the water species that are associated with the two excited states.

In Figure 5.4(A,B) the initial populations and vibrational lifetimes of the two excited states are plotted as a function of X_{sol} for water-acetone and water-DMSO solutions. The increase of the relative amplitude of the high-frequency bands with increasing solute content, as seen in Figure 5.4A, strongly suggests that the high-frequency bands represent HDO molecules forming hydrogen bonds to the solute. Indeed in previous neutron scattering and molecular dynamics simulation studies a strong tendency for water molecules to bind to the S=O groups of DMSO was found [85,88]. Likewise, we assign the high-frequency band of OD-oscillators in water-acetone mixtures to water molecules forming hydrogen bonds to the C=O groups. For both water-DMSO and water-acetone the vibrational relaxation time constant of the lower frequency band varies in the range 1.5 to 2 ps (Figure 5.4B), and is thus comparable to the relaxation rate of the OD-stretch vibration of neat HDO:H_2O. We therefore assign this band to HDO-molecules having their OD-groups hydrogen bonded to the oxygen atom of other water molecules. The relaxation time constants associated with the high frequency bands are significantly longer and increase monotonically from approximately 4 ps around X_{sol} = 0.3 to 8 ps at X_{sol} = 0.95 for water-DMSO solutions and to 13 ps at X_{sol} = 0.9 for water-acetone solutions. The relatively high frequency and slow relaxation dynamics of these bands indicate that the hydrogen bonds between water and the solute are relatively weak. The more pronounced slowing down of the vibrational relaxation together with the stronger blueshift of C=O bound waters compared to S=O bound waters in Figures 5.1 and 5.3 indicate that water molecules hydrating the C=O groups of acetone form much weaker hydrogen bonds than water molecules hydrating

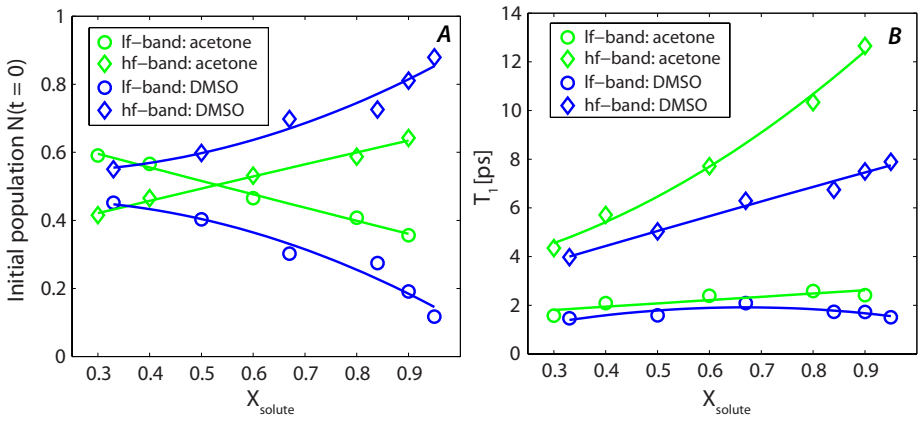

FIGURE 5.4. Fitresults obtained from the isotropic transient absorption data of water-acetone and water-DMSO solutions with X_{sol} = 0.3 - 0.95. (A) Integrated spectral amplitude of the bleaching signal of the two components used in the fit of the isotropic transient absorption changes $\Delta\alpha_{iso}(\omega, t)$. (B) Vibrational relaxation times obtained from the fit. Solid lines are a guide to the eye.

the S=O group of DMSO. This observation is in agreement with the results obtained from calorimetric studies, where an excess enthalpy of mixing of about -2.5 kJ/mol for water-DMSO solutions at X_{DMSO}= 0.33 was reported [70]. Water-acetone mixtures were found to exhibit a maximum negative excess enthalpy of mixing of only -0.67 kJ/mol at X_{acet}= 0.15 [99].

The relative amplitude of the high-frequency band is consistently lower for water-acetone than for water-DMSO solutions. For water-acetone solutions, the amplitude of the low-frequency band, representing HDO molecules bound to other water molecules, is quite large even at $X_{sol} = 0.9$ ($X_{wat} = 0.1$). For the water-DMSO solution this amplitude strongly decreases with increasing solute concentration, and is only 0.1 at $X_{sol} = 0.9$. This finding agrees with the linear absorption spectra in Figure 5.1, where it is seen that the OD-stretch band of water-acetone has a noticeably asymmetric lineshape at $X_{sol} = 0.9$, exhibiting a shoulder on the low-frequency side around ~ 2550 cm^{-1}, while the OD-stretch vibration in water-DMSO shows a nearly symmetric, gaussian lineshape.

The large differences between the amplitudes of the spectral bands of the water-acetone and water-DMSO solutions in the range of X_{sol} = 0.3 - 0.95 can be explained from the different mesoscopic structures of the solutions. Our results suggest that in water-acetone solutions water clusters already form at high X_{sol} (= low X_{wat}), leading to a higher fraction of water-molecules hydrogen bonded to other water molecules and a correspondingly lower fraction of water molecules that are hydrogen bonded to C=O. For water-DMSO solutions, the amplitudes of the water-bound and S=O bound water molecules show a concentration dependence that is to be expected in the case of homogeneous mixing, meaning that this system will be far less (microscopically) segregated.

For both water-DMSO and for water-acetone we find that the vibrational relaxation of the OD stretch vibration strongly slows down with increasing solute fraction X_{sol}. This slowing down of the vibrational relaxation can partly be explained from the increased fraction of water molecules that are hydrogen bonded to the S=O and C=O groups. These hydrogen bonds are weaker than between water molecules, which implies that the anharmonic coupling between the OD stretch vibration and the hydrogen bond will be weaker. In addition, with increasing solute fraction it becomes more likely that both hydroxyl groups of these water molecules are bonded to S=O or C=O groups, and it becomes less likely that these water molecules accept hydrogen bonds from other water molecules. Molecular dynamics simulations of water-acetone mixtures [91] and water-DMSO mixtures [85, 86] showed that the number of accepted hydrogen bonds per water molecule decreases with increasing solute fraction. The reduced probability of water-water hydrogen bonds is expected to lead to a decrease in the density of accepting modes of the excited hydroxyl stretch vibration, thus causing a decrease in the relaxation rate of water molecules that are hydrogen bonded to C=O or S=O groups, as seen in Figure 5.4B. This scenario is similar to the one recently proposed by Wong *et al.* in their study on the vibrational dynamics of water-DMSO solutions [90].

5.3.3 Water reorientation dynamics at low solute fractions

In Figure 5.5(A,B) the anisotropy decay of the OD-stretch vibration of HDO-molecules is presented for the composition range X_{sol} = 0.0 - 0.2. The data have been corrected for the rise of the thermal end level, where we assumed the final heated state to be isotropic. The addition of DMSO or acetone leads to the appearance of a slow component in the decay of the anisotropy, which shows very little decay on a timescale of 8 picoseconds. The amplitude of this component scales with the concentration of solute. This slow component is reminiscent of the slow reorientation component that has been observed in the anisotropy decay of water molecules in the vicinity of hydrophobic groups [97,98]. Therefore we assign the slow component of Figure 5.5(A,B) to water molecules hydrating the hydrophobic methyl groups of DMSO and acetone. The anisotropy curves can be well described by a function of the form $R(t) = R_1 \cdot \exp(-t/\tau_{or}) + R_0$. In Figure 5.5(C,D) we plot the reorientation time constants that we obtain by fitting this function to the data in Figure 5.5(A,B). For both DMSO and acetone, the values of τ_{or} are very similar to the reorientation time constant of 2-2.5 ps of the OD-stretch vibration in neat HDO:H_2O [56, 96]. This finding indicates that the reorientation dynamics are bimodal: a fraction of the water molecules is strongly slowed down in its reorientation by the presence of the solute, whereas the other water molecules are essentially unaffected and exhibit reorientation dynamics comparable to that of water molecules in neat liquid water.

In Figure 5.6, we plot the ratio of the amplitude of the slow water fraction and the total amplitude of the anisotropy, R_0/R_0+R_1, as a function of

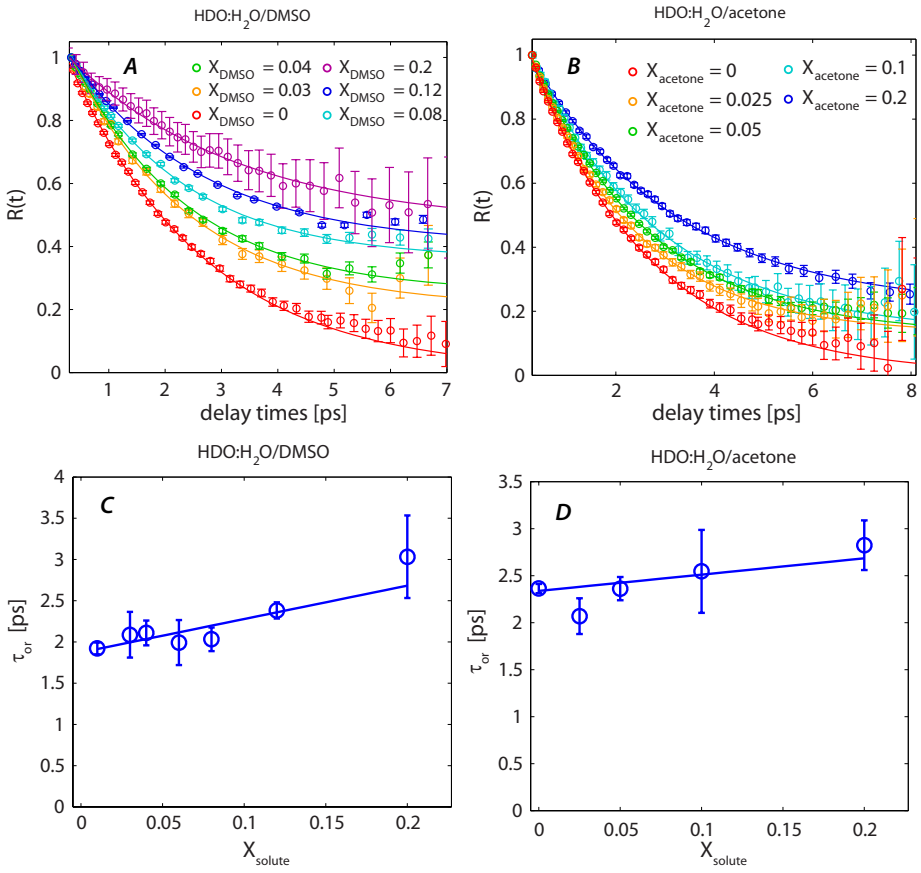

FIGURE 5.5. Anisotropy decay of the OD-stretch vibration of HDO-molecules in (A) water-DMSO and (B) water-acetone mixtures. The data represent an average over 40 cm^{-1}around the center frequency of the bleach. Open circles represent experimental data points that have been corrected for the time-dependent rise of the thermal endlevel, solid lines are fits to a function of the form $R(t) = R_1 \cdot \exp(-t/\tau_{or}) + R_0$. The reorientation time constants τ_{or} obtained from the fits of the data in panel (A) and (B) are plotted in panel (C) and (D), respectively. The solid lines in panel (C) and (D) are a guide to the eye.

X_{sol}. These amplitudes have been obtained from fitting the anisotropy curves in Figure 5.5. We find that the amplitude of the slow-water fraction of aqueous DMSO solutions is consistently larger than the amplitude of the slow water fraction in aqueous acetone solutions of the same X_{sol}. This result is surprising, since both solute molecules possess two hydrophobic methyl groups. In a previous femtosecond infrared study, in which the orientational dynamics of water around amphiphilic molecules with different numbers of hydrophobic groups over a similar concentration range as in Figure 5.6 was studied, the fraction of

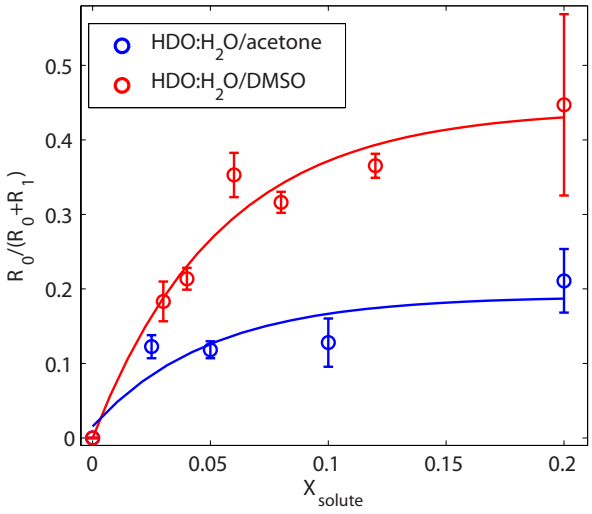

Figure 5.6. Normalized amplitude of the slow water fractions obtained from the anisotropy decays of Figure 5.5(A,B) as a function of X_{sol} for binary mixtures of water and DMSO (red open circles) as well as water and acetone (blue open circles). Solid lines are a guide to the eye.

slowed down water molecules was found to scale linearly with the number of solute methyl groups [97]. The data in Figure 5.6 suggest that in aqueous acetone solutions less water molecules are exposed to the hydrophobic methyl groups than in DMSO solutions. This result indicates that acetone molecules tend to aggregate already at low solute concentrations, thereby reducing the number of methyl groups interacting with water. This interpretation agrees well with results from neutron scattering studies of an acetone-water mixture with $X_{acet} = 0.05$ [93], and with results from molecular dynamics simulations [92].

5.3.4 Water reorientation dynamics at high solute fractions

In Figure 5.7, we plot the decay of the anisotropy of the OD-stretch vibration of HDO-molecules in aqueous DMSO and acetone solutions for a broad composition range $0.1 \leq X_{sol} \leq 0.9$. The data have been obtained by averaging over a spectral range of 70 cm^{-1} to 100 cm^{-1} of the bleaching signal of the parallel and perpendicular transient absorption spectra. For DMSO we observe the slowest anisotropy decay in the range of $X_{DMSO} = 0.33$ - 0.5. This finding agrees with the results of several previous studies that suggested that water and DMSO molecules can form very stable clusters in this composition range. It thus appears likely that the maximum slow-down of water molecules at X_{DMSO}= 0.33 - 0.5 finds its origin in the formation of stable 1:2 DMSO-water

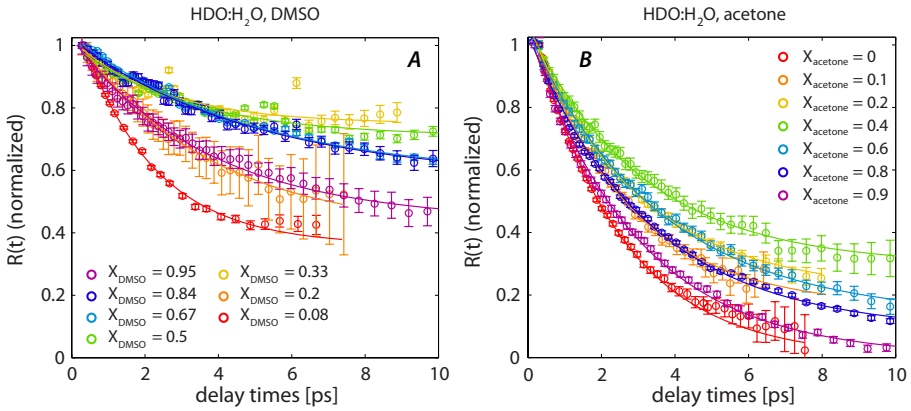

FIGURE 5.7. (A) Normalized anisotropy decay of the OD-stretch vibration of HDO molecules in aqueous DMSO solutions for X_{sol} = 0.1 - 0.95 . The data have been averaged over a range of $\sim$ 70 - 90 cm^{-1} of the bleaching signal of the transient absorption spectra. (B) Normalized anisotropy decay of the OD-stretch vibration of HDO molecules in aqueous acetone solutions for X_{acet} = 0.1 - 0.9. The data have been averaged over a range of $\sim$ 100 cm^{-1} of the bleaching signal of the transient absorption spectra. The solid lines are serve as a guide to the eye.

clusters. A further increase of the DMSO concentration is observed to result in a moderate acceleration of the anisotropy decay. It is also seen that the anisotropy decay becomes more single exponential, i.e. less bimodal. It followed from the isotropic data (Figure 5.4A) that for large X_{DMSO} values the signals are dominated by the response of HDO molecules bound to the S=O groups of DMSO. Hence, in the range of X_{DMSO} = 0.33 - 0.8, the anisotropy curves of Figure 5.7A represent a gradual transition from the regime of hydrophobic hydration to a regime where the hydrogen-bonding interaction with the S=O moiety of DMSO starts to determine the anisotropy dynamics. The solute fraction at which we observe the maximum slow-down of water molecules in water-DMSO solutions (X_{DMSO}= 0.33) matches very well with the composition at which theoretical and experimental self-diffusion coefficients show a minimum [76, 85], and the composition at which the viscosities [72] and the dielectric relaxation times [74] show a maximum. The observation of a maximum slowing down in dynamics at a particular composition agrees with the results obtained for the spectral diffusion and reorientation dynamics of water molecules in water-DMSO mixtures reported by Wong *et al.* [90].

For water-acetone mixtures (Figure 5.7B) the anisotropy decay is observed to slow down with increasing solute concentration in the range of X_{acet} = 0 - 0.4, but becomes faster again for higher X_{acet}. For X_{acet} = 0.9 the anisotropy decay is even similar to the anisotropy decay of pure water (X_{acet} = 0). The composition of water-acetone mixtures, at which we find the slowest anisotropy decays of water molecules in Figure 5.7B (X_{acet} = 0.4) is somewhat different

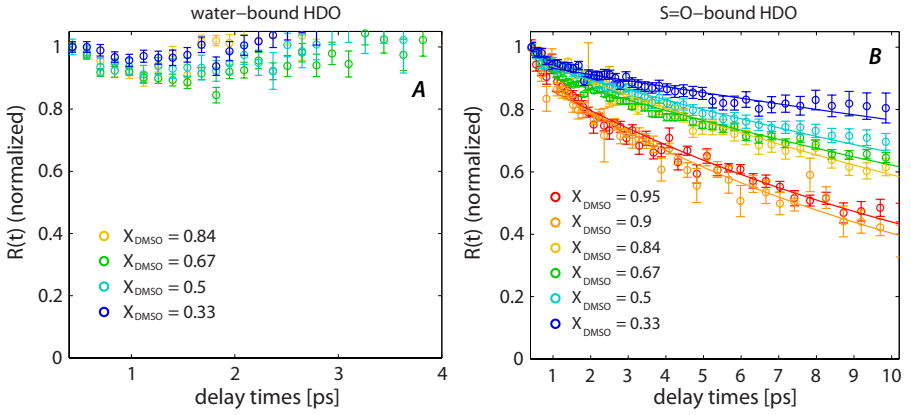

FIGURE 5.8. Anisotropy decays of water-DMSO solutions associated with the low- and high-frequency bands of which the amplitudes and T_1 time constants are shown in Figure 5.4. Panel (A) shows the decay of the anisotropy of the OD-group of HDO-molecules with their OD-group hydrogen bonded to other water molecules for X_{DMSO} = 0.33 - 0.84, and panel (B) shows the decay for HDO-molecules having their OD-groups hydrogen bonded to the S=O group of DMSO. The anisotropy decays in this figure have been obtained by the decomposition of the polarization resolved transient absorption changes as outlined in the text. The solid lines in panel (B) are monoexponential fits.

from the composition at which the self-diffusion coefficient of water molecules has a minimum, which occurs around $X_{acet} = 0.2$ as determined by NMR-spin echo experiments [77, 100].

Since the anisotropy decays are obtained from an average over the bleaching signal, they represent the response of *all* types of water molecules in the sample, i.e. water molecules forming hydrogen bonds to other water molecules and water molecules forming hydrogen bonds to the S=O groups of DMSO and the C=O groups of acetone. As these different types of water molecules show different spectral responses, we can disentangle their contributions to the anisotropy dynamics. We use the spectral bands that we obtained from fitting the isotropic transient absorption changes $\Delta\alpha_{iso}(\omega, t)$ of water-DMSO and water-acetone mixtures with $X_{sol} \geq 0.3$, to perform a decomposition of the polarization-resolved data sets $\Delta\alpha_{\parallel}(\omega, t)$ and $\Delta\alpha_{\perp}(\omega, t)$. The resulting amplitudes of the two spectral bands in $\Delta\alpha_{\parallel}(\omega, t)$ and $\Delta\alpha_{\perp}(\omega, t)$ at different time delays are used to construct the anisotropy dynamics of the two bands. A detailed outline of the procedure and exemplary spectral bands for water-bound and S=O/C=O-bound HDO molecules are given in the appendix of this chapter, respectively.

For water-DMSO mixtures, the spectral response of the low-frequency band becomes quite small at high DMSO mole fractions, as seen in Figure 5.4A, which makes the determination of the anisotropy of the low-frequency band very noisy.

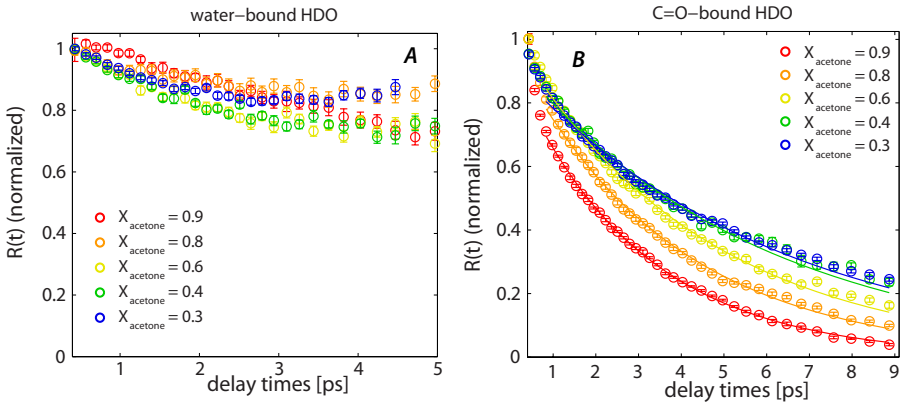

FIGURE 5.9. Anisotropy decays of water-acetone solutions at X_{acet} = 0.3 - 0.9. Panel (A) shows the decay of the anisotropy of the OD-group of HDO-molecules with their OD-group hydrogen bonded to other water molecules, and panel (B) shows the corresponding decay for HDO-molecules having their OD-groups weakly hydrogen bonded to acetone. The anisotropy decays in this figure have been obtained by the decomposition of the polarization resolved transient absorption changes as outlined in the text. The solid lines in panel (B) are monoexponential fits.

For $X_{DMSO} \geq 0.9$ the transient absorption is dominated by the high-frequency band and its anisotropy can still be well determined. In Figure 5.8 we present the anisotropy decay of the low-frequency water-bound band up to $X_{DMSO} = 0.84$ and the anisotropy decay of the high-frequency band up to $X_{DMSO} = 0.95$. The anisotropy $R_{WW}(t)$ of the low-frequency water-bound band (Figure 5.8A) is more or less constant, which means that the water-bound water molecules in water-DMSO mixtures show very little reorientation in the measured delay-time interval. An analysis of the dynamics for delay times longer than 4 ps is obstructed by the comparably short vibrational lifetime of this type of water molecules ($T_1 \approx 2$ ps) and its relatively small amplitude (Figure 5.4A). The anisotropy $R_{WD}(t)$ of the high-frequency S=O group bound water molecules (Figure 5.8B) shows a slow exponential decay that becomes somewhat faster with increasing X_{DMSO}. The time constants of the reorientation are shown in Figure 5.10. The time constant decreases from 46±14 ps at $X_{DMSO} = 0.33$ to 13±2 ps at $X_{DMSO} = 0.95$.

The results of the decomposition analysis for the water-acetone mixtures are shown in Figure 5.9. In this figure we present the anisotropy decays $R_{WW}(t)$ of water-bound HDO-molecules (Figure 5.9A) and $R_{WA}(t)$, the anisotropy decay of HDO-molecules that are hydrogen bonded to the C=O groups of acetone molecules (Figure 5.9B). $R_{WW}(t)$ shows only a partial decay to about 80 - 90 % of the initial value within the first 4 ps. The results in Figure 5.9A show that water molecules that are hydrogen bonded to other water molecules, are strongly impaired in their reorientation. It is likely that these water molecules

are present in the form of small water clusters, which agrees with the fact that the vibrational lifetime of these water molecules is similar to that of neat water (Figure 5.4). The anisotropy $R_{WA}(t)$ of the C=O bound water shown in Figure 5.9B is much faster than that of the S=O bound water shown in Figure 5.8B. This difference can be explained from the fact that the hydrogen bond between water and the C=O group of acetone is much weaker than that between water and the S=O group of DMSO. Due to the weakness of the hydrogen bond to the C=O group, the barrier for reorientation is low, thus making the hydroxyl group highly mobile. This interpretation is supported by the observations that these water molecules absorb at high frequencies and have a long vibrational lifetime of $T_1 \approx 13$ ps. Both observations indicate that the hydrogen bond donated by the O–D groups of these HDO molecules is very weak. It is seen in Figure 5.9B that the decay of the anisotropy $R_{WA}(t)$ significantly accelerates with increasing acetone concentration. The time constants of the reorientation are shown in Figure 5.10 and decrease from 6.1±0.2 ps at $X_{acet} = 0.3$ to 2.96±0.05 ps at $X_{acet} = 0.9$.

For both water-DMSO and water-acetone mixtures the anisotropy decay of the water molecules that are hydrogen bonded to the solute becomes faster with increasing solute concentration (Figures 5.8B and 5.9B). This acceleration is likely due to the fact that the water molecules that donate a hydrogen bond to the S=O group of DMSO/C=O group of acetone will become less coordinated with other water molecules when the solute concentration increases. With increasing X_{DMSO}, the fraction of 1:1 water-DMSO complexes will increase over the fraction of 2:1 water-DMSO complexes. As a result, the water molecule that is hydrogen bonded to the S=O group will no longer accept a hydrogen bond from another water molecule, which increases its orientational mobility. It has been observed that upon addition of acetone to water the number of 4-fold coordinated water molecules, which is the prevalent species in pure water, is gradually reduced, and that 3- and 2-fold coordinated water molecules become more prominent [91, 92]. Hence, at high acetone content, water molecules that donate a hydrogen bond to the C=O group with one hydroxyl group no longer donate a hydrogen bond to a water molecule with their other hydroxyl group, and no longer accept hydrogen bonds from other water molecules. As a result, the C=O bound water molecules become more mobile, leading to an acceleration of their reorientation.

The observed differences in vibrational relaxation and molecular reorientation dynamics of water molecules in water-DMSO and water-acetone mixtures likely find their origin in the different molecular geometries of the DMSO and acetone molecules. As mentioned in the introductory section, acetone adopts an essentially planar geometry, whereas the oxygen atom of a DMSO molecule lies outside the C-S-C plane. Additionally, the C-C and C=O bond lengths are considerably shorter than the the C-S and S=O bonds in DMSO, respectively, making acetone an overall more compact molecule. It is conceivable that the specific molecular geometry of DMSO allows a water molecule to donate a hydrogen bond to the oxygen atom of the S=O group of DMSO with little steric hindrance from the methyl groups. In contrast, the methyl groups of acetone

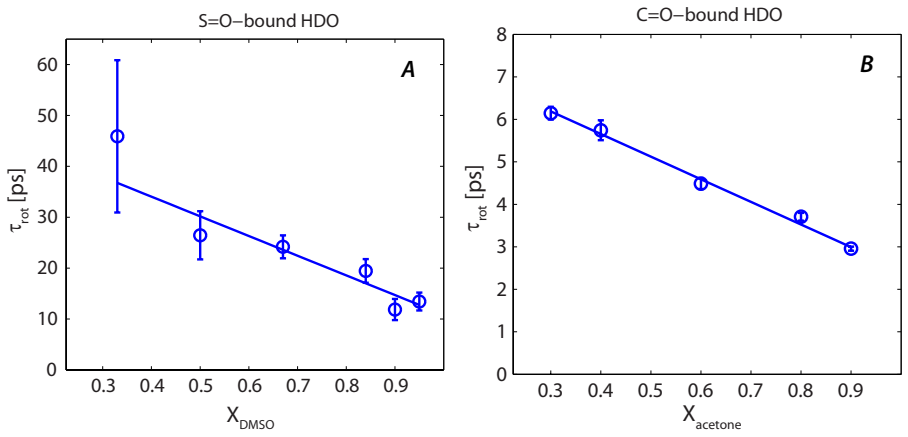

FIGURE 5.10. Time constants of the anisotropy decay of water molecules hydrogen bonded to the S=O group of DMSO as a function of X_{DMSO} (panel A), and the time constants of water molecules hydrogen bonded to the C=O group acetone as a function of X_{acet} (panel B). The time constants are obtained from a single-exponential fit of the data shown in Figures 5.8B and 5.9B.

might pose a significant steric barrier for the formation of hydrogen-bonds to the oxygen atom of the C=O group, due to the planar and overall more compact geometry of the acetone molecule.

5.4 CONCLUSIONS

We studied the vibrational energy relaxation and molecular reorientation dynamics of water molecules in water-DMSO and water-acetone mixtures with polarization-resolved femtosecond mid-infrared spectroscopy. For both water-DMSO and water-acetone mixtures we observe a slowing down of the vibrational relaxation dynamics of the water molecules with increasing solute fraction. For solute fractions $X_{sol} \geq 0.3$ the transient spectra show the presence of two components, corresponding to water molecules that are hydrogen bonded to other water molecules, and water molecules that are hydrogen bonded to C=O or S=O groups. The vibrational relaxation time constant T_1 of the C=O/S=O bound water molecules strongly increases with increasing solute fraction (Figure 5.4B), to 7.9 ps at $X_{DMSO} = 0.9$, and to 12.7 ps at $X_{acet} = 0.9$. This increase in vibrational lifetime can be explained from the decreased probability that the water molecule that is hydrogen bonded to S=O/C=O is involved in hydrogen bonds with other water molecules.

The water-DMSO and water-acetone mixtures show remarkable differences in the reorientation dynamics of the water molecules. At low solute fractions, we observe for both mixtures a fraction of water molecules that are strongly slowed down in their reorientation. We attribute this slow fraction to water

molecules that hydrate the hydrophobic methyl groups. The fraction of slow water is much smaller for water-acetone than for water-DMSO at the same concentration. For water-acetone the slow fraction does not exceed ∼20% of the total number of water molecules, and this plateau value is reached already at a solute concentration of $X_{acet} = 0.05$. This finding indicates that the acetone molecules form clusters already at low solute concentrations. With increasing solute fraction, the water-DMSO mixtures show a gradual transition from the effect of hydrophobic hydration to the effect of hydrogen bonding to the S=O group.

At high solute fractions, the water-bound water molecules in both water-acetone and water-DMSO mixtures show a very slow reorientation with a time constant $\gg$10 ps (Figures 5.9A and 5.8A). A difference between the two mixtures is that the amplitude of the water-bound water is much higher for water-acetone than for water-DMSO mixtures, which indicates that water forms nano-confined water clusters in water-acetone mixtures. The water-acetone mixtures also contain water molecules that are weakly hydrogen bonded to the C=O group. These water molecules show a relatively fast reorientation with a time constant that decreases from 6.1±0.2 ps at $X_{acet} = 0.3$ to 2.96±0.05 ps at $X_{acet} = 0.9$ (Figure 5.9B). For water-DMSO mixtures the water molecules forming hydrogen bonds to the S=O group show a much slower reorientation (Figure 5.8B) with a time constant that decreases from 46±14 ps at $X_{DMSO} = 0.33$ to 12 ± 2 ps at $X_{DMSO} = 0.95$. The large difference in reorientation time constant of the solute-bound water for DMSO and acetone is due to the fact that the hydrogen bond between water and the S=O group of DMSO is much stronger than the hydrogen bond between water and the C=O group of acetone.

Our observations support the notion of earlier studies that the structure of water-DMSO mixtures is largely determined by stable DMSO:water complexes for all mixture compositions, whereas the microscopic structure of water-acetone mixtures appears to be highly heterogeneous, showing nano-confined acetone clusters at low acetone concentrations and nano-confined water clusters at high acetone concentrations. This remarkable difference between water-DMSO and water-acetone mixtures is probably due to the difference in molecular structure between DMSO and acetone. The larger, bent DMSO molecule offers sufficient space for water molecules to form strong hydrogen bonds to the S=O group, while the more compact, planar acetone molecule does not provide sufficient space for a water molecule to form a strong hydrogen bond to the C=O group.

5.5 Appendix: Data analysis

In this section we present the kinetic model used to describe the isotropic transient absorption changes $\Delta\alpha_{iso}(\omega, t)$ and the decomposition of the polarization-resolved data $\Delta\alpha_{\parallel}(\omega, t)$ and $\Delta\alpha_{\perp}(\omega, t)$. When cast into matrix form, the set of ordinary differential equations associated with the vibrational relaxation model read as follows:

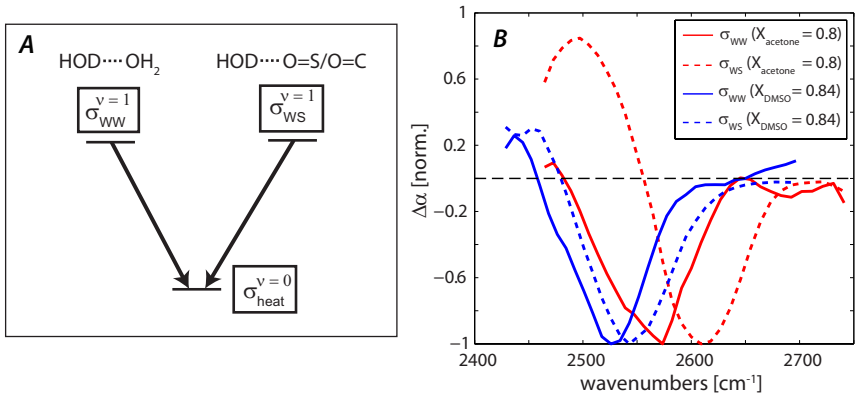

FIGURE 5.11. (A) Graphical representation of the model employed to describe the vibrational relaxation dynamics of the OD-stretch vibration of HDO molecules in water-DMSO and water-acetone mixtures. The excited states ($\nu = 1$) of water-bound (WW) and solute-bound (WS) HDO molecules decay to a common heated groundstate ($\nu = 0$). (B) Associated spectral signatures of the excited OD-stretch vibration of HDO molecules having their excited OD-group hydrogen bonded to other water molecules (lower frequency band) or the SO-/CO-moiety of DMSO/acetone. The spectra have been normalized to the maximum absolute value of the negative part of the spectra. The spectral separation between the two types of HDO-species is about 20 cm^{-1} for DMSO-water and 50 cm^{-1} for acetone-water.

$$\frac{d}{dt}\begin{pmatrix} N_{WW}(t) \\ N_{WS}(t) \\ N_{heat}(t) \end{pmatrix} = \begin{pmatrix} -1/T_{WW} & 0 & 0 \\ 0 & -1/T_{WS} & 0 \\ 1/T_{WW} & 1/T_{WS} & 0 \end{pmatrix} \cdot \begin{pmatrix} N_{WW}(t) \\ N_{WS}(t) \\ N_{heat}(t) \end{pmatrix} \tag{5.1}$$

Numerical integration of the above equations yields the time dependent population $N_i(t)$ of the three states included in the relaxation model. The best values for the vibrational lifetimes of water-bound HDO molecules T_{WW} and solute-bound HDO molecules T_{WS} are obtained by minimizing the target function

$$\chi^2(T_i) = \sum_k \left(\frac{\Delta\alpha_{iso}(\omega, t_k) - \sum_i^n N_i(t_k; T_i) \cdot \sigma_i(\omega)}{\epsilon_{iso}(\omega, t_k)} \right)^2 \tag{5.2}$$

The frequency-dependent, spectral signature of the i^{th} states $\sigma_i(\omega)$ are found by simultaneously finding the least-square solution to the following equation:

$$\frac{d}{d\sigma_i(\omega_j)} \sum_j \left(\frac{\Delta\alpha_{iso}(\omega_j, t) - \sum_i^n N_i(t; T_i) \cdot \sigma_i(\omega_j)}{\epsilon_{iso}(\omega_j, t)} \right)^2 = 0 \tag{5.3}$$

where i runs over all three states involved in the model of Figure 5.11A (n = 3).

Having obtained the spectral signatures of the excited states of water-bound and solute-bound HDO molecules, $\sigma_{WW}(\omega)$ and $\sigma_{WS}(\omega)$ are then used to disentangle the contribution from these distinct water species to the anisotropy decays in Figure 5.7(A,B). The anisotropy decays associated with each of the two water species individually are found by performing a decomposition of the polarization-resolved transient absorption changes $\Delta\alpha_{\parallel}(\omega,t)$ and $\Delta\alpha_{\perp}(\omega,t)$. To that end, we write the transient absorption changes obtained under parallel and perpendicular polarization of pump and probe pulses as

$$\Delta\alpha_{\parallel}(\omega,t) = \sum_{i=1}^{n}(1+2\cdot R_i(t))\cdot N_i(t)\cdot\sigma_i(\omega) = \sum_{i=1}^{n} N_{i,\parallel}(t)\cdot\sigma_i(\omega) \tag{5.4}$$

$$\Delta\alpha_{\perp}(\omega,t) = \sum_{i=1}^{n}(1-R_i(t))\cdot N_i(t)\cdot\sigma_i(\omega) = \sum_{i=1}^{n} N_{i,\perp}(t)\cdot\sigma_i(\omega) \tag{5.5}$$

where $R_i(t)$ denotes the anisotropy of a given species i of water molecules, which is assumed to have no frequency dependence, and the sum runs over all water species contributing to the transient absorption changes. Since the heated ground state ($i = 3$) represents a thermal difference spectrum, it is assumed to be isotropic and not to contribute to the anisotropy decay. Therefore, the signal contribution of the heated ground state is subtracted and the decomposition is performed with the two excited states only ($n = 2$ in Eq. (5.4) and Eq. (5.5)). The decomposition of the polarization resolved data sets $\Delta\alpha_{\parallel}(\omega,t)$ and $\Delta\alpha_{\perp}(\omega,t)$ with the previously obtained $\sigma_{WW}(\omega)$, $\sigma_{WS}(\omega)$ is based on finding the least square solution to the following equation:

$$\frac{d}{dN_{i,\parallel}(t_k)}\sum_{k}\left(\frac{\Delta\alpha_{\parallel}(\omega,t_k)-\sum_i N_{i,\parallel}(t_k)\cdot\sigma_i(\omega)}{\epsilon_{\parallel}(\omega,t_k)}\right)^2 = 0 \tag{5.6}$$

The same procedure is performed for $\Delta\alpha_{\perp}$. Having obtained $N_{i,\parallel}(t)$ and $N_{i,\perp}(t)$, we can extract the anisotropy decay that reflects purely the reorientation dynamics of the i^{th} water species:

$$R_i(t) = \frac{N_{i,\parallel}(t)-N_{i,\perp}(t)}{N_{i,\parallel}(t)+2\cdot N_{i,\perp}(t)} \tag{5.7}$$

6 Vibrational energy transfer in an antifreeze protein

We performed time- and polarization-resolved pump-probe and two-dimensional infrared (2D-IR) experiments to study the dynamics of the amide I vibration of a 7 kDa type III antifreeze protein. In the pump-probe experiments, we used femtosecond mid-infrared pulses to investigate the vibrational relaxation dynamics of the amide mode. The transient spectra show the presence of two spectral components that decay with different lifetimes, indicative of the presence of two distinct amide subbands. The 2D-IR experiments reveal the coupling between the two bands in the form of cross-peaks. Based on previous work by Demirdöven *et al.* (*J. Am. Chem. Soc.* 126 (25), 2004), we assign the observed bands to the two infrared-active modes $\alpha(-)$ and $\alpha(+)$ found in protein β-sheets. The amplitudes of the cross-peak were found to increase with delay time, indicating that the cross-peaks originate from population transfer between the coupled amide oscillators. The time constant of the energy transfer was found to be 6-7 ps.

6.1 Introduction

Among the various normal modes of the protein backbone, the amide I band forms a particularly sensitive marker for secondary structural elements. The vibration consists primarily of the displacement of the carbonyl group of the amide moiety with additional contributions from CN-streching and NH-bending [101]. The latter contribution is responsible for a slight shift of the amide I resonance frequency upon isotopic exchange from hydrogen to deuterium (denoted as amide I'). Amide oscillators are known to be coupled by electrostatic interactions, leading to the formation of vibrational excitons [102, 103]. Depending on the degree of structural disorder, these excitons can be partially delocalized over several residues of the peptide chain. Hochstrasser and coworkers were the first to investigate the signature of the excitonic states of the amide I' band with nonlinear infrared spectroscopy [30]. They found that vibrational excitations are delocalized between coupled sets of amide oscillators over a length of ~ 8 Å.

Over the past years, twodimensional infrared (2D-IR)-spectroscopy has become an extremely valuable tool for the study of the amide I' vibration of proteins and peptides, owing to its sensitivity to fast dynamics occuring on femto- to picosecond timescales. Most 2D-IR-studies have focussed on the analysis of lineshapes and coupling patterns, and many insightful observations about the structure and the conformational dynamics have been obtained [15, 16, 104–109]. In combination with theoretical modeling and residue-specific isotope labeling, mechanistic models and structure-function relationships have been devised for systems as complex as the M2 proton channel [104,108], membrane-associated peptides [16], and dimers of transmembrane helices [109] based on 2D-IR-spectra. The aforementioned studies have mainly been performed for a fixed timing of the pulses in the 2D-IR-pulse sequence, and relatively few studies have focussed on the dynamics of the amide mode [3, 110–112]. In a recent study by Middleton *et al.* it was found that the vibrational lifetime of the amide I' mode is correlated with the degree of structural disorder [110]. Hamm and coworkers have observed the breaking and reformation of hydrogen bonds between the amide groups of *N*-methylacetamide and the hydroxyl groups of methanol [111]. The same group has also studied the energy transfer dynamics between the amide oscillators of small peptides embedded in different environments [3, 112].
In this paper, we report on a study of the response of the amide I' vibration of a 67-residue type III antifreeze protein (AFPIII) from ocean pout (*macrozoarces americanus*) with linear- and nonlinear infrared spectroscopy. Antifreeze proteins are a class of proteins that are found in the body fluids of organisms that need to survive at sub-zero temperatures and are known to act as cryoprotectants by lowering the freezing point of aqueous solution with respect to the melting point [113]. We have applied polarization-resolved infrared pump-probe experiments using femtosecond pulses to the study of vibrational relaxation dynamics, and in addition performed delay-dependent 2D-IR-experiments using narrowband excitation pulses to obtain insight into the energy transfer dynamics of the amide I' band of AFPIII. The results strongly suggest the presence of intramolecular β-sheets in agreement with the X-ray crystal structure, demonstrating the sensitivity of 2D-IR for flexible structural elements invisible by commonly employed spectroscopic tools to probe protein structure in solution such as circular dichroism spectroscopy [114–116].

6.2 Experimental section

Nonlinear infrared spectroscopy

We use femtosecond mid-infrared spectroscopy to measure the vibrational relaxation dynamics of the amide I' vibration of 1.4 mM solutions of AFPIII dissolved in a D_2O-buffer (containing 150 mM NaCl, 20 mM tris(hydroxymethyl) aminomethane). D_2O is used instead of H_2O to avoid the absorption of the mid-infrared pulses by the bending mode of H_2O. The mid-infrared femtosecond pulses required for this study are generated by a series of nonlinear fre-

quency conversion processes that are pumped with the pulses of a commercial Ti:sapphire regenerative amplifier (Coherent Legend Elite Duo) as described in Chapter 3. To avoid absorption of the infrared pulses by ambient air, the setup is purged with nitrogen during the experiment. The pulse length at the sample position was determined by two-photon-absorption in an InAs-wafer and inferred to be ∼100 fs. We use the mid-infrared pulses in a polarization resolved pump-probe experiment as described in Section 3.1.

Relaxation of the initially excited amide I' oscillators as well as direct absorption of the pump light by the high-frequency shoulder of the D_2O-band centered at 1500 cm^{-1}lead to the rise of a thermal signal in the pump-probe spectra. In order to describe the kinetics of this process in a model-free approach, we have measured the pump-induced shift of the OD-stretch band using a second, independently tunable optical paremtric amplifier in combination with a $AgGaS_2$-based difference frequency generation scheme, generating probe pulses in resonance with the shoulder of the OD-stretch absorption band of the solvent ($\sim$ 2200 cm^{-1}). The pump pulse remains tuned to the amide I' vibration. The kinetics obtained from this experiment are used to subtract the time-dependent thermal signal from the pump-probe data set prior to further analysis. In this procedure, we have implicitly assumed that the time-dependence of thermal effects is identical for all modes in the sample.
In addition, we perform two-dimensional infrared (2D-IR) experiments as described in Section 3.2. During all experiments, the samples were held between two CaF_2 windows separated by Teflon spacers with a thickness in the range between 25 and 50 μm. The temperature of the sample was set by a thermoelectric module and actively stabilized over the course of the experiment by a programmable temperature controller (PTC 10, Stanford Research Systems), driven by in-house designed software. In the experiments below 8°C, the samples were rotated during the measurement to ensure that each laser shot probes a fresh portion of the sample so as to avoid steady-state heating in the focus.

6.3 Experimental results and interpretation

6.3.1 Isotropic transient spectra

Figure 6.1 shows the transient absorption changes of the amide I' band of AFPIII. The spectrally broad excitation pulses used in this experiment have sufficient bandwidth to cover the entire amide I' absorption band. The spectra show a negative response that peaks at 1640 cm^{-1}, originating from the bleaching of the ground state ($\nu = 0$) and stimulated emission from the first excited state ($\nu = 1$) of the amide I' mode. The positive feature in the transient spectrum observed at frequencies < 1620 cm^{-1} originates from excited state absorption ($\nu = 1 \rightarrow 2$). The signal at delay times > 20 ps has a flat and featureless shape (not shown here) and originates from the shift of the solvent background due to heating. The contribution from this signal has been subtracted from the data in Figure 6.1 as outlined in the experimental section.

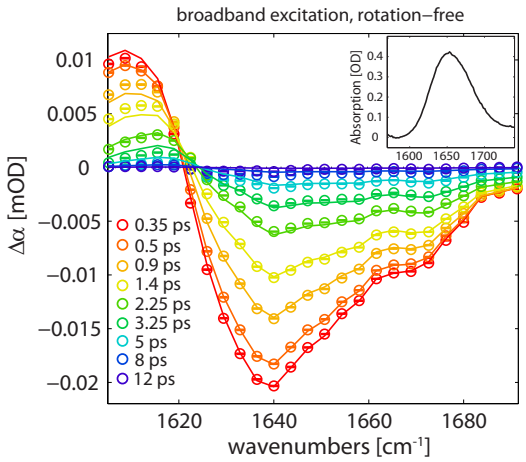

FIGURE 6.1. 1D-pump-probe data of AFPIII obtained under broadband excitation. The sample thickness used in the experiment was 50 micron. The open circles represent the data points after subtraction of the time-dependent rise of the thermal signal. The solid lines represent a fit to the model outlined in the text. The inset shows the linear absorption spectrum of the sample after subtraction of the solvent background.

It is worth noting the difference in spectral shapes between the linear absorption spectrum of AFPIII shown in the inset of Figure 6.1 and the nonlinear pump-probe spectrum. In the FTIR-spectrum, the amide I' band appears as a nearly Gaussian-shaped absorption line without shoulders or sidelobes. The slight asymmetry might in fact be caused by imperfect subtraction of the solvent background. In contrast, the bleaching signal of the transient spectra in Figure 6.1 exhibits a clear additional shoulder around 1670 cm^{-1}, which is not observed in the linear spectrum. The difference in intensity distribution can be understood from the dependence of the signal amplitude on the absorption cross-section, which is linear in the case of the FTIR-spectrum, but scales quadratically with the absorption cross-section in the pump-probe spectrum. In Figure 6.2 we plot the isotropic transient absorption changes obtained from the broadband excitation experiments at four different detection frequencies. To avoid any unwanted contributions arising from coherent coupling between pump- and probe pulses during the time-overlap of the pulses [31, 32] or perturbed free induction decay effects [33, 34] (see Section 2.4.2), we analyze the population relaxation only after a pump-probe delay of 300 fs. The data have been normalized to the maximum signal to facilitate a comparison of the dynamics. The population decay of the amide I' vibration has a pronounced frequency dependence, which points at the presence of more than one subensemble of amide oscillators within the absorption band. We find the decay to slow down with increasing frequency, which is consistent with the observation of a blue-shift of the transient spectrum in Figure 6.1 with increasing delay time. We describe the data set $\Delta\alpha(\omega, t)$ with a model that contains two excited

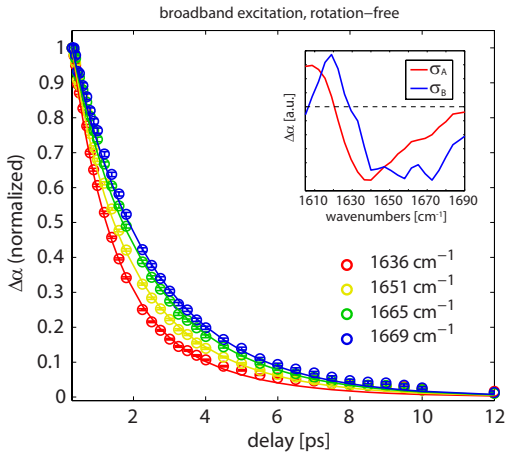

FIGURE 6.2. Transient absorption change obtained under broadband excitation conditions at different detection frequencies. The data have been normalized to the signal at 300 fs. Open circles represent the data points obtained after subtraction of the thermal signal as described in the text. The solid lines represent the fit of the kinetic model outlined in the text, and the inset shows the spectral signatures σ_A and σ_B of the excited states obtained with the fit.

states decaying with different lifetimes to a common ground state. The spectral signatures of the excited states that we extract from the fit are depicted in the inset of Figure 6.2. We find the lower-frequency component of the spectrum to decay with a lifetime of T_1^a of 1.09 ps, whereas the high frequency component exhibits a longer lifetime T_1^b of 3.21 ps. The details of the fitting procedure are described in section 6.3.2.

More detailed information on the structural origin of the two components can be obtained from a two-dimensional infrared spectroscopic (2D-IR) experiment, in which the coupling between different sets of amide modes reveals itself in the form of crosspeaks. As outlined in Section 3.2, we have implemented 2D-IR-spectroscopy in the form of a hole-burning experiment, in which we make use of tunable, spectrally narrow excitation pulses in combination with broadband probing pulses [3, 30, 37, 117]. In Figure 6.3 we show 2D-IR-spectra obtained at delays of 1 ps (Figure 6.3A) and 2 ps (Figure 6.3B) measured with a probe pulse with a polarization perpendicular to that of the pump. The negative bleaching/stimulated emission signal shows a pronounced elongation along the diagonal in both spectra. This correlation between excitation and probing frequency reflects inhomogeneous broadening, which is static on the timescales shown here (1-2 ps). In addition, we observe a ridge in the negative signal above the diagonal at $\omega_{probe} = 1670$ cm^{-1}, which becomes more pronounced with increasing delay time (Figure 6.3B).

To visualize the time-evolution of the spectrum, we plot in Figures 6.3C and 6.3D cuts through the 2D-IR-spectrum at excitation frequencies of

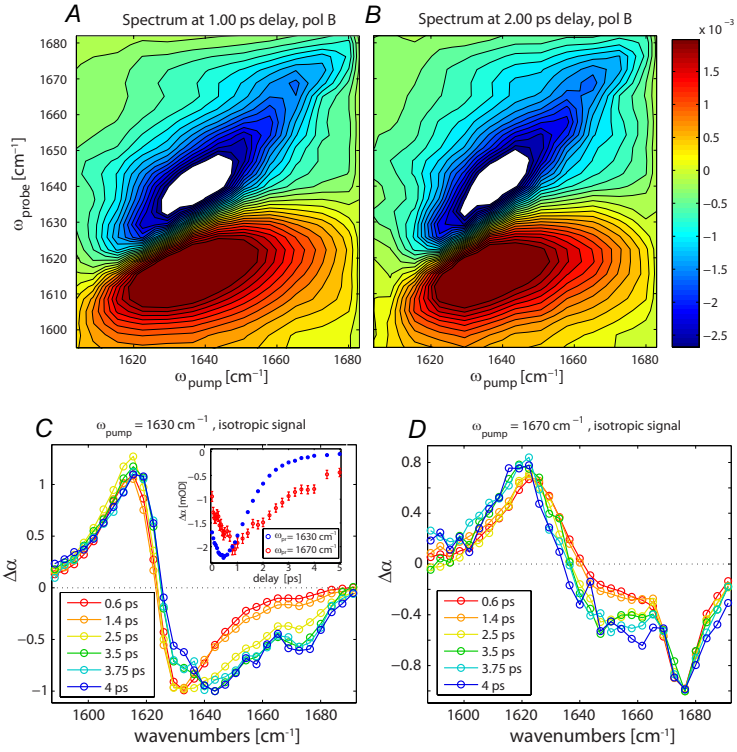

FIGURE 6.3. 2D-IR-spectra of the amide I' region of AFPIII, obtained at a delay time of (A) 1 ps and (B) 2 ps measured with perpendicular polarization of the pump- and probe pulses. The spectra have been generated from a series of narrowband excitation experiments with 12 different pump positions. Negative absorption signals are depicted as blue, positive absorption signals in red. The contours are equally spaced between +70% and -70% of the maximum bleaching signal. (C,D) Cuts through the isotropic part of the 2D-IR-spectrum for excitation frequencies $\omega_{pump} = 1630$ cm^{-1} (C) and $\omega_{pump} = 1670$ cm^{-1} (D), normalized to the minimum of bleaching signal. The inset in (C) shows the delay traces of the diagonal peak ($\omega_{probe} = 1630$ cm^{-1}, blue symbols) and the off-diagonal signal ($\omega_{probe} = 1670$ cm^{-1}, red symbols) for $\omega_{pump} = 1630$ cm^{-1}. The off-diagonal signal is magnified by a factor of 9 for clarity.

$\omega_{pump} = 1630$ cm^{-1} and $\omega_{pump} = 1670$ cm^{-1} at delay times ranging from 0.6 ps to 4 ps, normalized to the minimum of the bleaching signal. The thermal level has been subtracted in the same way as described above for the experiments under broadband excitation. Upon excitation of the amide oscillators at either frequency positions, a delayed rise of a bleaching signal is seen in the off-diagonal region, pointing at the presence of rising crosspeaks in these regions of the 2D-IR-spectrum. The inset in Figure 6.3C shows the delay traces at $\omega_{probe} = 1630$ cm^{-1} (diagonal signal) and $\omega_{probe} = 1670$ cm^{-1} (off-diagonal signal). The plot clearly shows that the off-diagonal signal peaks at a later

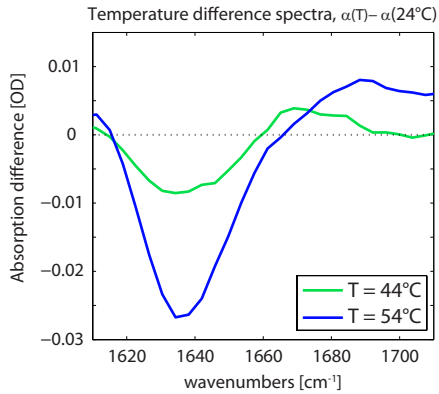

FIGURE 6.4. FTIR difference spectra of the amide I' band of AFPIII for different temperatures. The spectra have been obtained by first subtracting a spectrum of the solvent measured at the same temperature from the raw absorption spectrum of the sample, and subsequently taking the difference spectra between the background-corrected absorption spectra of AFPIII. The sample thickness in this experiment was 50 μm.

delay time than the diagonal signal, and that both signals decay with different lifetimes. The signal at ω_{probe} = 1670 cm^{-1} must therefore constitute a cross-peak that likely results from the exchange of population with the directly excited amide oscillators. In Figure 6.3D, the rise of a bleaching signal in the region ω_{probe}= 1630 - 1660 cm^{-1} is observed. The bleaching signal is partially compensated by the positive-valued induced 1→2 absorption. The rise of this off-diagonal bleaching signal results from population transfer from the directly excited mode at 1670 cm^{-1} to amide oscillators at lower frequencies.

To exclude the possibility that the delayed rise of the off-diagonal signals in Figure 6.3(C,D) originates from a local, transient heating effect resulting from thermalization of the vibrational relaxation, we have studied the influence of a temperature increase on the amide I' band by measuring solvent-corrected temperature-difference absorption spectra. From these difference spectra shown in Figure 6.4 it is apparent that an increase in temperature leads to a blueshift of the amide I' band, which is accompanied by a decrease in absorption cross-section. In the transient absorption spectrum, a temperature increase would thus lead to a bleach in the frequency region from 1620 cm^{-1} to 1660 cm^{-1} and an induced absorption in the region >1660 cm^{-1}. This is in contrast to the observations of Figure 6.3C, where the delayed rise of a *bleaching* signal in the frequency region of ω_{probe} >1660 cm^{-1} is clearly seen. The bleaching nature of this signal excludes the possibility that it originates from a local increase in temperature and strongly supports our assignment of the off-diagonal dynamics to the population transfer from directly excited amide modes at 1630 cm^{-1} to amide oscillators at higher frequencies.

Recently, a systematic study of the 2D-IR-spectroscopic signatures of differ-

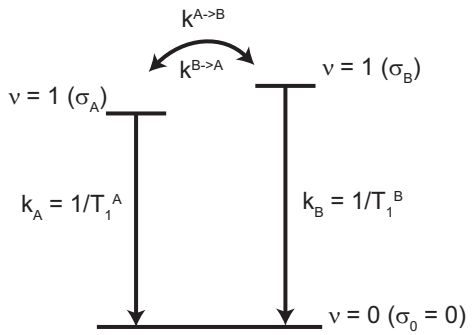

FIGURE 6.5. Rate model employed to fit the isotropic pump-probe data set $\Delta\alpha_{iso}(\omega, t)$. The rates of population transfer between the two excited states are constrained by the detailed balance condition $k_{A\to B}/k_{B\to A} = e^{-\Delta E/kT}$. The explicit expression for the rate equations are given in the appendix of this chapter.

ent structural elements of proteins and peptides has been performed by the Tokmakoff-group [105]. In this study, it was shown that the two infrared-active vibrational modes associated with antiparallel β-sheet elements, denoted as $\alpha(+)$ and $\alpha(-)$, are strongly coupled and give rise to a distinct cross-peak in the 2D-IR-spectrum. Based on this work, we assign the two components that we observe at $\omega \approx 1630$ cm^{-1} and $\omega \approx 1670$ cm^{-1} in the 2D-IR-spectra of AFPIII to the $\alpha(-)$ - and $\alpha(+)$ - modes of β-sheets, respectively. The $\alpha(+)$ and $\alpha(-)$ are collective modes that consist primarily of the in-phase movement of amide I'-oscillators on adjacent strands, leading to a delocalized mode with a transition dipole moment perpendicular to the direction of the β-strands ($\alpha(-)$), and the in-phase movement of neighboring oscillators within one strand ($\alpha(+)$), forming a mode with a transition dipole moment approximately parallel to the strands. The character of these modes is illustrated in Figure 6.9B.

6.3.2 KINETIC MODELING OF THE EXCHANGE

With the findings in the previous paragraph in mind, we return to the kinetic analysis of the broadband pump-probe data. To account for the energy transfer within the amide I' absorption band that was observed in the 2D-IR-spectra, we employ a kinetic model that is outlined schematically in Figure 6.5 to fit the isotropic pump-probe data set $\Delta\alpha_{iso}(\omega, t)$. We assume that the data set can be described by the product of the time-dependent populations $N_i(t)$ of the states involved in the relaxation scheme and their associated spectral signatures σ_i:

$$\Delta\alpha_{iso}(\omega, t) = N_A(t) \cdot \sigma_A + N_B(t) \cdot \sigma_B + N_0(t) \cdot \sigma_0 \tag{6.1}$$

The subscripts A, B and 0 denote the two excited states included in the model of Figure 6.5 and the groundstate, respectively. It should be noted that the spectra σ_i represent difference spectra with the absorption spectrum of

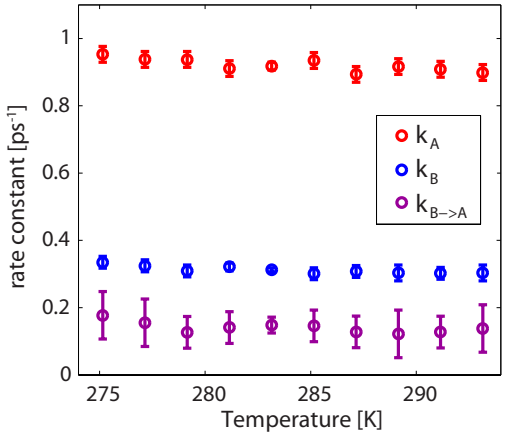

FIGURE 6.6. Rate constants obtained from a fit of the isotropic data set $\Delta\alpha_{iso}(\omega, t)$ to the model of Figure 6.5 for different sample temperatures between 2 and 20°C. Both the vibrational relaxation rates $k_A = 1/T_1^A$ and $k_B = 1/T_1^B$ of the two amide I' subbands as well as the exchange rate $k_{B\to A}$ show only minor variation with temperature.

the ground state. At later delay times, the transient spectrum will be formed by a thermal difference spectrum representing the change in absorption of the groundstate induced by the thermalization of the vibrational excitation. However, this contribution is already eliminated by the subtraction of the rising thermal difference spectrum from the data set as outlined in the experimental section. From a least-square fit, we find a rate of energy transfer from the higher-lying state to the lower-energy state of $k_{B\to A}$= $(7.1 \pm 0.2$ ps$)^{-1}$ and rates of relaxation to the groundstate of $k_A = 1/T_1^A = (1.09 \pm 0.01$ ps$)^{-1}$ and $k_B = 1/T_1^B = (3.21 \pm 0.07$ ps$)^{-1}$. Figure 6.6 shows the temperature dependence of the rate constants obtained from the least-square fit, ranging from 2 to 20°C. We find that the exchange rate $k_{B\to A}$ as well as the vibrational relaxation rates k_A and k_B are essentially temperature independent over the investigated range. The associated spectral signatures of the excited states σ_A and σ_B that we extract from the fit are depicted in the inset of Figure 6.2.

We employ the rate constants outlined above to perform a model calculation of the time-evolution of the 2D-IR-spectrum. The results of these calculations are presented in Figure 6.7 for two different excitation frequencies of $\omega_{pump} = 1630$ cm^{-1} and $\omega_{pump} = 1670$ cm^{-1}. The calculated spectra are to be compared with the experimental data in Figure 6.3(C,D). The calculations are based on fitting the isotropic transient spectra at an early delay time ($\tau = 0.6$ ps) obtained for $\omega_{pump} = 1630$ cm^{-1} and $\omega_{pump} = 1670$ cm^{-1} with a sum of Lorentzians and subsequently calculating the time evolution of these two components with the kinetic model and the rate constants outlined in the previous paragraphs. The peak positions and the linewidths of the Lorentzians are presented in Table I. The spectra obtained for $\omega_{pump} = 1630$ cm^{-1} are in

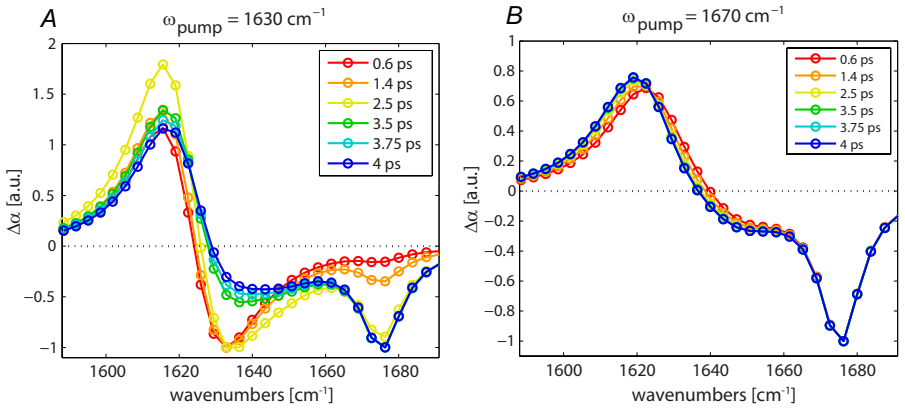

FIGURE 6.7. Calculated delay-time dependence of cuts through the 2D-IR-spectrum for excitation frequencies of (A) $\omega_{pump} = 1630$ cm^{-1}and (B) $\omega_{pump} = 1670$ cm^{-1}. The results are directly to be compared with the experimental data in Figure 6.3(C,D).

excellent agreement with the transient spectra in Figure 6.3C. The delayed rise of the bleaching signal in the range of $\omega_{probe} = 1640$ - 1680 cm^{-1} as well as the small blueshift of the induced absorption signal with increasing delay time are well reproduced. It should be noted that also the initial increase and subsequent decay of the induced absorption signal with a maximum at intermediate delay times ($\tau = 2.5$ ps, yellow curves in Figures 6.3C and 6.7A) is well reproduced by our model. The agreement of the calculations for $\omega_{pump} = 1670$ cm^{-1} in Figure 6.7B with the experimental data of Figure 6.3D is less good, but the main features and trends of the time-dependent transient spectra can be reproduced. The transient redshift of the induced absorption and the rise of the bleaching signal in the region of $\omega_{probe} = 1640$ - 1665 cm^{-1} is accounted for by the calculations, albeit that the latter feature is less pronounced in the calculations than in the experimental data. The overall less good agreement of the model calculations with the experimental data for $\omega_{pump} = 1670$ cm^{-1} than for

ω_{pump}	ν_1	fwhm	sign	ν_2	fwhm	sign	ν_3	fwhm	sign
1630	1618.5	26.3	pos.	1628.0	28.1	neg.			
1670	1624.5	26.0	pos.	1647.6	32.1	neg.	1675.3	13.4	neg.

TABLE I. Parameters used for the calculation of delay-time dependence of the narrowband excitation spectra (cuts of the 2D-IR-spectrum along ω_{probe} for $\omega_{pump} = 1630$ cm^{-1} and 1670 cm^{-1}) shown in Figure 6.7. The parameters have been obtained from a fit of a sum of Lorentzian lineshape functions to the transient spectra in Figure 6.3(C,D) at earliest delay times (0.6 ps). ν_i and fwhm$_i$ denote the center frequency and the full-width at half maximum of the Lorentzian functions, respectively, and are given in cm^{-1}. The sign indicates whether the signal originates from a bleach (negative) or an induced absorption (positive).

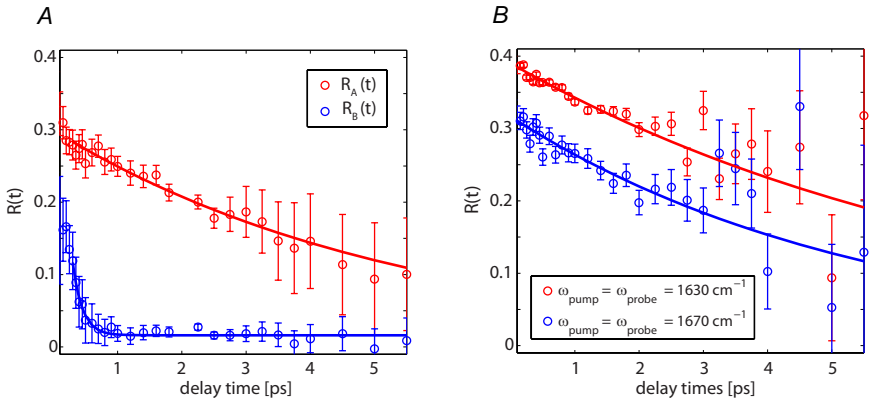

FIGURE 6.8. (A) Anisotropy decays obtained from a decomposition of the polarization-resolved broadband pump-probe data sets $\Delta\alpha_{\parallel}(\omega,t)$ and $\Delta\alpha_{\perp}(\omega,t)$. (B) Anisotropy decays of the diagonal signal of the 2D-IR-spectrum for narrowband excitation $\omega_{pump} = 1630$ cm^{-1} and $\omega_{pump} = 1670$ cm^{-1}. The solid lines are exponential fits to the data.

$\omega_{pump} = 1630$ cm^{-1} might be due to the presence of additional spectral equilibration after narrowband excitation at 1670 cm^{-1}, which is not included in the present model. The narrower width of the bleaching signal immediately after excitation at 1670 cm^{-1} ($\tau = 0.6$ ps in Figure 6.3D) when compared to the initial bleach after excitation at 1630 cm^{-1} ($\tau = 0.6$ ps in Figure 6.3C) suggests that a slow spectral diffusion process affects the time-evolution of the transient spectra stronger in the case of excitation of the $\alpha(+)$-band at 1670 cm^{-1}, for which a narrow spectral hole of $\sim$10 cm^{-1} is burned, than in the case of pumping at 1630 cm^{-1}, where the initial bleach has a width of approximately 20 cm^{-1}.

6.3.3 ANISOTROPY DYNAMICS OF THE PUMP-PROBE EXPERIMENTS

The spectral signatures can be used together with the polarization-resolved data sets $\Delta\alpha_{\parallel}(\omega,t)$ and $\Delta\alpha_{\perp}(\omega,t)$ to construct the time-dependent anisotropy decays for both individual bands by using the approach described in the appendix of Chapter 5 (Eqs. (5.4)-(5.7)). The anisotropy curves obtained in this way are shown in Figure 6.8. We find that the anisotropy curve of the high-frequency band R_B(t) exhibits a large drop within the first 500 fs, leading to an almost complete decay. In contrast, the anisotropy of the low-frequency band, $R_A(t)$, shows a much slower decay on a time-scale of several picoseconds. We find that the decay of $R_A(t)$ can be well described by a single exponential with a decay rate of $1/\tau = (5.5$ ps$)^{-1}$.
In Figure 6.8B we show the anisotropy decays of the diagonal signals of the 2D-IR-spectrum. Interestingly, neither of the anisotropy curves in Figure 6.8B shows a similar rapid decay as observed for the $R_B(t)$-curve in Figure 6.8A.

Instead, both curves decay on a timescale comparable to $R_A(t)$ in Figure 6.8A. The different dynamics of the anisotropy decays in broadband pump-probe experiments compared to 2D-IR-experiments has its origin in the exchange of population between the two modes considered in our model. In the 2D-IR-experiment, the spectrally selective excitation pulse creates population in only one of the excited states. The excited state population can either decay to the ground state (T_1-relaxation) or transfer population to the other mode (cross-relaxation). Both processes lead to a decay of the isotropic pump-probe signal of the initially excited mode, i.e. of the diagonal signal in the isotropic 2D-IR-spectrum, while at the same time leaving the *anisotropy* of the signal unaffected. The anisotropy of each probed amide I' vibration can only decay due to molecular reorientation, or if another excited vibration with a different orientation, i.e. the other amide I' mode, changes its character (frequency) to that of the probed vibration.
The situation outlined above for the narrowband-excitation 2D-IR experiments contrasts the situation encountered in the pump-probe experiments with broadband excitation pulses. The spectrally broad pump-pulse generates excited state population in *both* modes, with the ratio of population in the $\nu = 1$-states being determined by the cross-sections of the two modes. The excitation of both modes enables the exchange of population between the two excited, differently oriented amide I' modes, thereby opening up an efficient loss-channel for the anisotropy. Considering that the cross-section of the lower-frequency band σ_A is higher than that of σ_B, mode A will be more strongly excited than mode B. As a result, the exchange will have a much stronger effect on the anisotropy of mode B that on the anisotropy of mode A, thus likely causing the observed fast decay in the anisotropy curve R_B shown in Figure 6.8A.

6.4 DISCUSSION

The splitting of the amide I' band and the accompanying formation of cross-peaks in the 2D-IR-spectrum is highly characteristic for antiparallel β-sheets [105, 118]. Structurally disordered segments do not feature this distinctive lineshape behaviour. Therefore the two amide I' modes as observed in our experiment appear to be dominated by β-sheet character, thus supporting an assignment to $\alpha(-)$- and $\alpha(+)$-modes. The prevalence of β-sheet character in the amide I' response is in agreement with the crystal structure of AFPIII that has been determined by Anston *et al.* [115] and is shown in Figure 6.9A. Nevertheless, in view of the structure of AFPIII proteins it is likely that one or even both of the spectral components obtained in the analysis (inset of Figure 6.2) contains a contribution from random coil elements of the protein [114–116]. It should be noted that, in case the amide oscillators in random coil or α-helical segments exhibit vibrational lifetimes very similar to either the α(-) or $\alpha(+)$ mode, an unambiguous distinction *solely* based on a kinetic analysis is not possible. The high-frequency band (blue curve) shown in the inset of Figure 6.2 has a non-negligible amplitude around 1650 cm^{-1}, which likely originates from the

amide I' vibrations of random coil/helical elements, that show a similar lifetime as the $\alpha(+)$ mode.

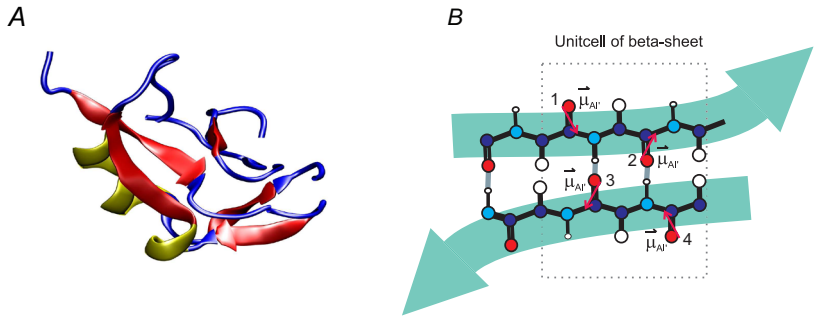

FIGURE 6.9. (A) Crystal structure of type III AFP determined by Antson *et al.* [115] (pdb-code 1HG7). The strands of the β-sheets are represented in red, random coil elements in blue and helices in yellow. (B) Schematic representation of the infrared-active collective vibrations of antiparallel β-sheets according to Ref. [105]. Red arrows indicate the direction of the transition dipole moment of the amide I' mode of the individual peptide moieties 1 to 4. Both the $\alpha(-)$ and $\alpha(+)$ modes correspond to the out-of-phase stretching movement of the (1,4) and (2,3) pairs of amide oscillators on adjacent β-strands. The $\alpha(+)$-mode is associated with the in-phase movement of neighboring oscillators (pairs (1,3) and (2,4), respectively), whereas the $\alpha(-)$-mode corresponds to the out-of-phase movement of these oscillators.

In a simulation study of the 11-residue β-hairpin peptide *trpzip2*, Jansen and Knoester found population transfer between the $\alpha(-)$- and $\alpha(+)$- modes of β-sheets [119], but in this study the transfer rate was found to be approximately a factor of 10 larger than in the present study. The value of $(7.1\ \text{ps})^{-1}$ we find for the exchange rate of AFPIII is in good agreement with the cross-relaxation rates of $(5.26\ \text{ps})^{-1}$ measured by Woutersen *et al.* for tri-alanine [3]. In this latter study, the energy transfer dynamics were found to be completely determined by a sub-picosecond component in the correlation function of the fluctuating coupling between the amide oscillators. It is thus conceivable that the cross-relaxation between the $\alpha(-)$ and $\alpha(+)$-modes in AFPIII results from fast conformational fluctuations of the β-sheets of the protein. We measured the temperature dependence of the exchange rate over an interval from 2°C to 20°C, and found the exchange rate to vary only within the experimental uncertainty. This observation implies that the protein backbone remains relatively flexible over the investigated temperature range, even at temperatures approaching the freezing point of the solvent. This notion of highly flexible β-sheets is supported by the absence of detectable secondary structure in circular dichroism spectroscopy, while the X-ray diffraction structure of flash-frozen crystals with strongly suppressed dynamics reveals two β-sheets, a β-bridge, and two 3_{10}-helices [114–116]

In the case of broadband pumping, the anisotropy of $\alpha(+)$ shows a very fast decay that we can explain from the energy transfer between the $\alpha(-)$ and $\alpha(+)$

modes. Similar subpicosecond decays of the anisotropy have been observed before in infrared pump-probe experiments on the peptides *apamin*, *scyllatoxin* and *bovine pancreatic inhibitor* [30]. In line with our interpretation, these fast decays have been assigned to energy transfer within the amide I' vibrational manifold [30]. In the case of narrowband excitation, the anisotropy dynamics of both the $\alpha(-)$ and the $\alpha(+)$ mode are quite slow because the transfer between these modes will negligibly contribute to the anisotropy decay. In the experiments of Figure 6.8B only either of the two modes gets excited, and to get an effect of energy transfer on the anisotropy the energy should not only be transferred to the unexcited mode but also back to the excited mode, which makes this contribution rather unimportant. The observed slow decay of the anisotropy can be ascribed to either molecular reorientation or to energy transfer between different modes $\alpha(-)$ or between different modes $\alpha(+)$. The first option can be ruled out in the present case considering the size of the protein and the relatively fixed orientation of the amide moiety in the peptide chain. The second option of energy transfer between different modes $\alpha(-)/\alpha(+)$ implies that there is a coupling between the modes leading to an excitonic manifold of delocalized $\alpha(-)$ states and an excitonic manifold of delocalized $\alpha(+)$ states. When either of the bands is excited, a set of excitonic states is populated that initially interferes constructively to an excited state for which the transition dipole moment is well aligned with the polarization of the pump pulse. The subsequent quantum interference and dephasing of the excitonic states will lead to a change of the orientation of the transition dipole moment and thus to a decay of the anisotropy. This type of quantum interference and dephasing has been discussed in Ref. [30] for the amide I modes of several other peptides, and also for the case of coupled electronic states in Ref. [33]. The interpretation of the anisotropy decay of Figure 6.8B in terms of dephasing of an excitonic manifold of $\alpha(-)/\alpha(+)$ states is further corroborated by inspection of the width of the spectral hole that is burned into the amide I' absorption band upon excitation with a narrowband pump pulse. A fit of a Lorentzian lineshape function to the spectral hole obtained upon excitation of the $\alpha(+)$-mode at 1670 cm^{-1} in Figure 6.3D yields a full width at half maximum (fwhm) of approximately 12 cm^{-1}. This value is comparable to the bandwidth of the excitation pulse ($\Delta\nu_{fwhm} \approx 10$ cm^{-1}), which implies that the dephasing time of the a(+)-states must occur on a timescale that is significantly *longer* than the duration of the excitation pulses. Previous work showed that the dephasing of excitonic amide I modes typically takes place with a time constant $T_2 \approx 1$ ps [16, 30, 120], thus making it indeed plausible that excitonic dephasing can lead to a decay of the anisotropy on a time scale of picoseconds, as observed in Figure 6.8B.

6.5 CONCLUSIONS

We have shown that the vibrational relaxation of the amide I' band of a type III antifreeze protein shows a pronounced frequency dependence, originating from the presence of two distinct amide I' bands with lifetimes of 1.09 ± 0.01 ps

and 3.21 ± 0.02 ps. From a twodimensional spectroscopic experiment, it was found that the two bands are coupled and exchange population with a rate of $k_{B\to A}$= (7.1 ± 0.2 ps)$^{-1}$. Based on this observation, we have assigned the observed components to the $\alpha(-)$ and $\alpha(+)$-modes of β-sheets. The influence of population exchange between the modes was found to have a large impact on the anisotropy dynamics obtained under broadband excitation conditions, whereas the anisotropy dynamics of narrowband-pump experiments are rather insensitive to this aspect. The population exchange is likely enabled by the fast, (sub-) picosecond conformational fluctuations of the β-sheets. The exchange rate constant shows little variation over a temperature interval from 2 to 20°C. This finding indicates that the protein backbone is flexible, even at temperatures near the freezing point (3.8°C, D_2O). This notion is corroborated by the absence of detectable secondary structure in circular dichroism spectroscopy, while the X-ray diffraction structure of flash-frozen crystals with strongly suppressed dynamics reveals two β-sheets, a β-bridge, and two 3_{10}-helices.

6.6 Appendix: Rate equations

The rate equations describing the time-dependent populations of the three states included in the model schematically depicted in Figure 6.5 can be written in matrix form as

$$\frac{d}{dt}\begin{pmatrix} N_A(t) \\ N_B(t) \\ N_0(t) \end{pmatrix} = \begin{pmatrix} -k_A - k_{A\to B} & k_{B\to A} & 0 \\ k_{A\to B} & -k_B - k_{B\to A} & 0 \\ k_A & k_B & 0 \end{pmatrix} \cdot \begin{pmatrix} N_A(t) \\ N_B(t) \\ N_0(t) \end{pmatrix} \tag{6.2}$$

The rate equations are integrated numerically and the rates of vibrational relaxation to the ground state $k_A = 1/T_{1a}$ and $k_B = 1/T_{1b}$ and the rate of population transfer $k_{A\to B}$= $1/T_{A\to B}$ are varied in a least-square minimization of the target functions Eqs. (5.2) and (5.3) given in the appendix of Chapter 5 until the best agreement with the experimentally obtained isotropic transient absorption changes $\Delta\alpha_{iso}$ are obtained. The rate of energy transfer in the reversed direction is constrained to obey the detailed balance condition $k_{A\to B}/k_{B\to A}$= $e^{-\Delta E/kT}$ where k, T and ΔE denote Boltzman's constant, the sample temperature in Kelvin and the energy gap between the two coupled amide modes of $\sim$ 35 cm^{-1}.

7 Structure and dynamics of a salt-bridge model system

We study the interaction between the ions methylguanidinium and trifluoroacetate dissolved in D_2O and dimethylsulfoxide (DMSO) with linear infrared spectroscopy and femtosecond two-dimensional infrared (2D-IR) spectroscopy. These ions constitute model systems for the side groups of arginine and glutamic and aspartic acid that are known to form salt bridges in proteins. We find that the salt-bridge formation of methylguanidinium and trifluoroacetate leads to a significant acceleration of the vibrational relaxation dynamics of the antisymmetric COO stretching vibration of the carboxyl moiety of trifluoroacetate. Salt-bridge formation has little effect on the rate of the spectral fluctuations of the CN stretching vibrations of methylguanidinium. The anisotropy of the cross peaks between the antisymmetric COO stretching vibration of trifluoroacetate and the CN stretching vibrations of methylguanidinium reveals that the salt-bridge is preferentially formed in a bidentate end-on configuration in which the two C=O groups of the carboxylate moiety form strong hydrogen bonds with the two ND_2 groups of deuterated methylguanidinium.

7.1 Introduction

Salt bridges are an ubiquitous structural motive in proteins formed between amino acids with a basic side chain (histidine, lysine or arginine), which are protonated at physiological pH conditions and hence bear a positive charge, and amino acids with an acidic side chain (aspartic/glutamic acid), which are deprotonated and hence bear a negative charge under all but the most acidic conditions. It has long been believed that the favorable coulombic interaction between the charged side chains would generally contribute to energetically stabilize the folded state of a protein over an unfolded state. However, this assumption has been challenged by the discovery of an energetically *unfavorable* salt bridge network in the Arc repressor protein [121]. Since then, other possible roles for salt bridges have been discussed. A recent study showed for example that the presence for geometrically optimized salt bridges can speed up the folding of α-helical peptides [122], which has led the authors to speculate if salt bridges might be involved in stabilizing intermediate or transition

states during the folding process, rather than the fully folded state of a peptide. Salt bridge interactions are often studied using model systems. Acetate is often used to mimic the natural amino acids glutamic acid (Glu) and aspartic acid (Asp), which both bear a carboxylate group in their side chain. The guanidinium cation forms a good model system for the naturally occurring amino acid arginine (Arg), which bears a guanidinium moiety in its side chain.
Deuterated guanidinium and guanidinium-like moieties are strong infrared absorbers in the region of 1600 cm^{-1} due to a mode that has mainly asymmetric CN stretching character with weak admixture of an ND_2-bending vibration [123]. The asymmetric CN stretch vibration is a two-fold degenerate mode in guanidinium, whereas in the methyl-guanidinium ion ($MeGd^+$) the degeneracy of this mode is broken by the methyl substitution, causing a splitting of the bands into a low-frequency band at 1585 cm^{-1} and a high-frequency band at 1615 cm^{-1} [124,125]. A similar splitting of the modes is also present in the side chain of the amino acid arginine. It was shown with two-dimensional infrared (2D-IR) spectrosopy that the CN stretching modes of arginine side-chains and of isolated guanidinium ions are strongly coupled and exhibit ultrafast energy transfer on a time scale of 2 ps [125,126]. Recently, 2DIR-spectroscopy was used for the first time to determine the structure of a salt bridge model system in dimethylsulfoxide (DMSO) [127]. From the cross-peaks resulting from mixing of the vibrational modes of guanidinium and acetate, the geometry of the complex could be inferred.
Here we use 2D-IR spectroscopy to study the salt-bridge interaction between methylguanidinium ($MeGd^+$) and trifluoroacetate (TFA^-) in D_2O and DMSO. The TFA^- anion exhibits sharp and intense infrared absorptions in the spectral region of 1670 to 1690 cm^{-1} due to the antisymmetric COO-stretch vibrations [128]. Trifluoroacetic acid (HTFA) is a strong organic acid (pKa in water 0.23) [129] and has found widespread use in many areas of preparative and analytical chemistry such as reversed-phase chromatography [130], mass-spectrometry [131] and solid-phase synthesis of peptides [132]. Furthermore, a stabilizing effect of TFA^- on urea-unfolded proteins has been reported [133]. The role of TFA^- in inducing conformational transitions of proteins towards a molten globule state by binding to positively charged sites and thereby minimizing intraprotein charge repulsion has been discussed [134]. An effect of the presence of small amounts of TFA^- anions on the size and morphology of fibrils formed by β-amyloid peptides has been reported [135]. By using $MeGd^+$ as a model for the side chain of the amino acid arginine in combination with TFA^-, we are able to identify the preferred binding geometry between the two ions.

7.2 EXPERIMENTAL METHODS

We study the salt-bridge interaction with the spectral hole-burning implementation of two-dimensional infrared (2D-IR) spectroscopy. The experiments in this chapter were performed with the two-dimensional infrared setup described in Section 3.2. Methylguanidinium chloride (MeGdCl), sodium trifluoroacetate

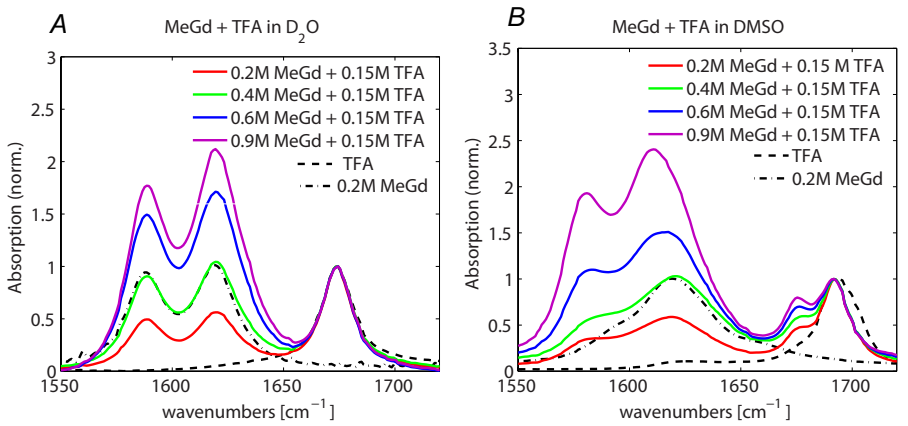

FIGURE 7.1. FTIR-absorption spectra of $MeGd^+$ dissolved in (A) D_2O and (B) DMSO. The spectra have been normalized to the COO-stretch absorption line in the 1670 - 1690 cm^{-1} region. Absorption spectra without TFA^- have been normalized to the maximum of the CN stretching band. The spectra in panel (A) have been corrected for the broad D_2O background absorption.

(NaTFA), and deuterated d^6-DMSO were obtained from Sigma-Aldrich and used without further purification. The samples were prepared by dissolving the salts in D_2O (Cambridge Isotope Laboratories, isotopic purity 99.96%). D_2O is used instead of H_2O to avoid absorption of the infrared pulses by the bending mode of H_2O around 1660 cm^{-1}. Prior to experiments in DMSO, hydrogen-deuterium exchange of $MeGd^+$ was performed by dissolving MeGdCl in D_2O and subsequently freeze drying the solution. After performing the procedure twice, the deuterated product is dissolved in DMSO.

7.3 Results and Discussion

7.3.1 Linear absorption spectra

Figure 7.1 shows linear absorption spectra of solutions of $MeGd^+$ and TFA in D_2O and DMSO. The spectra show a double peak structure around 1600 cm^{-1} that can be assigned to the CN-stretching vibrations of $MeGd^+$ [126]. The lower-frequency mode at 1590 cm^{-1} is associated with an antisymmetric vibration of CN bonds to the two ND_2 groups of $MeGd^+$, while the higher-frequency mode at 1620 cm^{-1} is dominated by a CN stretching vibration in which the stretching of the CN bond to the $NDCH_3$ group is in opposite phase to the symmetric stretching of the two CN bonds to the ND_2 groups [126]. The mode at 1620 cm^{-1} has a transition dipole moment that is oriented close to the bisectrix of the two ND_2 groups, and the transition dipole of the mode at 1590 cm^{-1} is oriented at an angle of $\sim 100°$ with respect to this bisectrix. The spectra also show a Lorentzian-shaped peak at 1690 cm^{-1} for solutions in DMSO and

at 1670 cm^{-1} for solutions in D_2O. This band is assigned to the antisymmetric COO-stretch vibration of the carboxylate group of TFA. The resonance position and the full width at half maximum (fwhm) of ~ 16 cm^{-1} are in good agreement with results from previous studies [128]. The addition of TFA^- to a solution of $MeGd^+$ in D_2O leads to minor variation in the absorption lines, leaving the center frequencies and the line width of both the CN-bands and the COO-band largely unaffected. For solutions in DMSO a strongly different behavior is observed. Most notably, in a solution containing both $MeGd^+$ and TFA^- the absorption line associated with the COO-stretch vibration acquires a double-peaked line shape. The amplitude of the lower frequency peak at 1670 cm^{-1} increases with concentration of $MeGd^+$, suggesting that this peak originates from TFA^- anions that form a hydrogen-bonded complex with $MeGd^+$ cations. The high-frequency peak at 1690 cm^{-1} also exhibits a small, but significant red-shift of a few wavenumbers with respect to the position of this absorption line in the absence of $MeGd^+$. Additionally, the two CN stretching modes of $MeGd^+$ split further apart with increasing $MeGd^+$ concentration. The features observed in the linear absorption spectra of Figure 7.1A suggest that in DMSO the $MeGd^+$ cation and TFA^- anion have a strong propensity to interact and to form complexes. The double-peak structure of the antisymmetric COO stretch absorption line suggests that the strength of the interaction is bimodal, with the 1670 cm^{-1}-peak representing strongly interacting $MeGd^+$-TFA^- complexes and the 1690 cm^{-1}-peak originating from rather weakly bound complexes.

7.3.2 2D-IR SPECTRA

In Figure 7.2(A-F) we show 2D-IR spectra measured for a solution of 0.4 M $MeGd^+$ and 0.4 M TFA^- in D_2O. Three peaks on the diagonal of the spectrum can be identified, each consisting of a negative (shown in blue) change in absorption ($\Delta\alpha$) at the fundamental frequency of the vibration and a red-shifted, positive $\Delta\alpha$ (shown in red) associated with the transition between the first and second excited state of the oscillator. Analogously to the FTIR-spectra in Figure 7.1, the peaks at 1590 cm^{-1} and 1620 cm^{-1} are assigned to the CN stretching vibrations of the $MeGd^+$-ion (referred to as ν_{CN}^{1590} and ν_{CN}^{1620} in the following) and the most intense peak at 1670 cm^{-1} is assigned to the antisymmetric COO-stretching vibration of TFA^-. The latter will be referred to as ν_{COO}. Furthermore, cross-peaks between ν_{CN}^{1590} and ν_{CN}^{1620} can be observed in the off-diagonal region of the spectrum. these can be best seen in the spectra shown in Figure 7.2(D-F), which have been obtained under perpendicular polarization of pump and probe pulses. Additionally, cross-peaks between the ν_{COO} vibration and the CN stretching modes of $MeGd^+$ can be identified, which are indicative of an interaction between the two ions.

In Figure 7.3, we plot the dynamics of the diagonal peaks of the isotropic 2D-IR spectrum that is constructed by adding the 2D-IR spectrum measured for parallel pump-probe polarization to 2 times the 2D-IR spectrum measured for perpendicular polarization (Eqn. 3.2). The decay of the diagonal peaks reflects the vibrational relaxation dynamics. With D_2O as the solvent, the vibrational

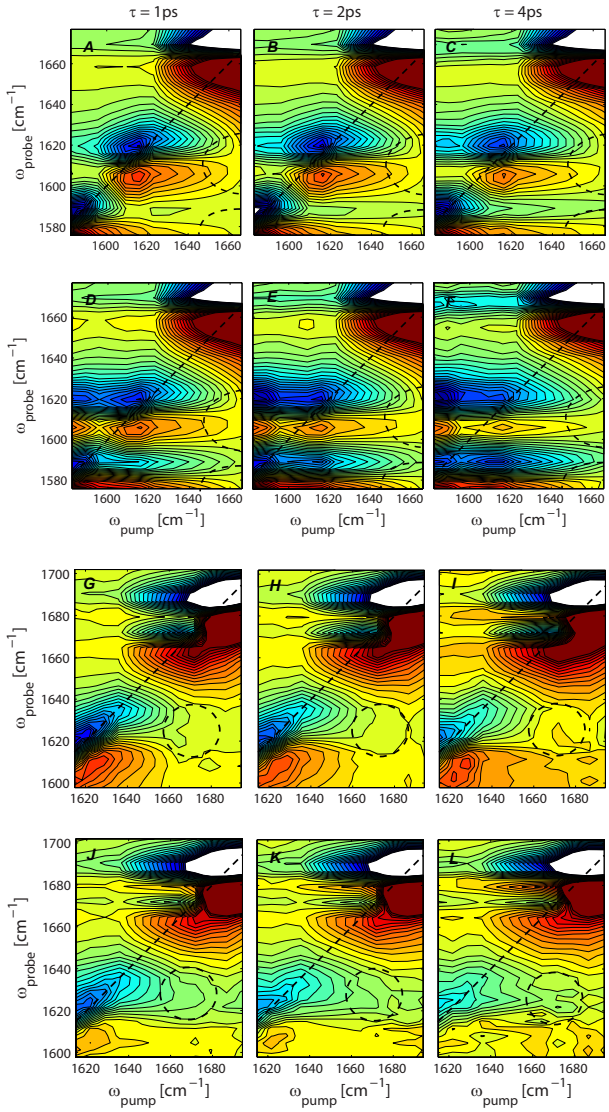

Figure 7.2. 2D-IR spectra at various delay times obtained for a solution of 0.4 M $MeGd^+$ + 0.4 M TFA^- in D_2O (a-f) and a solution of 0.6 M $MeGd^+$ + 0.15 M TFA^- in DMSO (g-l). The 2D-IR spectra (A-C) and (G-I) are measured with parallel polarization of the excitation and detection pulses, and 2D-IR spectra (D-F) and (J-L) are measured with perpendicular polarization of the excitation and detection pulses. Cross-peaks between TFA^- and $MeGd^+$ upon excitation of the ν_{COO} mode at 1670 cm^{-1} are indicated.

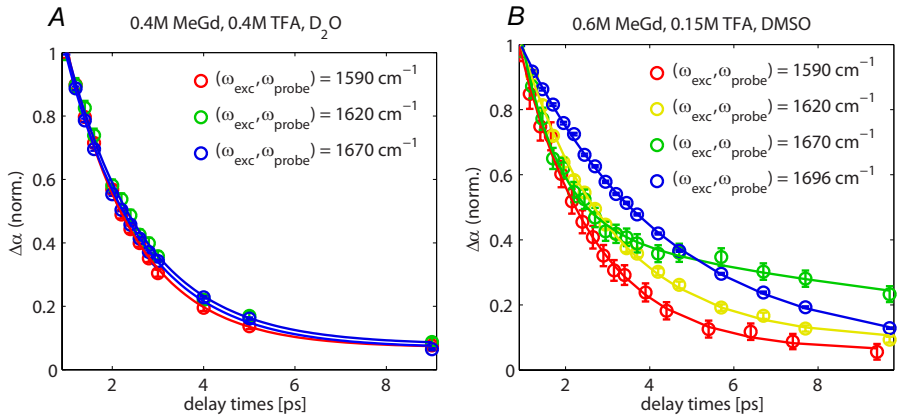

FIGURE 7.3. Diagonal dynamics of the 2DIR-spectra in Figure 7.2. The solid lines are fits of a mono-exponential decay (with an offset) to the data points.

relaxation of the ν_{CN}^{1590}, ν_{CN}^{1620} and the ν_{COO} modes all exhibit very similar vibrational relaxation time scales of 1.6±0.2 ps. In DMSO, the $\nu_{CN}^{1590}$and ν_{CN}^{1620} vibrations show quite similar relaxation dynamics as in D_2O, showing time constants of 1.8±0.2 and 2.1±0.3 ps, while the ν_{COO} bands show quite different relaxation behavior. The ν_{COO} band at 1670 cm^{-1} decays significantly faster (T_1 = 0.9±0.1 ps) than the ν_{COO} band at 1690 cm^{-1} (T_1 = 3.4±0.4 ps). The decay of the ν_{COO} mode at 1670 cm^{-1} is in fact biexponential and also contains a slow decay component with a time constant of > 10 ps, which we attribute to a slower thermalization of the relaxed vibrational energy. The strikingly faster decay of the ν_{COO} band at 1670 cm^{-1} compared to the ν_{COO} band at 1690 cm^{-1} band is likely the result of the presence of strong hydrogen bonds between the carboxylate group of TFA^- and the ND-groups of the $MeGd^+$ cation. The formation of a strong hydrogen bond increases the anharmonic coupling of the antisymmetric COO stretch vibration to lower-frequency accepting modes (including hydrogen-bond stretch vibrations), thereby speeding up the vibrational relaxation. The observation of a fast vibrational relaxation of the ν_{COO} band at 1670 cm^{-1} is thus consistent with the assignment of the 1670 cm^{-1} band to the antisymmetric COO stretch vibration of TFA^- anions in strongly bound salt-bridge complexes with $MeGd^+$ cations.

The reorientation dynamics of the TFA^- anions can be inferred from the dynamics of the anisotropy parameter R(t) associated with the diagonal peaks in the 2D-IR-spectrum. In Figure 7.4 we compare the anisotropy dynamics of the ν_{COO} mode of TFA^- anions absorbing at 1670 cm^{-1} with the anisotropy dynamics of the ν_{COO} mode of TFA^- anions absorbing at 1690 cm^{-1}. For the ν_{COO} mode at 1670 cm^{-1} we present the anisotropy dynamics of the induced absorption (1→2) instead of the anisotropy dynamics of the bleaching (0→1) because the bleaching signal of this mode partially overlaps with the 1→2-transition (induced absorption) of the ν_{COO} mode at 1690 cm^{-1}. We ob-

serve that the ν_{COO} mode at 1670 cm^{-1} shows a much slower anisotropy decay than the ν_{COO} mode at 1690 cm^{-1}. This supports our assignment of the ν_{COO} vibrations at 1670 cm^{-1} and 1690 cm^{-1} to strongly bound and weakly bound TFA$^-$ anions, respectively. The 2D-IR spectral line shapes give information on the homogeneous and inhomogeneous contributions to the line width of the absorption bands. In the case of inhomogeneous broadening the 2D-IR line shape is elongated along the diagonal. In Figure 7.2(A-F) it is seen that the diagonal peak of the ν_{COO} vibration shows negligible elongation along the diagonal which implies that its vibrational line shape exhibits very little inhomogeneity already at a delay time of 1 ps. This finding agrees with the very fast, sub-picosecond decay of the frequency-frequency correlation function (FFCF) of this vibration that was reported in Ref. [128]. With DMSO as solvent the diagonal peak associated with the ν_{COO} vibration of TFA$^-$ (Figure 7.2(G-L)) has a complex shape resulting from the interference between different transitions associated with the two partially overlapping peaks of this band. This complex shape also shows little elongation along the diagonal, which implies that the ν_{COO} vibration also shows little inhomogeneity when TFA$^-$ is dissolved in DMSO. The diagonal peaks of the ν_{CN}^{1590} and ν_{CN}^{1620} resonances of MeGd$^+$ also show little inhomogeneity when MeGd$^+$ is dissolved in D_2O (Figure 7.2(A-F)). The observed 2D-IR line shapes are nearly parallel to the pump-axis of the spectrum. This observation is in agreement with the $\sim$ 1 ps - decay time reported in Ref. [125] for the frequency-frequency correlation function (FFCF) of Gdm$^+$ in D_2O. In this work the apparent ultrafast spectral diffusion processes were attributed to the rapid reconfigurations of the solvation shell around the ion. In contrast, the

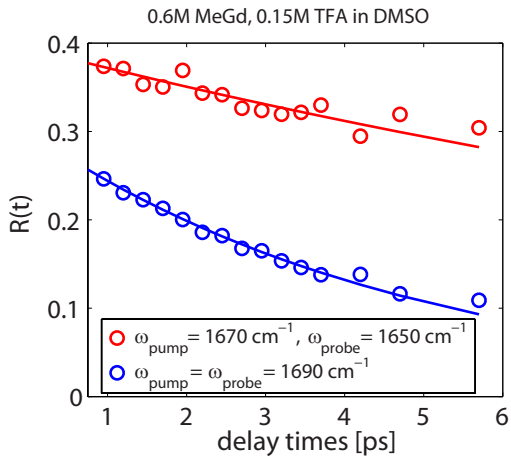

Figure 7.4. Comparison of the dynamics of the anisotropy parameter R(t) of the bleaching signal of the diagonal peak associated with weakly bound TFA$^-$ anions at ω_{pump}= ω_{probe}= 1690 cm^{-1}(blue circles) and the induced absorption signal of the diagonal peak of the strongly bound TFA$^-$ anions at ω_{pump}= 1670 cm^{-1}, ω_{probe}= 1650 cm^{-1} (red circles). The solid lines are mono-exponential fits.

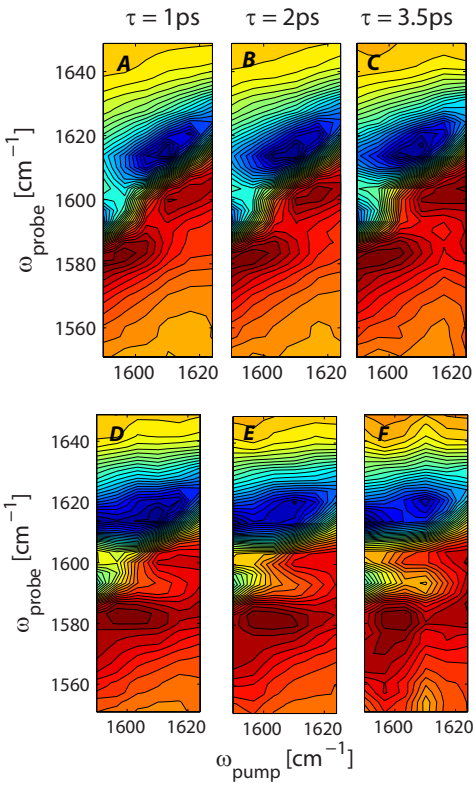

FIGURE 7.5. 2D-IR spectra of 0.6 M $MeGd^+$, 0.15 M TFA^- in D_2O at various delay times, obtained under parallel (A-C) and perpendicular (D-F) polarization of pump and probe pulses.

spectra obtained for a solution of $MeGd^+$ in DMSO (Figure 7.2(G-L)) show a strong elongation of the diagonal peak associated with the ν_{CN}^{1620}-mode along the diagonal of the spectrum that is not fully decayed at a delay time of 4 ps (Figure 7.2I). A similar diagonal elongation is also observed for the ν_{CN}^{1590}-mode in the 2D-IR-spectra shown in the Figures 7.5 and 7.6, where the ω_{pump}- and ω_{probe}-axes extend to lower frequencies. Hence, spectral diffusion is much slower in DMSO than in D_2O.

To quantify the spectral diffusion dynamics, we determined the delay dependence of the center line slope, i.e. the slope of the line that connects the frequency positions of the maxima of the negative absorption changes obtained at different excitation frequencies ω_{pump}. Plotting this slope as a function of delay time reflects the decay of the frequency-frequency correlation function [136]. In Figure 7.7 we present the results of this analysis for the ν_{CN}^{1620} vibration of $MeGd^+$ in DMSO, both in the presence and in the absence of TFA^-. The center line slope of ν_{CN}^{1620} is found to show a decay with a time-constant of 7.5±1 ps

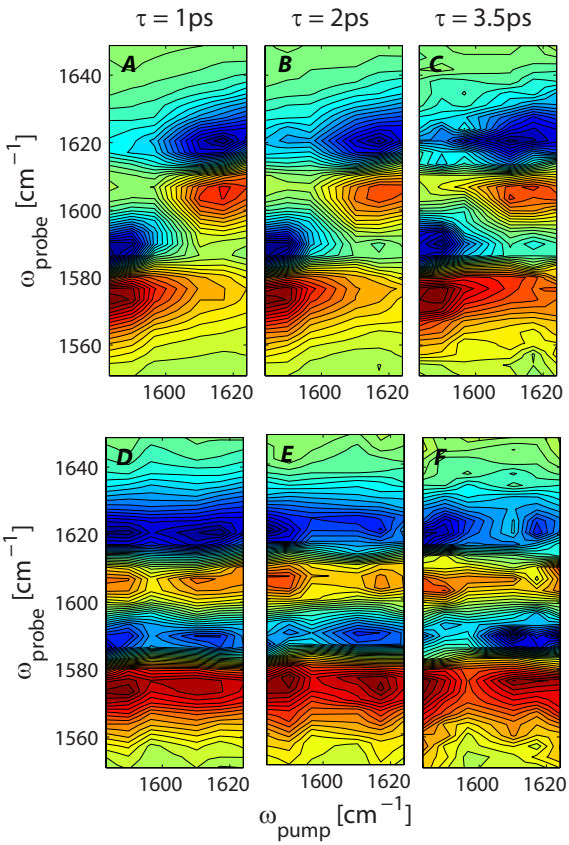

Figure 7.6. 2D-IR spectra of 0.2 M $MeGd^+$ in DMSO at various delay times, obtained under parallel (A-C) and perpendicular (D-F) polarization of pump and probe pulses

both in the presence and in the absence of TFA^-. The slightly higher starting value seen in Figure 7.7 in the presence of TFA^- indicates that the formation of salt bridges increases the width of the frequency distribution of the ν_{CN}^{1620} vibration. The insensitivity of the spectral diffusion dynamics with respect to the addition of TFA^- shows that the spectral fluctuations likely result from interactions with surrounding DMSO solvent molecules that show little dependence on the presence of the salt bridge. This explanation is in line with the fact that the ν_{CN}^{1620} line shape is near homogeneous in D_2O, where the interactions with the light D_2O molecules are expected to fluctuate on a much shorter time scale. It should be noted that, due to the spectrally narrow bandwidth of the excitation pulses in our experiment, we cannot resolve the dynamics occurring on time scales shorter than ~ 1 ps. Hence, the frequency-frequency correlation of the ν_{CN}^{1620}-mode of $MeGd^+$-ions embedded in a salt-bridge complex may in fact contain an additional sub-picosecond component.

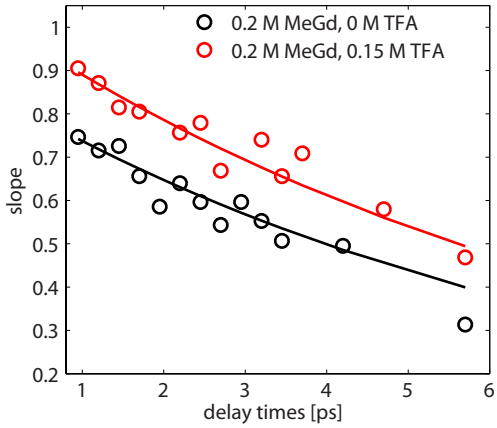

FIGURE 7.7. Central line slope as a function of delay time for the symmetric CN stretching mode of $MeGd^+$ at 1620 cm^{-1}. Black symbols show the data obtained for a solution of 0.2 M MeGdCl in DMSO, and red symbols represent the data obtained for a solution of 0.2 M MeGdCl and 0.15 M NaTFA in DMSO.

7.3.3 CROSS-PEAK ANISOTROPY OF THE 2D-IR SPECTRA

The anisotropy of the cross-peaks in the 2DIR-spectrum reveals the relative orientation of the transition dipole moments of the excited and probed vibrations [37, 127, 137, 138]. The dashed line in Figures 7.8 and 7.9 is a weighted average of a subset of the anisotropy values within a given frequency range. In this weighted average only anisotropy data points that correspond to a certain minimum isotropic signal (the value is given in the figure captions) have been included, since the anisotropy value is no longer reliable in case the isotropic signal is close to zero. In Figure 7.8 we show the frequency dependence of the anisotropy parameter R(ω) at 1 ps delay time upon selective excitation of the ν_{CN}^{1590} mode and the ν_{CN}^{1620} mode of $MeGd^+$. The isotropic spectra (solid lines) clearly show that excitation of either mode leads to a response of the other mode. This off-diagonal response shows that the two modes are coupled. Both the transient spectra and the frequency dependent anisotropy values are very similar for solutions in D_2O (Figure 7.8(A,C)) and DMSO (Figure 7.8(B,D)), which implies that the intramolecular coupling between the ν_{CN}^{1590} mode and the ν_{CN}^{1620} mode is largely unaffected by interactions with the solvent.
In the diagonal region (same mode excited and probed) the anisotropy ranges between 0.3 and 0.4, which shows that there is very little reorientational motion in the first picosecond after the excitation. In the off-diagonal region the anisotropy parameter R(ω) has a negative value around -0.05. The value of the off-diagonal anisotropy can be related to the angle θ between the transition dipoles using the relation $R = \frac{1}{5}(3\cos^2\theta - 1)$. We infer an angle of 120±5° between the transition dipole moments of the two modes, which is somewhat

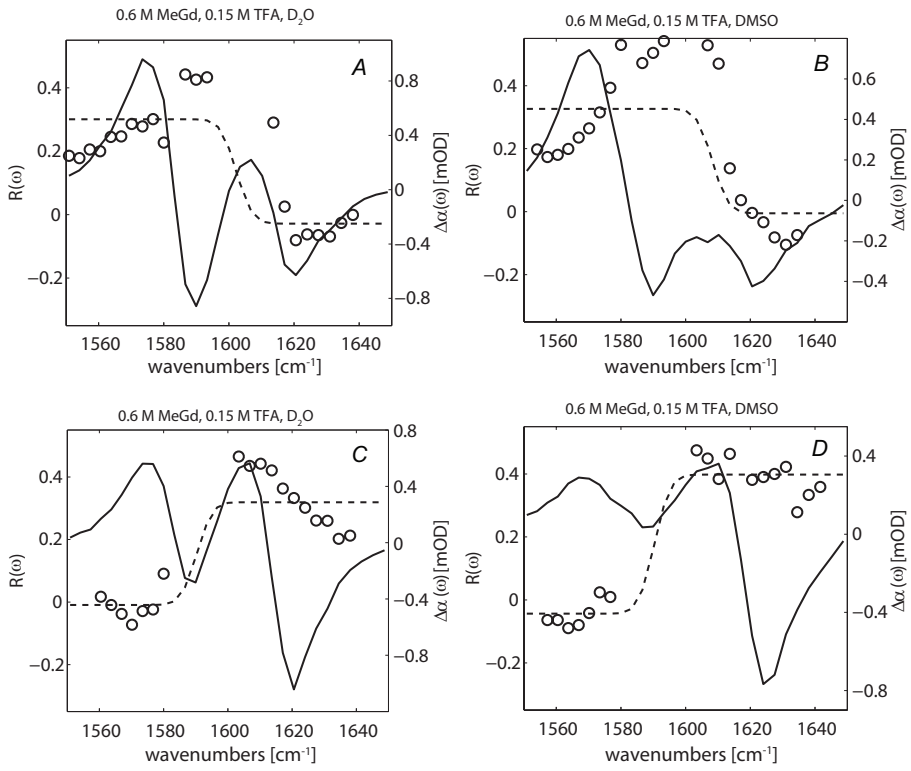

FIGURE 7.8. Cuts through the CN stretching region of 2D-IR spectra at a delay time of 1 ps after excitation of the ν_{CN}^{1590} mode of $MeGd^+$ (a,b) and of the ν_{CN}^{1620} mode (c,d) of $MeGd^+$, measured for a solution of 0.6 M MeGdCl and 0.15 M NaTFA in D_2O (a,c) and DMSO (b,d). The symbols denote the frequency-dependent anisotropy $R(\omega)$ (left vertical axis), and the solid lines represent the isotropic transient spectrum (right vertical axis). The dashed line is a weighted average of the anisotropy values of the diagonal and cross-peaks. Only anisotropy data points that correspond to an isotropic signal $\Delta\alpha_{iso} > 0.15$ mOD have been included.

higher than the value of 115° that was reported in Ref. [126] for arginine. The angle of 120° agrees well with the assignment of the ν_{CN}^{1590} mode to an antisymmetric vibration of the CN bonds to the two ND_2 groups of $MeGd^+$, and of the ν_{CN}^{1620} mode to an antisymmetric stretching of the CN bond to the $NDCH_3$ group with respect to the symmetric stretching of the two CN bonds to the two ND_2 groups [126].

In Figure 7.9, we show the transient spectra and anisotropy values over a frequency range that encompasses both the CN stretching vibrations of $MeGd^+$ and the COO-stretching vibrations of TFA^-. Excitation of the ν_{CN}^{1620} or the ν_{COO} band at 1670 cm^{-1} gives a clear cross-peak response at the other type of modes due to the formation of a salt bridge between $MeGd^+$ and TFA^-.

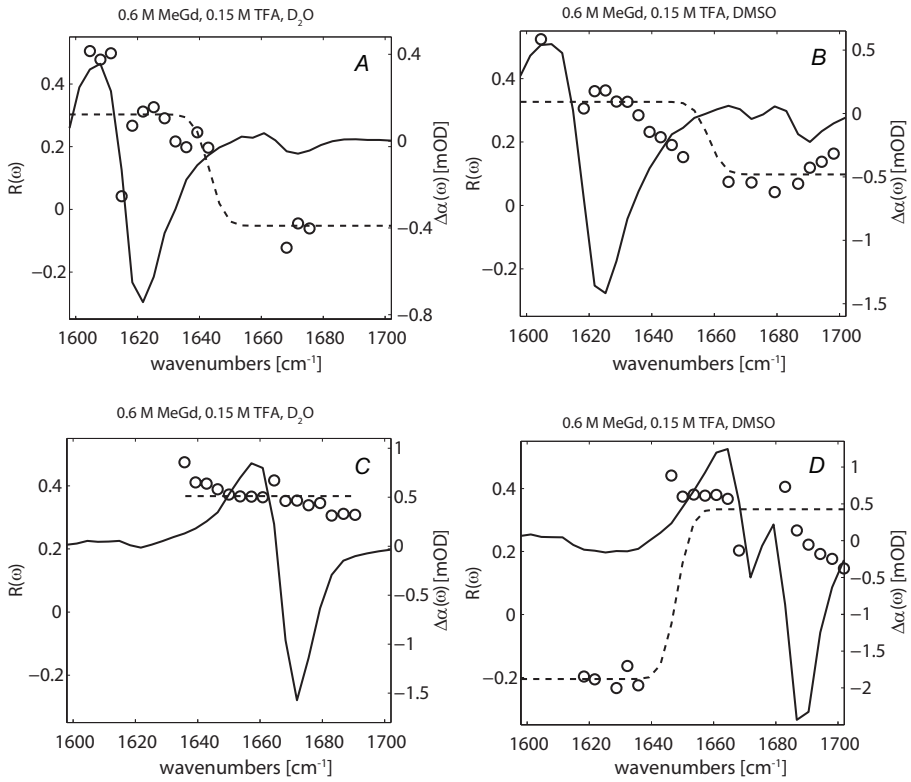

FIGURE 7.9. Cuts through the 2D-IR spectra at 1 ps delay time after excitation of the ν_{CN}^{1620} mode of $MeGd^+$ (A,B) and the ν_{COO} mode at 1670 cm^{-1} of TFA^- (C,D), measured for a solution of 0.6 M MeGdCl and 0.15 M NaTFA in D_2O (A,C) and DMSO (B,D). The symbols denote the frequency dependent-anisotropy R(ω) (left vertical axis), and the solid lines represent the isotropic transient spectrum (right vertical axis). The dashed line is a weighted average of the anisotropy values of the diagonal and cross-peaks. Only anisotropy data points that correspond to an isotropic signal $\Delta\alpha_{iso} > 0.05$ mOD have been included.

The cross-peaks in the 1670 - 1690 cm^{-1} region for $\omega_{pump} = 1620$ cm^{-1} are more pronounced for a solution in DMSO (Figure 7.9B) than for a solution in D_2O (Figure 7.9A). This result is not unexpected as DMSO has a lower dielectric constant than water ($\epsilon_{DMSO} = 48$, $\epsilon_{water} = 80$), which leads to a stronger coulombic attraction between the two oppositely charged ions. Hence $MeGd^+$ and TFA^- show a higher propensity to form salt-bridge complexes in DMSO than in D_2O. Excitation of the ν_{CN}^{1620} mode of $MeGd^+$ in DMSO leads to two distinct cross-peaks at $\omega_{probe} = 1670$ cm^{-1} and $\omega_{probe} = 1690$ cm^{-1} which shows that both ν_{COO} modes are coupled to the ν_{CN}^{1620} mode (Figure 7.9B). The observation of both ν_{COO} modes at 1670 cm^{-1} and 1690 cm^{-1} following excitation of ν_{CN}^{1620} shows that both ν_{COO} bands contain contributions from hydrogen-bonded

complexes of $MeGd^+$ and TFA^-. This points at a bimodal distribution of binding strengths.

Salt bridges exist in different binding geometries in proteins. In a bidentate binding geometry both C=O groups of a carboxylate moiety are hydrogen bonded to two N–D groups of a guanidinium moiety, whereas in a monodentate configuration only a single C=O group and a single N–D group form a hydrogen bond. In general the salt-bridge interaction between arginine and aspartic or glutamic acid has a prevalence for a bidentate configuration [139]. There are two possible configurations for this bidentate binding interaction. The two C=O groups can either bind to two ND_2-groups of the guanidinium-moiety (end-on) or bind to an ND_2 group and the NDR group that includes the alkyl R substituent (side-on) [139]. The salt-bridge configuration in proteins will strongly depend on steric effects. For instance, it has been found with 2D-IR spectroscopy that a bidentate geometry is preferred in a model β-turn polypeptide, whereas a monodentate configuration is preferred in a model α-helical peptide [140]. The geometry of the salt bridge formed between $MeGd^+$ and TFA^- can be derived from the polarization-resolved 2D-IR spectra of Figure 7.2.

The anisotropy of the ν_{COO} mode following excitation of the ν_{CN}^{1620} mode has a value close to zero (Figure 7.9(A,B)). This finding shows that the response of the ν_{COO} modes is dominated by cross-anharmonic coupling between the ν_{CN}^{1620} and ν_{COO} modes and not the result of direct excitation of the very low-frequency wing of the absorption band of the ν_{COO} vibrations, as this would result in a value of $R(\omega)$ of $\sim$0.4. The small value of the anisotropy indicates that the transition dipole moments of the ν_{CN}^{1620} and ν_{COO} modes are oriented at a large relative angle. For solutions of $MeGd^+$ and TFA^- in D_2O the signal of the ν_{CN}^{1620} mode following excitation of the ν_{COO} mode is very weak (Figure 7.9C), thus preventing an accurate determination of its anisotropy. The weak signal of the cross peak indicates that there exists a large fraction of free (uncomplexed) TFA^- in D_2O. Excitation of the ν_{COO} mode at 1670 cm^{-1} for a solution of $MeGd^+$ and TFA^- in DMSO yields a clear cross-peak signal at the ν_{CN}^{1620} mode with an anisotropy value of $R(\omega)$ = -0.2 (Figure 7.9D). Excitation of the ν_{COO} mode at 1670 cm^{-1} in DMSO exclusively excites TFA^- molecules forming salt-bridge complexes. Hence, the contribution of directly excited ν_{COO} modes to the signal measured in the frequency range of the ν_{CN}^{1620} mode will be smaller than in the case of Figure 7.9B, where the signal measured in the frequency region of the ν_{COO} modes also has a significant contribution of uncomplexed TFA^- anions at the given stochiometry of $MeGd^+$:TFA^- = 4:1.

The excitation of the CN-mode at 1620 cm^{-1} is therefore *not* selective for $MeGd^+$ ions in salt-bridge complexes, but also involves the excitation of unbound $MeGd^+$ ions. This latter species does not give rise to a cross-peak signal at 1670 cm^{-1}, but its high-frequency wing gives rise to a transient absorption change in the 1670 cm^{-1}-region. This signal will have a high (R = 0.4) anisotropy value and adds to the low anisotropy (R = -0.2) expected for the (ω_{pump} = 1620 cm^{-1}, ω_{probe} = 1670 cm^{-1})-cross-peak, resulting in the intermediate anisotropy value of R = 0.1 that is observed in Figure

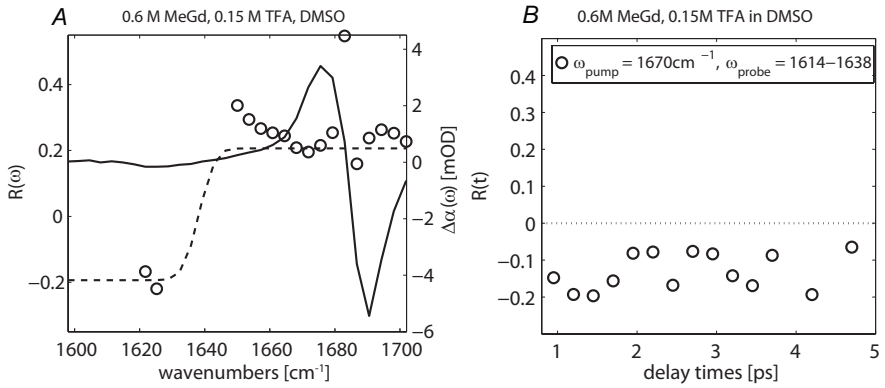

FIGURE 7.10. (A) Cuts through the 2D-IR spectra at 1 ps delay time after excitation of the ν_{COO} mode of weakly bound TFA^- anions at 1690 cm^{-1}, measured for a solution of 0.6 M MeGdCl and 0.15 M NaTFA in DMSO. The symbols denote the frequency dependent anisotropy R(ω) (left vertical axis), and the solid lines represent the isotropic transient spectrum (right vertical axis). The cross-peak anisotropy of R $\approx$ -0.2 suggests that weakly bound salt bridge complexes between $MeGd^+$ and TFA^- also adopt an end-on geometry, similar to the strongly bound complexes. (B) Time-dependence of the cross-peak anisotropy associated with the ν_{CN}^{1620}-mode upon excitation of the ν_{COO}-1670 cm^{-1}-mode. Each data point has been obtained by averaging along the ω_{probe}-axis from 1614 to 1638 cm^{-1}.

7.9B. Since the 1670 cm^{-1}-peak results exclusively from TFA^- anions in salt-bridge complexes, the aforementioned effect does not affect the anisotropy of the (ω_{pump}= 1670 cm^{-1}, ω_{probe}= 1620 cm^{-1})-cross-peak, making the anisotropy in Figure 7.9D a reliable measure for the angle between the transition dipoles of the COO-stretch vibration and the CN-stretch vibration in a salt-bridge complex.

For the cross-peak of the ν_{COO}-mode around 1690 cm^{-1} and the ν_{CN}^{1620}-mode, originating from weakly-bound salt bridge complexes, we also observe a value of R = -0.2 in Figure 7.10A. It can be excluded that the cross-peak in the region of the ν_{CN}^{1620}-vibration originates from excitation of the high-frequency wing of the ν_{COO}-vibration of strongly bound TFA^- anions based on the absence of any bleaching-like feature 1670 cm^{-1} in the isotropic transient spectrum of Figure 7.10A. In Figure 7.10B we present the dynamics of the cross-peak around ω_{probe} = 1620 cm^{-1} upon excitation of the ν_{COO}-mode at 1670 cm^{-1}. The anisotropy shows little time dependence (within the experimental uncertainty) up to a delay time of 5 ps, indicating that the reorientation is a quite slow process, in agreement with the observation of the slow decay of the anisotropy of the diagonal ν_{COO}-peak at 1670 cm^{-1} in Figure 7.4.

An anisotropy value of R(ω) = -0.2 corresponds to a relative angle of 90° between the transition dipole moments of the ν_{COO} and ν_{CN}^{1620} modes. The results of Figures 7.9(A,B,D) and 7.10A thus show that the transition dipole moments

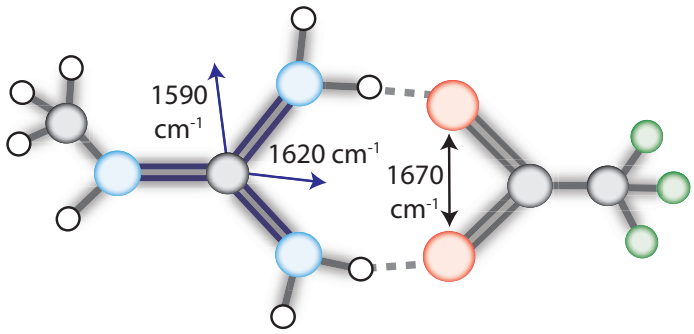

Figure 7.11. Geometry of the salt bridge formed between $MeGd^+$ and the TFA^--anion as inferred from the polarization-resolved 2D-IR spectrum. The cross-peak anisotropy values indicate that the complex adopts an bidentate end-on geometry, with the carboxylate-group of TFA^- binding to the two ND_2-groups of the $MeGd^+$ cation. Arrows depict the transition dipoles of the CN stretching modes of $MeGd^+$ and the ν_{COO}-mode of the TFA^--anion.

of ν_{CN}^{1620} and the antisymmetric ν_{COO}-vibrations have a nearly perpendicular orientation in the salt-bridged complexes of $MeGd^+$ and TFA^-. This finding indicates a geometric arrangement as outlined in Figure 7.11. The carboxylate group of the TFA^--anion binds in a bidentate end-on configuration to the two ND_2-groups of the $MeGd^+$ cation.

7.4 Conclusions

We study the interaction between methylguanidinium ($MeGd^+$) and trifluoroacetate (TFA^-) in D_2O and DMSO using linear infrared spectroscopy and femtosecond two-dimensional infrared (2D-IR) spectroscopy. For methylguanidinium we probe the CN stretching vibrations at 1590 and 1620 cm^{-1}, for TFA^- we probe the antisymmetric COO stretching vibration with a frequency of 1670 cm^{-1} in D_2O and frequencies of 1670 cm^{-1} and 1690 cm^{-1} in DMSO. We find that in both solvents $MeGd^+$ and TFA^- have a strong tendency to form salt-bridge complexes in which the C=O groups of TFA^- from strong hydrogen bonds to two N–D groups of $MeGd^+$.

In DMSO the formation of the salt bridge leads to a strong acceleration of the vibrational relaxation of the antisymmetric COO vibration of TFA^-, from 3.4±0.4 ps to 0.9±0.1 ps. Salt bridge formation has little effect on the time constant of vibrational relaxation of the CN stretching vibrations. Both CN stretching vibrations at 1590 and 1620 cm^{-1} have a vibrational relaxation time of ∼2 ps, irrespective of the solvent or formation of a salt-bridge. In DMSO the CN stretching vibrations show quite slow spectral diffusion with a time constant of 7.5±1 ps. This time constant is the same for isolated $MeGd^+$ and for $MeGd^+$ contained in a salt-bridge complex, showing that the spectral fluctuations are governed by intermolecular interactions with the DMSO solvent

molecules. This result is consistent with the observation that the spectral diffusion is much faster in D_2O where the interactions with the light D_2O molecules fluctuate on a much shorter time scale.

The anisotropy of the cross peaks of the 2D-IR spectrum show that the transition dipole moments of the two CN stretching vibrations at 1590 and 1620 cm^{-1} have a relative angle of 120°, which agrees with an assignment of the 1590 cm^{-1} mode to an antisymmetric vibration of the CN bonds to the two ND_2 groups of $MeGd^+$, and of the 1620 cm^{-1} mode to a stretching of the CN bond to the $NDCH_3$ group that is in opposite phase to the symmetric stretching of the two CN bonds to the ND_2 groups [126]. From the anisotropy values of the cross peaks of the CN stretching vibration at 1620 cm^{-1} and the antisymmetric ν_{COO} mode of TFA^- it follows that the transition dipole moments of these vibrations have a relative orientation that is close to perpendicular. This result shows that the salt-bridge complex of $MeGd^+$ and TFA^- has a preferred bidentate end-on configuration in which the two C=O groups of TFA^- form strong hydrogen bonds to the two ND_2 groups of $MeGd^+$ (Figure 7.11).

8 Probing chirality at aqueous interfaces

We demonstrate that the absolute configuration of complex chiral molecules at an aqueous interface can be determined using heterodyne-detected vibrational sum-frequency generation (VSFG). We perform VSFG spectroscopy with a polarization combination that selectively probes chiral molecular structures. We use frequencies that are far detuned from electronic resonances to probe the chiral molecular structures with high surface specificity. By heterodyning the generated sum-frequency light with light of a local oscillator, we enhance the signal and we determine the phase of the sum-frequency light generated by the chiral molecules. With this approach we can distinguish right-handed (L-type) and left-handed (D-type) helical peptides at a water-air interface. We thus show that heterodyne-detected VSFG allows for the determination of the absolute configuration of complex macromolecules with monolayer sensitivity.

8.1 Introduction

The determination of the absolute configuration of a chiral molecule is of importance in many areas of (bio)chemistry, ranging from enantioselective catalysis, supramolecular chemistry to protein biochemistry. Chirality is often connected to a stereogenic carbon atom. Macromolecules can also exhibit chirality if their building blocks are arranged in such a way that the macromolecular assembly is non-superimposable with its mirror image. Examples of supramolecular chirality that is related to the intrinsic chirality of the building blocks are biological macromolecules, such as proteins, peptides and nucleic acids, and self-assembled polymer-helices [141]. The assembly of supramolecular structures from achiral building blocks has been demonstrated [142, 143], a process likely related to an asymmetry in the molecular forces driving the assembly.
Only few measurement techniques are capable of determining the absolute configuration of chiral molecules. One of these techniques is anomalous X-ray scattering dispersion [20]. More common is circular dichroism (CD) with which the difference in absorption of left- and right-circularly polarized light is measured. Electronic CD-spectroscopy in the near-ultraviolet region is routinely employed to quantify secondary structural elements in peptides and proteins [144, 145].

Vibrational circular dichroism in the mid-infrared [146–149] and Raman optical activity [150–152] potentially hold a greater promise for the structural elucidation of small molecules in solution, owing to their sensitivity to distinct vibrational marker bands.

Since the aforementioned experimental approaches are all based on linear optical techniques, their enantiomer-specificity results from magnetic dipole or electric quadrupole interactions, which are inherently weak, and much effort has been devoted to the enhancement of electronic and vibrational CD-spectroscopic signatures, both in terms of instrumentation and chemical modification of the samples [21, 25, 28, 153]. Additionally, the potential of non-linear optical techniques such as second harmonic generation (SHG) and sum-frequency generation (SFG) to study chiral molecules has been increasingly recognized over the past years. The first non-linear optical study of chiral molecules was reported by Hicks and co-workers [154, 155], who observed a pronounced difference in the efficiency of SHG from oriented surface layers of 2,2'-hydroxy-1,1'-binaphtyl using either left- or right-circularly polarized light.

Vibrational SFG-spectroscopy (VSFG), illustrated in Figure 8.1A, is a second-order non-linear optical technique, in which an infrared and a visible pulse are combined at an interface to generate light at their sum-frequency. This generation is enhanced in case the infrared light is in resonance with specific molecular vibrations. Within the electric dipole approximation, SFG is only allowed in media that lack inversion symmetry such as chiral media [156] or interfaces [157], where the inversion symmetry is inherently broken. Vibrational SFG therefore offers the structural resolution of vibrational spectroscopy with the specificity to non-centrosymmetric media, thus combining spectroscopic aspects ideal for the study of chirality at interfaces.

The application of VSFG to the study of chiral molecules has been pioneered by Shen and co-workers [24, 158]. In these early studies, chiral VSFG-spectra were obtained from the bulk of optically active solutions, and the detection of a chiral VSFG-spectrum from a molecular monolayer was only possible under electronically resonant conditions [24]. Recently, chiral VSFG-spectra of protein monolayers at the air-water interface were successfully measured in the spectral region of the amide I vibration (C=O-stretch) and the NH-stretch vibration [159–162]. This approach allowed for the first time the monitoring of complex structural rearrangements of proteins with interface specificity. In particular, Yan and co-workers have succeeded in studying the aggregation behavior of amyloidic peptides at water-lipid interfaces and found that the aggregation of the human islet amyloid peptide at the water-lipid interface proceeds via an α-helical intermediate before folding into a β-sheet structure [161]. Such structural transformations taking place at aqueous interfaces cannot be studied with many other techniques, as these do not provide surface specificity (such as 2-dimensional infrared spectroscopy [163]), or merely probe interfacial ordering without the ability to resolve structural features (such as X-ray reflectivity measurements [164]).

In the aforementioned studies, only the intensity of the generated SFG-light $I_{sfg} \propto |\chi^{(2)}|^2$ was detected, from which only the absolute value of the complex-

valued, 2^{nd}-order nonlinear susceptibility $\chi^{(2)}$ can be inferred [165–170]. The non-linear susceptibility $\chi^{(2)}_{chiral}$ of a chiral molecule contains elements that change sign between enantiomers, and thus valuable information on the absolute configuration of chiral molecules could be obtained in case the real and imaginary part of $\chi^{(2)}_{chiral}$ could be determined. A phase-resolved chiral SFG-spectrum has been reported for the CH-stretch vibrations of the R- and S-enantiomers of limonene under electronically off-resonant conditions [171], in which the signal originated from the bulk of the solution and therefore did not provide access to chirality at interfaces, and recently also for a variety of proteins at the air-water interface [172]. Here, we demonstrate heterodyne-detected chiral VSFG spectroscopy of two enantiomeric forms of a complex (bio)macromolecule at the water-air interface. We show that this method allows for an unambiguous identification of the absolute configuration of macromolecules at interfaces.

8.2 The molecular origin of the SFG-signal

The macroscopic non-linear susceptibility $\chi^{(2)}_{IJK}$, where the indices I,J,K refer to the laboratory coordinate frame (X,Y,Z), is linked to the microscopic molecular hyperpolarizability β_{ijk}, where the indices i,j,k refer to the molecular coordinate frame (x,y,z). The hyperpolarizability β_{ijk} in turn is determined by the transition dipole moment and the Raman polarizability of a molecular vibration as [173]

$$\chi^{(2)}_{IJK} = N \sum_{i,j,k} \langle R_{Ii} R_{Jj} R_{Kk} \rangle \beta_{ijk} \tag{8.1}$$

where R denote rotation matrices and $\langle ... \rangle$ denotes an orientational average. For an isotropic surface the orientational average corresponds to an integral of the form $\int_0^{2\pi} d\phi$ and for an isotropic three dimensional distribution to $\int_0^{\pi} \sin\theta d\theta \int_0^{2\pi} d\phi \int_0^{2\pi} d\psi$, where θ, ϕ and ψ denote the Euler angles.
Chirality can be due to local chiral molecular groups giving rise to chiral tensor elements like β_{xyz} or more generally β_{ijk} with $i \neq j \neq k$ [173]. In addition, elements of the molecular hyperpolarizability tensor such as β_{xxz}, that are *achiral* in the molecular frame, can contribute to $\chi^{(2)}_{chiral}$ in case a chiral arrangement of chromophores is present, such as in a helix with a well-defined handedness [173–175].
In order to understand the chiral specificity of particular polarization combinations in an SFG-experiment, we consider the point groups to which chiral and achiral surfaces belong. In the following, we assume a laboratory coordinate frame in which the X- and Y-axis span the interfacial plane and the Z-axis is normal to the surface. A chiral surface belongs to the C_∞-point group, whereas an achiral surface has $C_{\infty V}$-symmetry. The latter point group contains mirror planes as additional symmetry operations compared to the C_∞-symmetry of chiral surfaces. Because of the mirror symmetry, all elements of the non-linear susceptibility tensor $\chi^{(2)}_{IJK}$, where the indices I,J,K refer to the laboratory co-

ordinate frame (X,Y,Z), with $I \neq J \neq K$ such as $\chi^{(2)}_{XYZ}$ are zero for a surface composed of *achiral* molecules, and only elements with two equal indices such as $\chi^{(2)}_{XXZ}$, $\chi^{(2)}_{YYZ}$ are non-zero [173]. In contrast, elements $\chi^{(2)}_{IJK}$ with $I \neq J \neq K$ can be non-zero for a surface containing *chiral* molecules.
A chiral VSFG signal can in principle originate both from the bulk and the surface of a solution. However, for an isotropic bulk system, the generation of a chiral SFG signal requires the antisymmetric part of the Raman tensor to be nonzero, which is only the case at frequencies close to electronic resonances [23,24,158,173,176]. In an aqueous solution, the helices are isotropically oriented in three dimensions, and thus $\chi^{bulk}_{chiral} = 0$, if the Raman-tensor is totally symmetric, which is usually the case if ω_{VIS} and ω_{SFG} are far away from electronic resonances. The surface possesses C_∞ symmetry which implies that the orientational average in Eq. (8.1) is only performed over the in-plane orientation of the molecules. Hence, $\chi^{surface}_{chiral}$ can be non-zero, even for a totally symmetric Raman-tensor [173,174]. In the present experiments ω_{VIS} and ω_{SFG} are far away from electronic resonances, meaning that the chiral SFG signal is only generated by protein molecules at the water-air interface. The phase of $\chi^{surface}_{chiral}$ can be determined by comparing the phase of the chiral SFG signal with the phase of the SFG signal from a system with a known $\chi^{(2)}$ (see below).

8.3 Results and Discussion

We use VSFG to study the biologically relevant type I antifreeze peptide (AFP1) [177] at the water-air interface. AFP1 is naturally found in the body fluids of the cold-adapted winter flounder fish, forming a natural protection against freeze damage from ice-crystals by adsorbing to the ice-crystal surfaces and inhibiting further growth [178]. AFP1 is 37 amino acids in length and fully α-helical. The handedness of an α-helix is defined by the chirality of the amino acids (L- or D-enantiomers) and constitutes a form of supramolecular chirality. We have synthesized two AFP1 peptides with either (L)- or (D)-amino acid configuration, which allows us to selectively control the handedness of the helix and hence the absolute configuration of the molecule. The helicity of (L)- and (D)-AFP1 was studied by circular dichroism. The CD-spectra in Figure 8.2C show the characteristics of an α-helix, but with opposite sign for (L)-AFP1 and (D)-AFP1, confirming that the two peptides form indeed helices with opposite handedness. The temperature-dependence of the CD-spectra shows that the thermal stability of (L)- and (D)-AFP1 is highly similar and agrees with literature values (see Appendix B). An independent activity assay (sonocrystallization) demonstrated that (L)- and (D)-AFP1 show also equal antifreeze activity (see Appendix B).

The sum-frequency generation setup described in Section 3.3 has been used to record VSFG-spectra of AFP1 at the air-water interface. Figure 8.1B shows the intensity VSFG-spectrum of (L)-AFP1 obtained under ssp-polarization conditions (s-polarized SFG, s-polarized VIS, p-polarized IR). The spectrum consists of a broad band around $\sim$ 3200 cm^{-1} originating from the OH-stretch

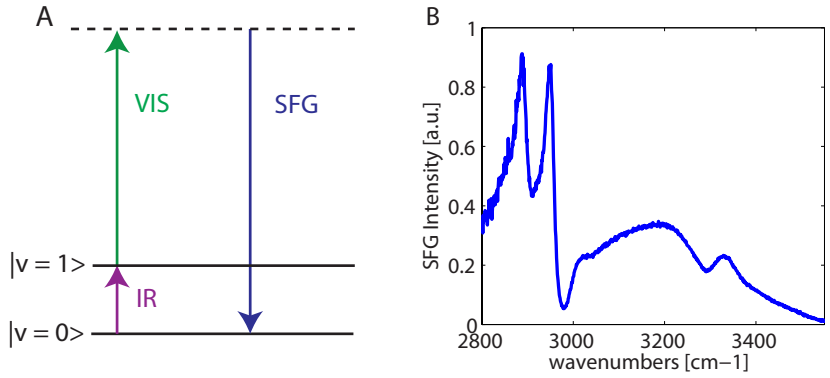

FIGURE 8.1. (A) Schematic representation of the sum-frequency generation process: a femtosecond mid-infrared pulse (IR) couples the vibrational ground-state $|0>$ and the first vibrationally excited state $|1>$ of the NH-stretch vibration of the peptide backbone and the resulting coherence is upconverted by a non-resonant 800 nm-pulse (VIS), leading to the emission of light at the sum-frequency (SFG). (B) Direct SFG-spectrum obtained from an aqueous solutions of (L)-AFP1 using ssp polarization conditions. The sharp resonances below 3000 cm^{-1} originate from CH-stretch vibrations of the peptide and the broad resonance centered around $\sim$ 3200 cm^{-1} originates from the OH-stretch vibration of interfacial water molecules. A peak on the high frequency side of the broad OH-band can be observed around 3350 cm^{-1}.

vibration of interfacial water molecules, and two additional narrow resonances at 2890 cm^{-1} and 2950 cm^{-1}, which originate from the symmetric and anti-symmetric CH_3-stretching vibrations [179] of methyl-groups in the amino acid side chains of AFPI. Additionally, a peak on the high frequency side of the broad OH-band is observed at 3350 cm^{-1}. Based on its resonance position and its narrow line-width, we assign this band to an NH-stretch vibration. While the signal could in principle also originate from NH-groups in the side-chains of amino acids (lysine and arginine) or the N-terminus/amidated C-terminus of the peptide, the overwhelming prevalence of backbone-NH-groups (36) over side-chain (2) or N/C-terminal NH-groups (2) supports an assignment to backbone NH-vibrations.

We now turn to chiral-specific VSFG-spectra. By performing the SFG-experiment with a polarization combination that specifically probes elements of the non-linear susceptibility tensor $\chi^{(2)}_{IJK}$ with $I \neq J \neq K$ such as $\chi^{(2)}_{XYZ}$, we can probe the chiral molecules without any contribution from achiral molecules [22–24, 160–162, 173, 181]. If the plane of incidence of the IR- and VIS-beams is spanned by the X- and Z-axis of the laboratory coordinate frame, the polarization combination psp (p-polarized SFG, s-polarized VIS, p-polarized IR) will probe the chiral-specific $\chi^{(2)}_{ZYX}$-element. For a helical peptide, the chirality results from the handedness of the helix, which is right-handed for (L)-AFP1 and left-handed for (D)-AFP1. The NH-stretch vibrations of the peptide backbone

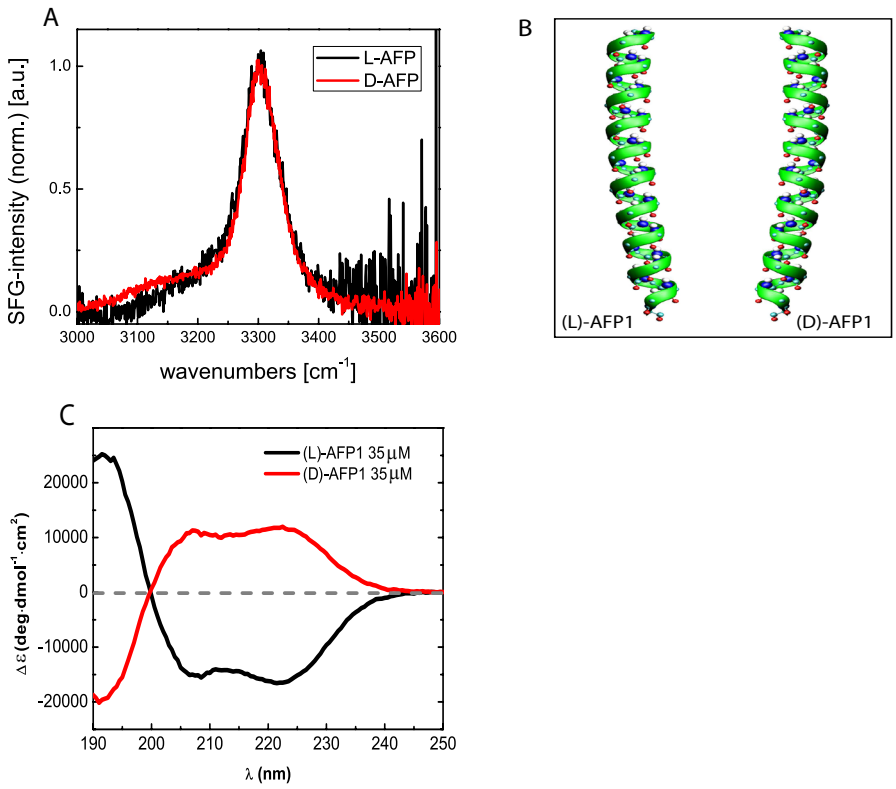

FIGURE 8.2. (A) Chiral SFG-spectra of L-type and D-type AFP1 obtained under psp-polarization settings. The sharp resonance at 3300 cm^{-1} originates from the NH-vibration of the peptide backbone [161]. (B) Structure of AFP synthesized from L- and D-amino acids; the structure of (D)-AFP1 has been generated by a mirror-image transformation of the structure of (L)-AFP1 published in [180](Protein Data Bank identifier 1WFA). (C) Near UV-circular dichroism spectra obtained from solutions of (L)- and (D)-AFP1 at 15 °, respectively. The CD-spectra exhibit the characteristic features of an α-helix, showing extrema in the molar ellipticity at 207 and 222 nm. The opposite sign of the CD-spectra confirms that (L)- and (D)-AFP1 indeed form helices with opposite handedness and are enantiomeric to each other.

report on this chirality [161, 173].

The spectra of Figure 8.2A are measured using psp-polarization conditions. The broad signal from the OH-stretch vibration of water molecules observed in Figure 8.1B is completely absent from the psp SFG spectrum, and only the sharp NH-feature of the peptide backbone is observed. Both the resonance frequency and the width of the peak are in good agreement with the values that were recently reported for the NH-stretch vibration of a number of other α-helical peptides and proteins [161].

The intensity-spectra in Figure 8.2A only demonstrate the presence of chi-

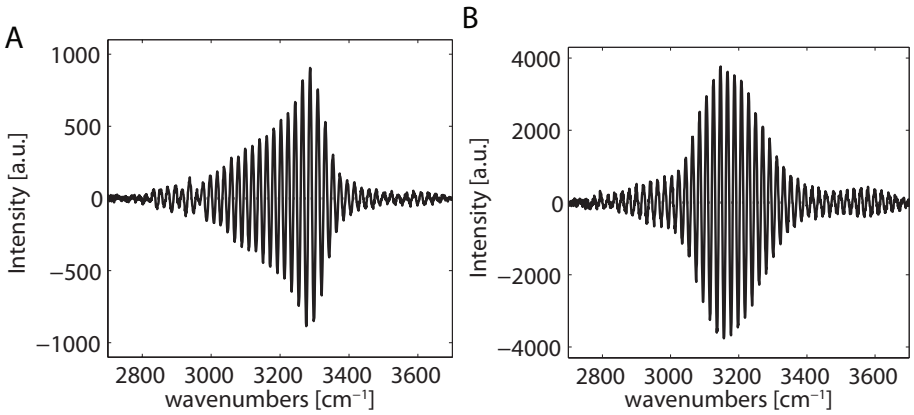

FIGURE 8.3. (A) Spectral interferogram of L-type AFP1 protein obtained by Fourier filtering of the spectral interference signal measured in psp configuration. (B) Spectral interferogram of the quartz surface obtained by replacing the sample with a quartz crystal.

ral molecules at the surface, but do not provide information on their absolute configuration, i.e. their handedness. The $\chi^{(2)}$-elements, that are probed under psp-polarization, change sign between enantiomers [22–24,158,171,173]. Hence, the nature of the enantiomer can be determined by measuring the phase of $\chi^{(2)}$, which requires heterodyne detection of the SFG light. We perform heterodyne-detected SFG experiments using the setup that is schematically depicted in Figure 3.3. The IR and visible beams are first both sent on a gold mirror which leads to the generation of broadband light at the sum-frequency (local oscillator, LO). Subsequently, the three resulting beams (IR, VIS and SFG) are sent together onto the sample where additional SFG light is generated at the aqueous surface. The local oscillator SFG light is delayed by Δt by sending this beam through a tilted fused silica plate. The SFG light generated at the gold mirror and at the sample co-propagate to the spectrograph and are detected by the CCD camera. The detected intensity of the heterodyne-detected SFG (HD-SFG) signal is given by Eq. (3.3). The cross-term $E_{sample}E^*_{LO}e^{-i\omega\Delta t}$ contains the electric field of the SFG-signal originating from the sample and is directly proportional to the complex $\chi^{(2)}$. The detected spectral interferogram is Fourier filtered to remove the $|E_{LO}(\omega)|^2$ and $|E_{sample}(\omega)|^2$ contributions and back transformed to yield an interferogram as shown in Figure 8.3A.

To determine the absolute phase of the SFG light generated by the proteins at the water-air interface, we compare the interferogram resulting from the heterodyne-detected SFG experiment of the sample with an interferogram measured for a sample with a well-known phase. To this purpose, we replace the sample by a quartz crystal that we orient in such a way that its bulk $\chi^{(2)}$ equals zero. For quartz the sum-frequency generation process is non-resonant, meaning that $\chi^{(2)}$ is real and frequency independent. Hence, the real and imaginary

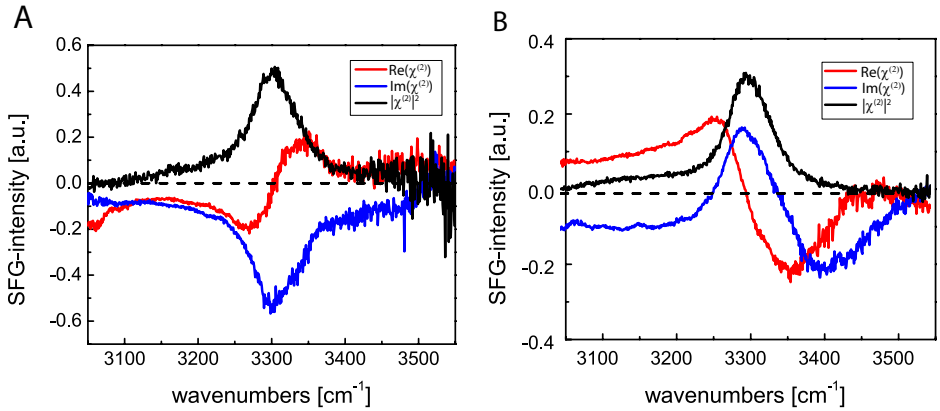

FIGURE 8.4. (A) Real and imaginary $\chi^{(2)}$ measured for L-type AFP1. (B) As (A) but for D-type AFP1. The intensity VSFG-spectra (proportional to $|\chi^{(2)}|^2$) of (L)- and (D)-AFP1 are shown in black for comparison.

$\chi^{(2)}$ of the AFP molecules at the water-air interface can be obtained from the ratio of the spectral interferogram measured for the surface of the aqueous AFP-solution (Figure 8.3A) and the interferogram measured for the quartz surface (Figure 8.3B) directly yields the values of according to Eq. (3.4).

$$\chi^{(2)}_{sample}(\omega) = \chi^{(2)}_{quartz}(\omega)\frac{E_{sample}(\omega)E^*_{LO}(\omega)e^{-i\omega\Delta t}}{E_{quartz}(\omega)E^*_{LO}(\omega)e^{-i\omega\Delta t}} = \chi^{(2)}_{quartz}(\omega)\frac{E_{sample}(\omega)}{E_{quartz}(\omega)} \quad (8.2)$$

In Figure 8.4, we plot the real and imaginary $\chi^{(2)}$ of L-and D-type AFP1 in the spectral region of the NH-stretch vibration obtained under psp-polarization settings and calculated according to Eq. (8.2). The opposite phase of the backbone NH-vibration resulting from the different signs of $\chi^{(2)}_{chiral}$ for right-handed (L-AFP1) and left-handed (D-AFP1) α-helical peptides is clearly resolved. This is most clearly seen in the absorptive imaginary part of $\chi^{(2)}$ that shows a sign change between (L)-AFP1 and (D)-AFP1. The dispersive real parts of $\chi^{(2)}_{chiral}$ reflect the same trend, with $\mathrm{Re}(\chi^{(2)}_{chiral})$ of (L)-AFP1 being negative at $\omega < \omega_0$, exhibiting a zero-crossing at ω_0 and becoming positive $\omega > \omega_0$. For (D)-AFP1 the opposite trend is observed, which is fully consistent with the opposite sign of the imaginary parts of $\chi^{(2)}_{chiral}$. The observed frequency dependence of the real and imaginary parts of $\chi^{(2)}_{chiral}$ confirms that the psp SFG signal originates from AFP molecules located at the surface. In case these signals would have resulted from bulk AFP molecules, the detected $\chi^{(2)}_{chiral}$ would have been phase shifted by $\pi/2$ [182,183]. Then the imaginary part of $\chi^{(2)}_{chiral}$ would have shown a dispersive shape, i.e. a sign change at the resonance frequency of 3350 cm^{-1},

and the real part would have been absorptive.
The above results demonstrate that the heterodyne-detected chiral SFG method allows for the determination of the absolute configuration of chiral molecules at interfaces. Due to the low sample amount that is required and short data integration times (<10 minutes), the experimental approach outlined here is perfectly suited to study (bio)chemical transformations at interfaces, offering unique insight in structural and conformational rearrangements of interfacial macromolecules. This method may find many applications, especially in fields where stereoselective (bio)chemical processes at interfaces play an important role. Examples are the assembly of superhelical protein complexes such as SNARE-complexes during membrane fusion events [184], the enantiospecific interaction between nucleobases and amino acids at surfaces [185] and the formation of two-dimensional chiral domains upon adsorption of helicenes onto metal surfaces [186].

8.4 CONCLUSIONS

We demonstrate heterodyne-detected chiral vibrational sum-frequency generation (VSFG) of an interfacial layer of biomolecules. By interfering the SFG light generated at the surface with the light of a local oscillator, and by comparing the resulting interferogram with that of a sample for which the phase of the SFG light is known, we determine the real and imaginary part of the second-order susceptibility $\chi^{(2)}$, and we demonstrate that the signal originates from molecules at the surface. This $\chi^{(2)}$ directly reflects the absolute configuration of chiral molecules. We show that the method allows for the distinction between surface bound type I antifreeze peptides with left- and right-handed helices. Probing the absolute configuration of chiral molecules at interfaces is of great value in understanding the adsorption affinity of proteins at interfaces and their associated structural and conformational changes.

8.5 APPENDIX A: DETERMINATION OF THE PHASE OF E_{SFG}

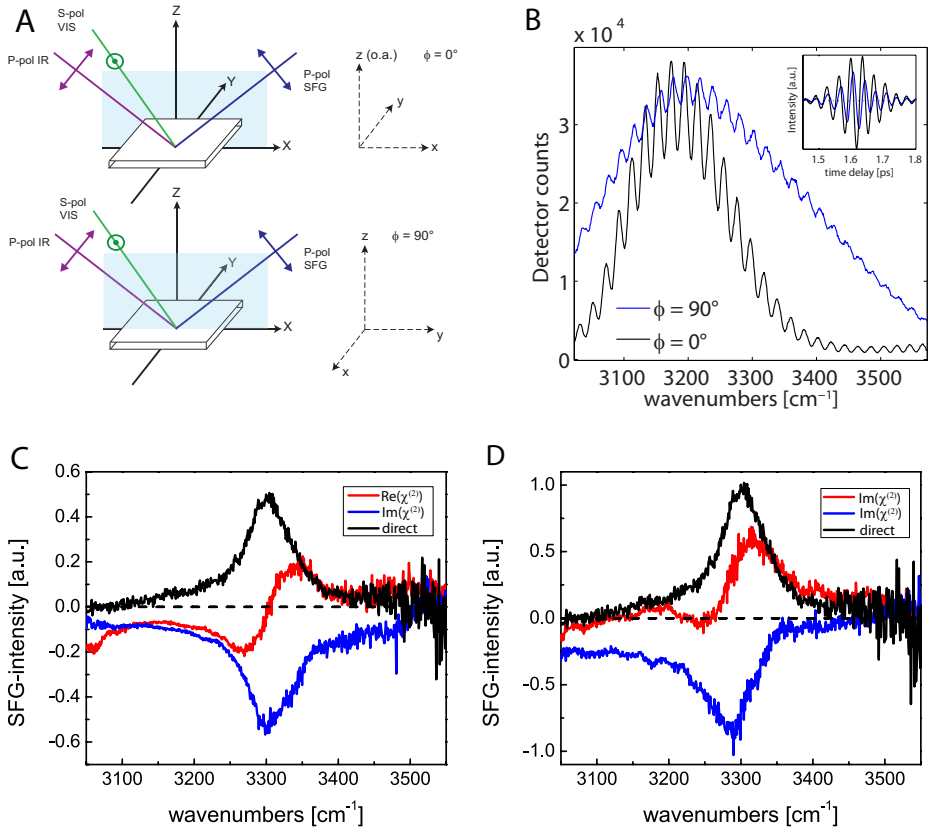

FIGURE 8.5. (A) Comparison of the orientations of the quartz-crystal used for referencing in psp-polarization. (X,Y,Z) and (x,y,z) denote the laboratory coordinate frame and the crystal coordinate frame, respectively. The optical axis (o.a.) of the z-cut crystal is oriented parallel to the surface normal (the Z-axis of the laboratory frame). ϕ denotes the angle between the X-axis and the x-axis. The $\phi = 0°$-orientation is also used in the experiments under ssp-polarization. (B) The spectral interferograms obtained for $\phi = 90°$ and $\phi = 0°$ under psp-polarization with 7 sec. and 55 sec. of integration time, respectively. The signal for $\phi = 90°$ has been scaled down by a factor of 0.65 for better comparison. The inset shows the corresponding time-domain data obtained by an inverse Fourier transformation of the spectral interferograms. (C) The complex phase-resolved chiral SFG-spectrum of (L)-AFP1 obtained using Eq. (8.2) and the quartz-crystal at $\phi = 0°$-orientation. (D) Same as (C) but using Eq. (8.3) and the quartz-crystal at $\phi = 90°$-orientation.

Since for a solution of chiral molecules the SFG-spectrum obtained under psp-polarization can in principle originate both from an interface and from the bulk of the isotropic solution [22, 24], we use the phase of the SFG-spectrum relative to the SFG-spectrum from quartz E_{quartz} to determine the origin of the sample-SFG (interface or bulk). The efficiency of the SFG-process is determined by the effective nonlinearity d_{eff}, and in quartz its dependence on rotation over the surface normal (the z-axis of the crystal) is given by $d_{eff} \propto d_{xxx}\cos(3\phi)$ in ssp and $d_{eff} \propto d_{xxx}\sin(3\phi)$ in psp [187, 188], where ϕ is the angle between the X-axis of the laboratory frame and the x-axis of the crystal frame as shown in Figure 8.5A. We can verify this by comparing the spectral interferograms obtained from quartz in two different orientations, $\phi = 0°$ and $\phi = 90°$. As expected, the signal obtained for $\phi = 0°$ is much smaller (about one order of magnitude) than for $\phi = 90°$. We furthermore note that the fringe patterns in the two interferograms in Figure 8.5B are exactly $\pi/2$ phase-shifted with respect two each other. This can also be clearly observed in the time-domain signals in the inset of Figure 8.5B obtained from an inverse Fourier transformation of the interferogram. These observations confirm that the quartz signal obtained for a crystal orientation of $\phi = 0°$ under psp-polarization results from the interface between quartz and air and not from the bulk. The real and imaginary part of $\chi^{(2)}_{chiral}$ of the aqueous interface are then obtained from Eq. (8.2). This procedure has been applied to Figure 8.4. An alternative approach is to rotate the quartz crystal by $\phi = 90°$ and to compare the spectrogram measured for the AFP solution with that of bulk quartz. In this case the real and imaginary part of $\chi^{(2)}_{chiral}$ are determined by:

$$\chi^{(2)}_{sample}(\omega) = \chi^{(2)}_{quartz}(\omega)\frac{E_{sample}(\omega)}{iE_{quartz}(\omega)} \tag{8.3}$$

The factor of i in the denominator of this equation is introduced because the sum-frequency field generated in the bulk of the non-centrosymmetric quartz crystal has a phase shift of $\pi/2$ relative to the sum-frequency electric field generated at the surface [182, 183].

The very efficient SFG-generation from quartz at $\phi = 90°$-orientation causes the CCD-camera to become saturated after a few seconds of signal integration, thus posing an upper limit for the integration time of the much weaker LO-signal. It is possible to show that the noise in the cross-terms of Eq. (3.3) is dominated by the shot-noise from the SFG-field with the higher intensity [170]. If E_{LO} is smaller than than E_{quartz} by a factor of f with $f \ll 1$, then it can easily be shown that the signal-to-noise ratio is effectively reduced by a factor of f compared to the usual situation where the LO is large compared to the signal it interferes with [170]. Thus referencing the peptide-SFG signal to the quartz-SFG signal obtained at $\phi = 90°$ leads to an elevated noise level in the final phase-resolved SFG-spectrum of the peptide sample. The effect can be seen when comparing Figure 8.5D to 8.5C. Measuring the reference spectrum from quartz for $\phi = 0°$ circumvents this problem since in this case E_{LO} and E_{quartz} are of comparable magnitude, thus avoiding the introduction of additional noise sources into the

final phase-resolved spectrum.

8.6 APPENDIX B: CHARACTERIZATION OF (L)- AND (D)-AFP1

8.6.1 UV-CIRCULAR DICHROISM

To determine the thermodynamic properties of (L)- and (D)-AFP1, the unfolding of the peptides was studied using a circular dichroism temperature wavelength scan from 1 to 85 °C (Figure 8.6). All samples were measured in a quartz cuvette with a path length of 0.2 cm in 5 mM phosphate buffer on a Jasco J-815 spectropolarimeter, where the sensitivity, time constant and scan-rate were chosen appropriately. Temperature was controlled by a PFD-425S/15 Peltier-type temperature controller. To derive the thermodynamic parameters from the temperature dependent CD measurements, we used a simple two-state model, where the peptide is either in a fully folded (F) or a fully (reversible)

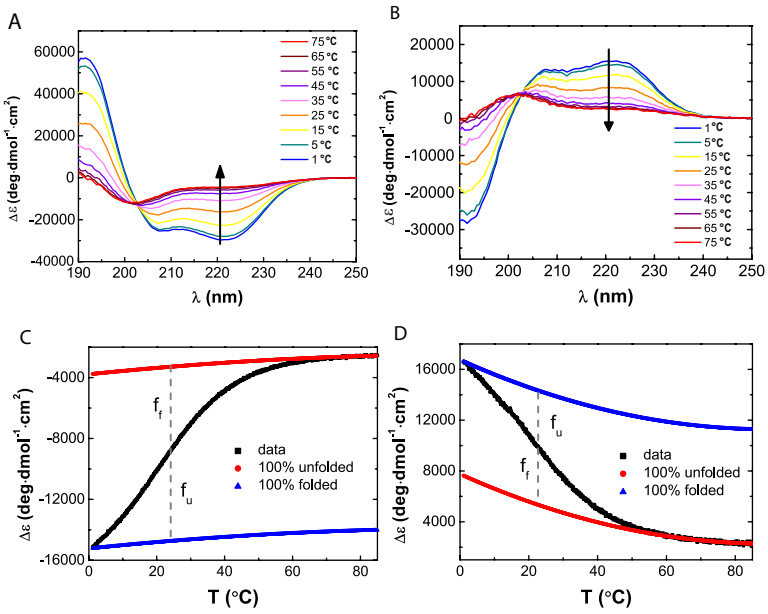

FIGURE 8.6. Temperature-dependent CD-spectra of (A) (L)-AFP1 and (B) (D)-AFP1. (C,D) Circular dichroism temperature-wavelength scan at 222 nm of (L)-AFP1 and (D)-AFP1. Black symbols are data points, red and blue lines denote a fit for the 100% unfolded state (f_u) and for the 100% folded state (f_f), respectively. The latter were obtained from a quadratic fit to the data points outside the transition region. The melting temperature T_m corresponding to $f_u = f_f$ is 23°C for both peptides.

unfolded (U) state, given by

$$F \leftrightarrows U, \qquad K_D = \frac{U}{F} \tag{8.4}$$

The fraction folded (f_f) and unfolded (f_u) peptide is then

$$f_f = \frac{\alpha}{\alpha + \beta}, \qquad f_u = \frac{\beta}{\alpha + \beta} \tag{8.5}$$

where α and β is the helicity calculated as the difference between the fitted lines for 100% (un)folded and experimental data points. These equations can be inserted into Eq. (8.4), leading to $K_D = f_u/f_f$. A Van't Hoff plot of $\ln(K_D)$ vs $1/T$ [K^{-1}] can be used to derive the thermodynamic parameters. Equimolar amounts of folded and unfolded peptide ($f_f = f_u$) give $K_D = 1$ and $\ln(K_D) = 0$, from which the denaturation temperature T_m can be derived from the intercept with the horizontal axis, which gives an equal denaturation temperature $T_m = 23$ °C for (L)- and (D)-AFP1, which agrees well with literature values [189].

8.6.2 FREEZING HYSTERESIS ACTIVITY OF (L)- AND (D)-AFP1

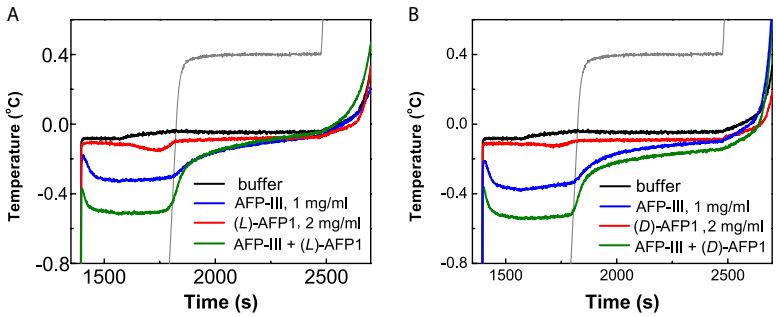

FIGURE 8.7. Activity of (A) (L)-AFP1 and (B) (D)-AFP1 as determined by thermal hysteresis measurements. While both (L)- and (D)-AFP1 alone exhibit very little activity, both peptides are able to potentiate the observed antifreeze-activity of AFP-III. This agrees with the observations in Ref. [190] from ice-crystal growth measurements.

The thermal hysteresis activity of the synthesized peptides was measured by sonocrystallization of which the methods and experimental setup are described elsewhere [191]. Sonocrystallization is a method to determine the lowering of the non-equilibrium freezing point by antifreeze proteins. Samples are cooled to -6 °C after which ice-crystallization is initiated by the application of a short ultrasound pulse, resulting in the release of latent heat. This raises the sample temperature until it stabilizes at the non-equilibrium freezing point of the

solution. Hereafter the temperature is slowly raised to determine the melting point of the solution. As expected, type III antifreeze protein (AFP-III) shows a stable freezing plateau as seen in Figure 8.7. Surprisingly, type I AFP does not form a stable freezing plateau, however the addition of AFP1 to AFP-III enhances the non-colligative freezing point depression. The effects observed in the sonocrystallization experiments are virtually indistinguishable for (L)-AFP1 and (D)-AFP1.

The CD-spectroscopic characterization and freezing hysteresis activity tests have been performed at the Laboratory of Macromolecular and Organic Chemistry of the Technical University Eindhoven by Luuk L.C. Olijve under the supervision of Dr. Ilja K. Voets.

Bibliography

[1] D. Arnlund *et al.* Visualizing a protein quake with time-resolved X-ray scattering at a free-electron laser. *Nat. Meth.*, 11(9):923–926, 2014.

[2] A. G. Palmer. Enzyme dynamics from NMR spectroscopy. *Acc. Chem. Res.*, 48(2):457–465, 2015.

[3] S. Woutersen, Y. Mu, G. Stock, and P. Hamm. Subpicosecond conformational dynamics of small peptides probed by two-dimensional vibrational spectroscopy. *Proc. Nat. Sci. U.S.A*, 98(20):11254–11258, 2001.

[4] S. Woutersen, U. Emmerichs, and H. J. Bakker. Femtosecond mid-IR pump-probe spectroscopy of liquid water: Evidence for a two-component structure. *Science*, 278(5338):658–660, 1997.

[5] C. J. Fecko, J. D. Eaves, J. J. Loparo, A. Tokmakoff, and P. L. Geissler. Ultrafast hydrogen-bond dynamics in the infrared spectroscopy of water. *Science*, 301(5640):1698–1702, 2003.

[6] A. W. Omta, M. F. Kropman, S. Woutersen, and H. J. Bakker. Negligible effect of ions on the hydrogen-bond structure in liquid water. *Science*, 301(5631):347–349, 2003.

[7] J. B. Asbury, T. Steinel, C. Stromberg, K. J. Gaffney, I. R. Piletic, A. Goun, and M. D. Fayer. Hydrogen bond dynamics probed with ultrafast infrared heterodyne-detected multidimensional vibrational stimulated echoes. *Phys. Rev. Lett.*, 91:237402, 2003.

[8] J. B. Asbury, T. Steinel, K. Kwak, S. A. Corcelli, C. P. Lawrence, J. L. Skinner, and M. D. Fayer. Dynamics of water probed with vibrational echo correlation spectroscopy. *J. Chem. Phys.*, 121(24):12431–12446, 2004.

[9] J. B. Asbury, T. Steinel, C. Stromberg, S. A. Corcelli, C. P. Lawrence, J. L. Skinner, and M. D. Fayer. Water dynamics: Vibrational echo correlation spectroscopy and comparison to molecular dynamics simulations. *J. Phys. Chem. A*, 108(7):1107–1119, 2004.

[10] J. D. Eaves, J. J. Loparo, C. J. Fecko, S. T. Roberts, A. Tokmakoff, and P. L. Geissler. Hydrogen bonds in liquid water are broken only fleetingly. *Proc. Nat. Sci. U.S.A*, 102(37):13019–13022, 2005.

[11] S. Park and M. D. Fayer. Hydrogen bond dynamics in aqueous NaBr solutions. *Proc. Nat. Sci. U.S.A*, 104(43):16731–16738, 2007.

[12] D. E. Moilanen, E. E. Fenn, D. Wong, and M. D. Fayer. Water dynamics at the interface in AOT reverse micelles. *J. Phys. Chem. B*, 113(25):8560–8568, 2009.

[13] M. Ji, M. Odelius, and K. J. Gaffney. Large angular jump mechanism observed for hydrogen bond exchange in aqueous perchlorate solution. *Science*, 328(5981):1003–1005, 2010.

[14] K. J. Tielrooij, N. Garcia-Araez, M. Bonn, and H. J. Bakker. Cooperativity in ion hydration. *Science*, 328(5981):1006–1009, 2010.

[15] P. Mukherjee, I. Kass, I. T. Arkin, and M. T. Zanni. Picosecond dynamics of a membrane protein revealed by 2D IR. *Proc. Nat. Sci. U.S.A*, 103(10):3528–3533, 2006.

[16] A. M. Woys, Y.-S. Lin, A. S. Reddy, W. Xiong, J. J. de Pablo, J. L. Skinner, and M. T. Zanni. 2D IR line shapes probe ovispirin peptide conformation and depth in lipid bilayers. *J. Am. Chem. Soc.*, 132(8):2832–2838, 2010.

[17] L. Pauling, R. B. Corey, and H. R. Branson. The structure of proteins: Two hydrogen-bonded helical configurations of the polypeptide chain. *Proc. Nat. Sci. U.S.A*, 37(4):205–211, 1951.

[18] H. Urata, E. Ogura, K. Shinohara, Y. Ueda, and M. Akagi. Synthesis and properties of mirror-image DNA. *Nucleic Acids Res.*, 20(13):3325–3332, 1992.

[19] Y. Mitsui, R. Langridge, B. E. Shortle, C. R. Cantor, R. C. Grant, Ma. Kodama, and R. D. Wells. Physical and enzymatic studies on poly d(I-C)-poly d(I-C), an unusual double-helical DNA. *Nature*, 228(5277):1166–1169, 1970.

[20] Peerdeman A.F. Bijvoet, J. M. and A.J. Van Bommel. Determination of the absolute configuration of optically active compounds by means of X-rays. *Nature*, 168:271–272, 1951.

[21] X. Huang, K. Nakanishi, and N. Berova. Porphyrins and metalloporphyrins: Versatile circular dichroic reporter groups for structural studies. *Chirality*, 12(4):237–255, 2000.

[22] M. A. Belkin, T. A. Kulakov, K.-H. Ernst, L. Yan, and Y. R. Shen. Sum-frequency vibrational spectroscopy on chiral liquids: A novel technique to probe molecular chirality. *Phys. Rev. Lett.*, 85:4474–4477, 2000.

[23] M. A. Belkin, S. H. Han, X. Wei, and Y. R. Shen. Sum-frequency generation in chiral liquids near electronic resonance. *Phys. Rev. Lett.*, 87:113001, 2001.

[24] M. A. Belkin and Y. R. Shen. Doubly resonant IR-UV sum-frequency vibrational spectroscopy on molecular chirality. *Phys. Rev. Lett.*, 91:213907, 2003.

[25] H. Rhee, Y.-G. June, J.-S. Lee, K.-K. Lee, J.-H. Ha, Z. H. Kim, S.-J. Jeon, and M. Cho. Femtosecond characterization of vibrational optical activity of chiral molecules. *Nature*, 458(7236):310–313, 2009.

[26] D. Patterson and J. M. Doyle. Sensitive chiral analysis via microwave three-wave mixing. *Phys. Rev. Lett.*, 111:023008, 2013.

[27] D. Patterson, M. Schnell, and J. M. Doyle. Enantiomer-specific detection of chiral molecules via microwave spectroscopy. *Nature*, 497(7450):475–477, 2013.

[28] S. R. Domingos, H. J. Sanders, F. Hartl, W.J. Buma, and S. Woutersen. Switchable amplification of vibrational circular dichroism as a probe of local chiral structure. *Angew. Chem. Int. Ed. Engl.*, 126(51):14266–14269, 2014.

[29] Y. R. Shen. The Principles of Nonlinear Optics. Wiley Interscience, 1984.

[30] P. Hamm, M. Lim, and R. M. Hochstrasser. Structure of the amide I band of peptides measured by femtosecond nonlinear-infrared spectroscopy. *J. Phys. Chem. B*, 102(31):6123–6138, 1998.

[31] R. W. Boyd and S. Mukamel. Origin of spectral holes in pump-probe studies of homogeneously broadened lines. *Phys. Rev. A*, 29:1973–1983, 1984.

[32] S. Woutersen and H. J. Bakker. Coherent coupling in frequency-resolved pump-probe spectroscopy. *J. Opt. Soc. Am. B*, 17(5):827–832, May 2000.

[33] K. Wynne and R.M. Hochstrasser. Coherence effects in the anisotropy of optical experiments. *Chem. Phys.*, 171(1-2):179 – 188, 1993.

[34] P. Hamm. Coherent effects in femtosecond infrared spectroscopy. *Chem. Phys.*, 200(3):415–429, 1995.

[35] P. Hamm and M. Zanni. Concepts and Methods of 2D Infrared Spectroscopy. Cambridge University Press, 2011.

[36] S. Mukamel. Principles of Nonlinear Optical Spectroscopy. Oxford University Press, 1995.

[37] P. Hamm, M. Lim, W. F. DeGrado, and R. M. Hochstrasser. The two-dimensional IR nonlinear spectroscopy of a cyclic penta-peptide in relation to its three-dimensional structure. *Proc. Nat. Sci. U.S.A*, 96(5):2036–2041, 1999.

[38] Michael D Fayer. Ultrafast infrared and Raman spectroscopy, volume 26. CRC Press, 2001.

[39] A. Moran and S. Mukamel. The origin of vibrational mode couplings in various secondary structural motifs of polypeptides. *Proc. Nat. Sci. U.S.A*, 101(2):506–510, 2004.

[40] R. D. Gorbunov, D. S. Kosov, and G. Stock. Ab initio-based exciton model of amide i vibrations in peptides: Definition, conformational dependence, and transferability. *J. Chem. Phys.*, 122(22):224904, 2005.

[41] R. D. Waldron. Infrared spectra of HDO in water and ionic solutions. *J. Chem. Phys.*, 26(4):809–814, 1957.

[42] W. M. Cox and J. H. Wolfenden. The viscosity of strong electrolytes measured by a differential method. *Proc. R. Soc. London, A*, 145(855):475–488, 1934.

[43] Y. Marcus. Effect of ions on the structure of water: Structure making and breaking. *Chem. Rev.*, 109(3):1346–1370, 2009.

[44] M. D. Fayer, D. E. Moilanen, D. Wong, D. E. Rosenfeld, E. E. Fenn, and S. Park. Water dynamics in salt solutions studied with ultrafast two-dimensional infrared (2D IR) vibrational echo spectroscopy. *Acc. Chem. Res.*, 42(9):1210–1219, 2009.

[45] M. F. Kropman and H. J. Bakker. Dynamics of water molecules in aqueous solvation shells. *Science*, 291(5511):2118–2120, 2001.

[46] M. F. Kropman and H. J. Bakker. Effect of ions on the vibrational relaxation of liquid water. *J. Am. Chem. Soc.*, 126(29):9135–9141, 2004.

[47] M. F. Kropman and H. J. Bakker. Femtosecond mid-infrared spectroscopy of aqueous solvation shells. *J. Chem. Phys.*, 115(19):8942–8948, 2001.

[48] M. F. Kropman, H.-K. Nienhuys, and H. J. Bakker. Real-time measurement of the orientational dynamics of aqueous solvation shells in bulk liquid water. *Phys. Rev. Lett.*, 88:077601, 2002.

[49] R. L. A. Timmer and H. J. Bakker. Hydrogen bond fluctuations of the hydration shell of the bromide anion. *J. Phys. Chem. A*, 113(21):6104–6110, 2009.

[50] D. Laage and J. T. Hynes. Reorientional dynamics of water molecules in anionic hydration shells. *Proc. Nat. Sci. U.S.A*, 104(27):11167–11172, 2007.

[51] A. M. Dokter, S. Woutersen, and H. J. Bakker. Inhomogeneous dynamics in confined water nanodroplets. *Proc. Nat. Sci. U.S.A*, 103(42):15355–15358, 2006.

[52] I..R. Piletic, D. E. Moilanen, D. B. Spry, N. E. Levinger, and M. D. Fayer. Testing the core/shell model of nanoconfined water in reverse micelles using linear and nonlinear IR spectroscopy. *J. Phys. Chem. A*, 110(15):4985–4999, 2006.

[53] D. Laage and J. T. Hynes. A molecular jump mechanism of water reorientation. *Science*, 311(5762):832–835, 2006.

[54] C. J. Fecko, J. J. Loparo, S. T. Roberts, and A. Tokmakoff. Local hydrogen bonding dynamics and collective reorganization in water: Ultrafast infrared spectroscopy of HOD/D_2O. *J. Chem. Phys.*, 122(5):054506, 2005.

[55] J. Stenger, D. Madsen, P. Hamm, E. T. J. Nibbering, and T. Elsaesser. A photon echo peak shift study of liquid water. *J. Phys. Chem. A*, 106(10):2341–2350, 2002.

[56] T. Steinel, J. B. Asbury, J. Zheng, and M. D. Fayer. Watching hydrogen bonds break: A transient absorption study of water. *J. Phys. Chem. A*, 108(50):10957–10964, 2004.

[57] S. Woutersen and H. J. Bakker. Resonant intermolecular transfer of vibrational energy in liquid water. *Nature*, 402(6761):507–509, 1999.

[58] M. L. Cowan, B. D. Bruner, N. Huse, J. R. Dwyer, B. Chugh, E. T. J. Nibbering, T. Elsaesser, and R. J. D. Miller. Ultrafast memory loss and energy redistribution in the hydrogen bond network of liquid H_2O. *Nature*, 434(7030):199–202, 2005.

[59] L. Piatkowski, K. B. Eisenthal, and H. J. Bakker. Ultrafast intermolecular energy transfer in heavy water. *Phys. Chem. Chem. Phys.*, 11(40):9033–9038, 2009.

[60] P. A. Bergstroem, J. Lindgren, and O. Kristiansson. An IR study of the hydration of perchlorate, nitrate, iodide, bromide, chloride and sulfate anions in aqueous solution. *J. Chem. Phys.*, 95(22):8575–8580, 1991.

[61] Y. L. A. Rezus and H. J. Bakker. Orientational dynamics of isotopically diluted H_2O and D_2O. *J. Chem. Phys.*, 125(14):144512, 2006.

[62] S. Woutersen, U. Emmerichs, H.-K. Nienhuys, and H. J. Bakker. Anomalous temperature dependence of vibrational lifetimes in water and ice. *Phys. Rev. Lett.*, 81(5):1106–1109, 1998.

[63] A. J. Lock and H. J. Bakker. Temperature dependence of vibrational relaxation in liquid H_2O. *J. Chem. Phys.*, 117(4):1708–1713, 2002.

[64] J. C. Duplan, L. Mahi, and J. L. Brunet. NMR determination of the equilibrium constant for the liquid H_2O/D_2O mixture. *Chem. Phys. Lett.*, 413(4-6):400–403, 2005.

[65] S. Ashihara, N. Huse, A. Espagne, E. T. J. Nibbering, and T. Elsaesser. Ultrafast structural dynamics of water induced by dissipation of vibrational energy. *Phys. Rev. Lett.*, 111(5):743–746, 2007.

[66] M. Yang, F. Li, and J. L. Skinner. Vibrational energy transfer and anisotropy decay in liquid water: Is the Förster model valid? *J. Chem. Phys.*, 135(16):164505, 2011.

[67] Th Förster. Zwischenmolekulare Energiewanderung und Fluoreszenz. *Annalen der Physik*, 437(1-2):55–75, 1948.

[68] J.A. Riddick, W. B. Bunger, and T. K. Sakano. Organic Solvents: Physical Properties and Methods of Purification. John Wiley and Sons, New York, 1986.

[69] NIST chemistry webbook.

[70] J. M. G. Cowie and P. M. Toporowski. Association in the binary liquid system dimethyl sulphoxide - water. *Can. J. Chem.*, 39(11):2240–2243, 1961.

[71] D. O. Hanson and M. Van Winkle. Relation of binary heats of mixing and distribution of ketone between phases in some ketone-water-solvent ternaries. *J. Chem. Eng. Data*, 5(1):30–34, 1960.

[72] S. A. Schichman and R. L. Amey. Viscosity and local liquid structure in dimethyl sulfoxide-water mixtures. *J. Phys. Chem.*, 75(1):98–102, 1971.

[73] J. Padova. Ion-solvent interaction in mixed solvents. II. The viscosity of electrolytes in mixed solvents. *J. Chem. Phys.*, 38(11):2635–2640, 1963.

[74] U. Kaatze, R. Pottel, and M. Schaefer. Dielectric spectrum of dimethyl sulfoxide/water mixtures as a function of composition. *J. Phys. Chem.*, 93(14):5623–5627, 1989.

[75] A.C. Kumbharkhane, S.N. Helambe, M.P. Lokhande, S. Doraiswamy, and S.C. Mehrotra. Structural study of aqueous solutions of tetrahydrofuran and acetone mixtures using dielectric relaxation technique. *Pramana*, 46(2):91–98, 1996.

[76] K. J. Packer and D. J. Tomlinson. Nuclear spin relaxation and self-diffusion in the binary system, dimethylsulphoxide (DMSO) + water. *Trans. Faraday Soc.*, 67:1302–1314, 1971.

[77] D. W. McCall and D. C. Douglass. Diffusion in binary solutions. *J. Phys. Chem.*, 71(4):987–997, 1967.

[78] J. E. Lovelock and M. W. H. Bishop. Prevention of freezing damage to living cells by dimethyl sulphoxide. *Nature*, 183(4672):1394–1395, 1959.

[79] I.J. Bickis, K. Kazaks, J.J. Finn, and I.W.D. Henderson. Permeation kinetics of glycerol and dimethyl sulfoxide in novikoff hepatoma ascites cells. *Cryobiology*, 4(1):1–10, 1967.

[80] M. J. Ashwood-Smith. Preservation of mouse bone marrow at -79° C. with dimethyl sulphoxide. *Nature*, 190(4782):1204–1205, 1961.

[81] D.E. Pegg. Freezing of bone marrow for clinical use. *Cryobiology*, 1(1):64–71, 1964.

[82] M. J. Ashwood-Smith. Radioprotective and cryoprotective properties of dimethyl sulfoxide in cellular systems. *Annals of the New York Academy of Sciences*, 141(1):45–62, 1967.

[83] J.S. Vicente and F. Garcia-Ximenez. Osmotic and cryoprotective effects of a mixture of DMSO and ethylene glycol on rabbit morulae. *Theriogenology*, 42(7):1205–1215, 1994.

[84] J. L. Hanslick, K. Lau, K. K. Noguchi, J. W. Olney, C. F. Zorumski, S. Mennerick, and N. B. Farber. Dimethyl sulfoxide (DMSO) produces widespread apoptosis in the developing central nervous system. *Neurobiology of Disease*, 34(1):1–10, 2009.

[85] I. A. Borin and M. S. Skaf. Molecular association between water and dimethyl sulfoxide in solution: A molecular dynamics simulation study. *J. Chem. Phys.*, 110(13):6412–6420, 1999.

[86] A. Luzar and D. Chandler. Structure and hydrogen bond dynamics of water-dimethyl sulfoxide mixtures by computer simulations. *J. Chem. Phys.*, 98(10):8160–8173, 1993.

[87] I. I. Vaisman and M. L. Berkowitz. Local structural order and molecular associations in water-DMSO mixtures. molecular dynamics study. *J. Am. Chem. Soc.*, 114(20):7889–7896, 1992.

[88] A. K. Soper and A. Luzar. A neutron diffraction study of dimethyl sulphoxide-water mixtures. *J. Chem. Phys.*, 97(2):1320–1331, 1992.

[89] B. Kirchner and M. Reiher. The secret of dimethyl sulfoxide-water mixtures. A quantum chemical study of 1 DMSO-n water clusters. *J. Am. Chem. Soc.*, 124(21):6206–6215, 2002.

[90] D. B. Wong, K. P. Sokolowsky, M. I. El-Barghouthi, E. E. Fenn, C. H. Giammanco, A. L. Sturlaugson, and M. D. Fayer. Water dynamics in water/DMSO binary mixtures. *J. Phys. Chem. B*, 116(18):5479–5490, 2012.

[91] M. Ferrario, M. Haughney, I. R. McDonald, and M. L. Klein. Molecular-dynamics simulation of aqueous mixtures: Methanol, acetone, and ammonia. *J. Chem. Phys.*, 93(7):5156–5166, 1990.

[92] D. S. Venables and C. A. Schmuttenmaer. Spectroscopy and dynamics of mixtures of water with acetone, acetonitrile, and methanol. *J. Chem. Phys.*, 113(24):11222–11236, 2000.

[93] S. E. McLain, A. K. Soper, and A. Luzar. Investigations on the structure of dimethyl sulfoxide and acetone in aqueous solution. *J. Chem. Phys.*, 127(17):174515, 2007.

[94] J.-J. Max and C. Chapados. Infrared spectroscopy of acetone-water liquid mixtures. I. Factor analysis. *J. Chem. Phys.*, 119(11):5632–5643, 2003.

[95] J.-J. Max and C. Chapados. Infrared spectroscopy of acetone-water liquid mixtures. II. Molecular model. *J. Chem. Phys.*, 120(14):6625–6641, 2004.

[96] Y. L. A. Rezus and H. J. Bakker. On the orientational relaxation of HDO in liquid water. *J. Chem. Phys.*, 123(11):114502, 2005.

[97] Y. L. A. Rezus and H. J. Bakker. Observation of immobilized water molecules around hydrophobic groups. *Phys. Rev. Lett.*, 99:148301, 2007.

[98] Y.L.A. Rezus and H.J. Bakker. Femtosecond spectroscopic study of the solvation of amphiphilic molecules by water. *Chem. Phys.*, 350(1-3):87–93, 2008.

[99] A.V. Benedetti, M. Cilense, D.R. Vollet, and R.C. Montone. Thermodynamic properties of liquid mixtures. III. Acetone-water. *Thermochim. Acta*, 66(13):219 – 223, 1993.

[100] E. Von Goldammer and H. G. Hertz. Molecular motion and structure of aqueous mixtures with nonelectrolytes as studied by nuclear magnetic relaxation methods. *J. Phys. Chem.*, 74(21):3734–3755, 1970.

[101] A. Barth. Infrared spectroscopy of proteins. *Biochim. Biophys. Acta - Bioenergetics*, 1767(9):1073–1101, 2007.

[102] J. Bandekar and S. Krimm. Vibrational analysis of peptides, polypeptides, and proteins. VI. Assignment of β-turn modes in insulin and other proteins. *Biopolymers*, 19(1):31–36, 1980.

[103] H. Torii and M. Tasumi. Model calculations on the amide-I infrared bands of globular proteins. *J. Chem. Phys.*, 96(5):3379–3387, 1992.

[104] J. Manor, P. Mukherjee, Y.-S. Lin, H. Leonov, J. L. Skinner, M. T. Zanni, and I. T. Arkin. Gating mechanism of the influenza A M2 channel revealed by 1D and 2D IR spectroscopies. *Structure*, 17(2):247 – 254, 2009.

[105] N. Demirdöven, C. M. Cheatum, H. S. Chung, M. Khalil, J. Knoester, and A. Tokmakoff. Two-dimensional infrared spectroscopy of antiparallel β-sheet secondary structure. *J. Am. Chem. Soc.*, 126(25):7981–7990, 2004.

[106] A. W. Smith, J. Lessing, Z. Ganim, C. S. Peng, A. Tokmakoff, S. Roy, T. L. C. Jansen, and J. Knoester. Melting of a β-hairpin peptide using isotope-edited 2D IR spectroscopy and simulations. *J. Phys. Chem. B*, 114(34):10913–10924, 2010.

[107] J. Lessing, S. Roy, M. Reppert, M. Baer, D. Marx, T. La Cour Jansen, J. Knoester, and A. Tokmakoff. Identifying residual structure in intrinsically disordered systems: A 2D IR spectroscopic study of the *GVGXPGVG* peptide. *J. Am. Chem. Soc.*, 134(11):5032–5035, 2012.

[108] A. Ghosh, J. Qiu, W. F. DeGrado, and R. M. Hochstrasser. Tidal surge in the M2 proton channel, sensed by 2D IR spectroscopy. *Proc. Nat. Sci. U.S.A*, 108(15):6115–6120, 2011.

[109] A. Remorino, I. V. Korendovych, Y. Wu, W. F. DeGrado, and R. M. Hochstrasser. Residue-specific vibrational echoes yield 3D structures of a transmembrane helix dimer. *Science*, 332(6034):1206–1209, 2011.

[110] C. T. Middleton, L. E. Buchanan, E. B. Dunkelberger, and M. T. Zanni. Utilizing lifetimes to suppress random coil features in 2D IR spectra of peptides. *J. Phys. Chem. Lett.*, 2(18):2357–2361, 2011.

[111] Mu Y. Stock G. Woutersen, S. and P. Hamm. Hydrogen-bond lifetime measured by time-resolved 2D-IR spectroscopy: *N*-methylacetamide in methanol. *Chem. Phys.*, 266(2-3):137–147, 2001.

[112] V. Volkov and P. Hamm. A two-dimensional infrared study of localization, structure, and dynamics of a dipeptide in membrane environment. *Biophys. J.*, 87(6):4213–4225, 2004.

[113] Y. Yeh and R. E. Feeney. Antifreeze proteins: Structures and mechanisms of function. *Chem. Rev.*, 96(2):601–618, 1996.

[114] F. D. Sönnichsen, C. I. DeLuca, P. L. Davies, and B. D. Sykes. Refined solution structure of type III antifreeze protein: Hydrophobic groups may be involved in the energetics of the protein-ice interaction. *Structure*, 4(11):1325–1337, 1996.

[115] A. A. Antson, D. J. Smith, D. I. Roper, S. Lewis, Leo S.D. Caves, C. S. Verma, S. L. Buckley, P. J. Lillford, and R. E. Hubbard. Understanding the mechanism of ice binding by type *III* antifreeze proteins. *J. Mol. Bio.*, 305(4):875–889, 2001.

[116] A. G. Salvay, F. Gabel, B. Pucci, J. Santos, E. I. Howard, and C. Ebel. Structure and interactions of fish type III antifreeze protein in solution. *Biophys. J.*, 99(2):609–618, 2010.

[117] V. Cervetto, J. Helbing, and P. Bredenbeck, J.and Hamm. Double-resonance versus pulsed fourier transform two-dimensional infrared spectroscopy: An experimental and theoretical comparison. *J. Chem. Phys.*, 121(12):5935–5942, 2004.

[118] T. Miyazawa. Perturbation treatment of the characteristic vibrations of polypeptide chains in various configurations. *J. Chem. Phys.*, 32(6):1647–1652, 1960.

[119] T. la Cour Jansen and J. Knoester. Two-dimensional infrared population transfer spectroscopy for enhancing structural markers of proteins. *Biophys. J.*, 94(5):1818–1825, 2008.

[120] P. Hamm, M. Lim, W. F. DeGrado, and R. M. Hochstrasser. Stimulated photon echoes from amide I vibrations. *J. Phys. Chem. A*, 103(49):10049–10053, 1999.

[121] C. D. Waldburger, J. F. Schildbach, and R. T. Sauer. Are buried salt bridges important for protein stability and conformational specificity? *Nat. Struct. Bio.*, 2:122–128, 1995.

[122] H. Meuzelaar, M. Tros, A. Huerta-Viga, C. N. van Dijk, J. Vreede, and S. Woutersen. Solvent-exposed salt bridges influence the kinetics of α-helix folding and unfolding. *J. Phys. Chem. Lett.*, 5(5):900–904, 2014.

[123] R. J. Sension, B. Hudson, and P. R. Callis. Resonance raman studies of guanidinium and substituted guanidinium ions. *J. Phys. Chem.*, 94(10):4015–4025, 1990.

[124] D. Y. Vorobyev, C.-H. Kuo, J.-X. Chen, D. G. Kuroda, J. N. Scott, J. M. Vanderkooi, and R. M. Hochstrasser. Ultrafast vibrational spectroscopy of a degenerate mode of guanidinium chloride. *J. Phys. Chem. B*, 113(46):15382–15391, 2009.

[125] D. Yu. Vorobyev, C.-H. Kuo, D. G. Kuroda, J. N. Scott, J. M. Vanderkooi, and R. M. Hochstrasser. Water-induced relaxation of a degenerate vibration of guanidinium using 2D IR echo spectroscopy. *J. Phys. Chem. B*, 114(8):2944–2953, 2010.

[126] A. Ghosh, M. J. Tucker, and R. M. Hochstrasser. Identification of arginine residues in peptides by 2D-IR echo spectroscopy. *J. Phys. Chem. A*, 115(34):9731–9738, 2011.

[127] A. Huerta-Viga, S. R. Domingos, S. Amirjalayer, and S. Woutersen. A salt-bridge structure in solution revealed by 2D-IR spectroscopy. *Phys. Chem. Chem. Phys.*, 16:15784–15786, 2014.

[128] D. G. Kuroda, D. Y. Vorobyev, and R. M. Hochstrasser. Ultrafast relaxation and 2D IR of the aqueous trifluorocarboxylate ion. *J. Chem. Phys.*, 132(4):044501, 2010.

[129] J. B. Milne and T. J. Parker. Dissociation constant of aqueous trifluoroacetic acid by cryoscopy and conductivity. *J. Solution Chem.*, 10(7):479–487, 1981.

[130] G. Winkler, P. Wolschann, P. Briza, F. X. Heinz, and C. Kunz. Spectral properties of trifluoroacetic acid-acetonitrile gradient systems for separation of picomole quantities of peptides by reversed-phase high-performance liquid chromatography. *J. Chromatogr., A*, 347(0):83–88, 1985.

[131] A. Apffel, S. Fischer, G. Goldberg, P. C. Goodley, and F. E. Kuhlmann. Enhanced sensitivity for peptide mapping with electrospray liquid chromatography-mass spectrometry in the presence of signal suppression due to trifluoroacetic acid-containing mobile phases. *J. Chromatogr., A*, 712(1):177–190, 1995.

[132] D. S. King, C. G. Fields, and G. B. Fields. A cleavage method which minimizes side reactions following Fmoc solid phase peptide synthesis. *Int. J. Pept. Protein Res.*, 36(3):255–266, 1990.

[133] V. Dötsch, G. Wider, G. Siegal, and K. Wüthrich. Interaction of urea with an unfolded protein. the DNA-binding domain of the 434-repressor. *FEBS Lett.*, 366(1):6–10, 1995.

[134] Y. Goto, N. Takahashi, and A. L. Fink. Mechanism of acid-induced folding of proteins. *Biochemistry*, 29(14):3480–3488, 1990.

[135] C.L. Shen, M.C. Fitzgerald, and R.M. Murphy. Effect of acid predissolution on fibril size and fibril flexibility of synthetic beta-amyloid peptide. *Biophys. J.*, 67(3):1238–1246, 1994.

[136] K. Kwak, S. Park, I. J. Finkelstein, and M. D. Fayer. Frequency-frequency correlation functions and apodization in two-dimensional infrared vibrational echo spectroscopy: A new approach. *J. Chem. Phys.*, 127(12):–, 2007.

[137] S. Woutersen and P. Hamm. Structure determination of trialanine in water using polarization sensitive two-dimensional vibrational spectroscopy. *J. Phys. Chem. B*, 104(47):11316–11320, 2000.

[138] M. T. Zanni, N.-H. Ge, Y. S. Kim, and R. M. Hochstrasser. Two-dimensional IR spectroscopy can be designed to eliminate the diagonal peaks and expose only the crosspeaks needed for structure determination. *Proc. Nat. Sci. U.S.A*, 98(20):11265–11270, 2001.

[139] J. E. Donald, D. W. Kulp, and W. F. DeGrado. Salt bridges: Geometrically specific, designable interactions. *Proteins: Structure, Function, and Bioinformatics*, 79(3):898–915, 2011.

[140] A. Huerta-Viga, S. Amirjalayer, S. R. Domingos, H. Meuzelaar, A. Rupenyan, and S. Woutersen. The structure of salt bridges between Arg^+ and Glu^- in peptides investigated with 2D-IR spectroscopy: Evidence for two distinct hydrogen-bond geometries. *J. Chem. Phys.*, 142(21):212444, 2015.

[141] A. J. Markvoort, H. M. M. ten Eikelder, P. A. J. Hilbers, T. F. A. de Greef, and E. W. Meijer. Theoretical models of nonlinear effects in two-component cooperative supramolecular copolymerizations. *Nat. Commun.*, 2:509, 2011.

[142] E. Yashima, K. Maeda, and Y. Okamoto. Memory of macromolecular helicity assisted by interaction with achiral small molecules. *Nature*, 399(6735):449–451, 1999.

[143] X. Huang, C. Li, S. Jiang, X. Wang, and M. Zhang, B.and Liu. Self-assembled spiral nanoarchitecture and supramolecular chirality in langmuir-blodgett films of an achiral amphiphilic barbituric acid. *J. Am. Chem. Soc.*, 126(5):1322–1323, 2004.

[144] Y.-H. Chen, J. T. Yang, and H. M. Martinez. Determination of the secondary structures of proteins by circular dichroism and optical rotatory dispersion. *Biochemistry*, 11(22):4120–4131, 1972.

[145] G. Holzwarth and P. Doty. The ultraviolet circular dichroism of polypeptides. *J. Am. Chem. Soc.*, 87(2):218–228, 1965.

[146] L. A. Nafie, T. A. Keiderling, and P. J. Stephens. Vibrational circular dichroism. *J. Am. Chem. Soc.*, 98(10):2715–2723, 1976.

[147] R. A. G. D. Silva, J. Kubelka, P. Bour, S. M. Decatur, and T. A. Keiderling. Site-specific conformational determination in thermal unfolding studies of helical peptides using vibrational circular dichroism with isotopic substitution. *Proc. Nat. Sci. U.S.A*, 97(15):8318–8323, 2000.

[148] T. B. Freedman, R. K. Cao, X.and Dukor, and L. A. Nafie. Absolute configuration determination of chiral molecules in the solution state using vibrational circular dichroism. *Chirality*, 15(9):743–758, 2003.

[149] D. Kurouski, R. A. Lombardi, R. K. Dukor, I. K. Lednev, and L. A. Nafie. Direct observation and pH control of reversed supramolecular chirality in insulin fibrils by vibrational circular dichroism. *Chem. Commun.*, 46:7154–7156, 2010.

[150] L. D. Barron, M. P. Bogaard, and A. D. Buckingham. Raman scattering of circularly polarized light by optically active molecules. *J. Am. Chem. Soc.*, 95(2):603–605, 1973.

[151] L.D. Barron, L. Hecht, E.W. Blanch, and A.F. Bell. Solution structure and dynamics of biomolecules from raman optical activity. *Prog. Biophys. Mol. Biol.*, 73(1):1–49, 2000.

[152] I. H. McColl, E. W. Blanch, L. Hecht, N. R. Kallenbach, and L.D. Barron. Vibrational raman optical activity characterization of poly(L-proline) II helix in alanine oligopeptides. *J. Am. Chem. Soc.*, 126(16):5076–5077, 2004.

[153] S. R. Domingos, A. Huerta-Viga, L. Baij, S. Amirjalayer, D. A. E. Dunnebier, A. J. C. Walters, M. Finger, L. A. Nafie, B. de Bruin, W. J. Buma, and S. Woutersen. Amplified vibrational circular dichroism as a probe of local biomolecular structure. *J. Am. Chem. Soc.*, 136(9):3530–3535, 2014.

[154] T. Petralli-Mallow, T. M. Wong, J. D. Byers, H. I. Yee, and J. M. Hicks. Circular dichroism spectroscopy at interfaces: a surface second harmonic generation study. *J. Phys. Chem.*, 97(7):1383–1388, 1993.

[155] J. D. Byers, H. I. Yee, T. Petralli-Mallow, and J. M. Hicks. Second-harmonic generation circular-dichroism spectroscopy from chiral monolayers. *Phys. Rev. B*, 49:14643–14647, 1994.

[156] J. A. Giordmaine. Nonlinear optical properties of liquids. *Phys. Rev.*, 138:A1599–A1606, 1965.

[157] X. D. Zhu, Hajo Suhr, and Y. R. Shen. Surface vibrational spectroscopy by infrared-visible sum frequency generation. *Phys. Rev. B*, 35:3047–3050, 1987.

[158] M. Oh-e, H. Yokoyama, S. Yorozuya, K. Akagi, M. A. Belkin, and Y. R. Shen. Sum-frequency vibrational spectroscopy of a helically structured conjugated polymer. *Phys. Rev. Lett.*, 93:267402, 2004.

[159] J. Wang, X. Chen, M. L. Clarke, and Z. Chen. Detection of chiral sum frequency generation vibrational spectra of proteins and peptides at interfaces in situ. *Proc. Nat. Sci. U.S.A*, 102(14):4978–4983, 2005.

[160] L. Fu, G. Ma, and E. C. Y. Yan. In situ misfolding of human islet amyloid polypeptide at interfaces probed by vibrational sum frequency generation. *J. Am. Chem. Soc.*, 132(15):5405–5412, 2010.

[161] L. Fu, J. Liu, and E. C. Y. Yan. Chiral sum frequency generation spectroscopy for characterizing protein secondary structures at interfaces. *J. Am. Chem. Soc.*, 133(21):8094–8097, 2011.

[162] L. Fu, D. Xiao, Z. Wang, V. S. Batista, and E. C. Y. Yan. Chiral sum frequency generation for in situ probing proton exchange in antiparallel β-sheets at interfaces. *J. Am. Chem. Soc.*, 135(9):3592–3598, 2013.

[163] Z. Ganim, H. S. Chung, A. W. Smith, L. P. DeFlores, K. C. Jones, and A. Tokmakoff. Amide I two-dimensional infrared spectroscopy of proteins. *Acc. Chem. Res.*, 41(3):432–441, 2008.

[164] M. L. Schlossman and A. M. Tikhonov. Molecular ordering and phase behavior of surfactants at water-oil interfaces as probed by X-ray surface scattering. *Annu. Rev. Phys. Chem.*, 59(1):153–177, 2008.

[165] R. Superfine, J. Y. Huang, and Y. R. Shen. Phase measurement for surface infrared–visible sum-frequency generation. *Opt. Lett.*, 15(22):1276–1278, 1990.

[166] V. Ostroverkhov, G. A. Waychunas, and Y. R. Shen. New information on water interfacial structure revealed by phase-sensitive surface spectroscopy. *Phys. Rev. Lett.*, 94:046102, 2005.

[167] N. Ji, V. Ostroverkhov, C.-Y. Chen, and Y.-R. Shen. Phase-sensitive sum-frequency vibrational spectroscopy and its application to studies of interfacial alkyl chains. *J. Am. Chem. Soc.*, 129(33):10056–10057, 2007.

[168] I. V. Stiopkin, H. D. Jayathilake, A. N. Bordenyuk, and Al. V. Benderskii. Heterodyne-detected vibrational sum frequency generation spectroscopy. *J. Am. Chem. Soc.*, 130(7):2271–2275, 2008.

[169] S. Nihonyanagi, S. Yamaguchi, and T. Tahara. Direct evidence for orientational flip-flop of water molecules at charged interfaces: A heterodyne-detected vibrational sum frequency generation study. *J. Chem. Phys.*, 130(20):204704, 2009.

[170] R. E. Pool, J. Versluis, E. H. G. Backus, and M. Bonn. Comparative study of direct and phase-specific vibrational sum-frequency generation spectroscopy: Advantages and limitations. *J. Phys. Chem. B*, 115(51):15362–15369, 2011.

[171] M. Okuno and T.-a. Ishibashi. Chirality discriminated by heterodyne-detected vibrational sum frequency generation. *J. Phys. Chem. Lett.*, 5(16):2874–2878, 2014.

[172] M. Okuno and T.-a. Ishibashi. Heterodyne-detected achiral and chiral vibrational sum frequency generation of proteins at air/water interface. *J. Phys. Chem. C*, 119(18):9947–9954, 2015.

[173] E. C. Y. Yan, L. Fu, Z. Wang, and W. Liu. Biological macromolecules at interfaces probed by chiral vibrational sum frequency generation spectroscopy. *Chem. Rev.*, 114(17):8471–8498, 2014.

[174] A. J. Moad and G. J. Simpson. A unified treatment of selection rules and symmetry relations for sum-frequency and second harmonic spectroscopies. *J. Phys. Chem. B*, 108(11):3548–3562, 2004.

[175] G. J. Simpson. Molecular origins of the remarkable chiral sensitivity of second-order nonlinear optics. *Chem. Phys. Chem.*, 5(9):1301–1310, 2004.

[176] N. Ji, V. Ostroverkhov, M. Belkin, Y.-J. Shiu, and Y.-R. Shen. Toward chiral sum-frequency spectroscopy. *J. Am. Chem. Soc.*, 128(27):8845–8848, 2006.

[177] M. M. Harding, L. G. Ward, and A. D. J. Haymet. Type I antifreeze proteins. *Euro. J. Biochem.*, 264(3):653–665, 1999.

[178] G. L. Fletcher, C. L. Hew, and P. L. Davies. Antifreeze proteins of teleost fishes. *Annu. Rev. Physiol.*, 63(1):359–390, 2001.

[179] X. Zhuang, P. B. Miranda, D. Kim, and Y. R. Shen. Mapping molecular orientation and conformation at interfaces by surface nonlinear optics. *Phys. Rev. B*, 59:12632–12640, 1999.

[180] F. Sicheri and D. S. C. Yang. Ice-binding structure and mechanism of an antifreeze protein from winter flounder. *Nature*, 375(6530):427–431, 1995.

[181] M. A. Belkin, Y. R. Shen, and R. A. Harris. Sum-frequency vibrational spectroscopy of chiral liquids off and close to electronic resonance and the antisymmetric raman tensor. *J. Chem. Phys.*, 120(21):10118–10126, 2004.

[182] N. Bloembergen and P. S. Pershan. Light waves at the boundary of nonlinear media. *Phys. Rev.*, 128:606–622, 1962.

[183] K. Kemnitz, K. Bhattacharyya, J.M. Hicks, G.R. Pinto, B. Eisenthal, and T.F. Heinz. The phase of second-harmonic light generated at an interface and its relation to absolute molecular orientation. *Chem. Phys. Lett.*, 131(4-5):285–290, 1986.

[184] R. B. Sutton, D. Fasshauer, R. Jahn, and A. T. Brunger. Crystal structure of a SNARE complex involved in synaptic exocytosis at 2.4 Å resolution. *Nature*, 395(6700):347–353, 1998.

[185] Q. Chen and N. V. Richardson. Enantiomeric interactions between nucleic acid bases and amino acids on solid surfaces. *Nat. Mater.*, 2(5):324–328, 2003.

[186] R. Fasel, M. Parschau, and K.-H. Ernst. Amplification of chirality in two-dimensional enantiomorphous lattices. *Nature*, 439(7075):449–452, 2006.

[187] V.G. Dmitriev, G.G. Gurzadyan, and D.N. Nikogosyan. Handbook of Nonlinear Optical Crystals. Springer-Verlag, 1990.

[188] F. Zernike and J. E. Midwinter. Applied Nonlinear Optics. John Wiley & Sons, 1973.

[189] H. Chao, M. E. Houston, R. S. Hodges, C. M. Kay, B. D. Sykes, M. C. Loewen, P. L. Davies, and F. D. Sönnichsen. A diminished role for hydrogen bonds in antifreeze protein binding to ice. *Biochemistry*, 36(48):14652–14660, 1997.

[190] D. Wen and R. A. Laursen. A D-antifreeze polypeptide displays the same activity as its natural L-enantiomer. *FEBS Lett.*, 317(1,2):31–34, 1993.

[191] K. Meister, S. Strazdaite, A. L. DeVries, S. Lotze, L. L. C. Olijve, I. K. Voets, and H. J. Bakker. Observation of ice-like water layers at an aqueous protein surface. *Proc. Nat. Sci. U.S.A*, 111(50):17732–17736, 2014.

8 Summary

In this thesis, the molecular dynamics of water and biological (model) systems have been studied with advanced nonlinear optical techniques. In Chapters 4 - 5, the technique of femtosecond mid-infrared pump probe spectroscopy has been used to study the energy transfer and the reorientational dynamics of water molecules in solutions containing different solutes. In Chapters 6, two-dimensional infrared (2D-IR) spectroscopy has been used to study the energy transfer dynamics between vibrational marker modes of the protein backbone of an antifreeze protein. In Chapter 7, the same technique was used to determine the preferred geometry of a salt-bridge model complex in solution. The last chapter of this thesis shows how vibrational sum-frequency generation spectroscopy can be used to determine the absolute configuration of chiral (bio)molecules at interfaces. The main results of the individual chapters are summarized in the following.

Förster-type energy transfer In Chapter 4, we study the vibrational relaxation dynamics of the OH-stretch vibration in aqueous sodium iodide solutions of different isotopic composition. For low fractions of hydrogen ($f_H = 0.04$), the vibrational relaxation of water-bound and iodide-bound HDO molecules occur on two distinctly different timescales. An increase of the hydrogen fraction leads to fast Förster-energy transfer of the vibrational excitation between the water molecules in the ionic hydration shells and the bulk water. For HDO molecules in the hydration shell of the anion the resonant energy transfer to H_2O molecules opens up a new vibrational relaxation channel that is much faster than the intrinsic vibrational relaxation. As a result, the vibrational energy relaxation of the anionic hydration shells is strongly accelerated. For $f_H > 0.25$, the Förster energy transfer becomes faster than the intrinsic vibrational relaxation rates of all the water species, and a single decay rate is observed that forms a weighted average of the relaxation rates of the different species. We find that the Förster energy transfer becomes somewhat slower at higher salt concentrations, which manifests itself as a decrease in the Förster radius from 2.5 ± 0.2 Å at 1m NaI to 2 ± 0.2 Å at 6m NaI, which is likely the result of the increase in average distance between the water molecules, as a result of the dilution of water due to the presence of Na^+ and I^- ions.

Water dynamics in aqueous DMSO and acetone solutions In Chapter 5, we study the vibrational energy relaxation and molecular reorientation dynamics of water molecules in water-DMSO and water-acetone mixtures. For both solutes and at low solute fractions, a fraction of water molecules is strongly slowed down in their reorientation dynamics as a result of

the hydrophobic methyl groups. For water-acetone, the fraction of slow water molecules is significantly smaller than for an aqueous solution of DMSO at the same solute concentration. This suggests that substantially *less* water molecules are exposed to the hydrophobic methyl groups of acetone when compared to a water-DMSO mixture of equal solute mole fraction. This observation is a strong indicator that acetone molecules have a tendency to aggregate and form nano-clusters already at low concentrations.
At high solute fractions, the water-bound water molecules in both water-acetone and water-DMSO mixtures show a very slow reorientation with a time constant $\gg$10 ps. A striking difference between the two mixtures is that the solute-bound water fraction is much smaller for water-acetone than for water-DMSO mixtures at solute fractions $X_{sol} > 0.4$, which indicates that water forms nano-confined water clusters in water-acetone mixtures. The water molecules that are weakly hydrogen bonded to the C=O group of acetone, show a relatively fast reorientation with a time constant that decreases with increasing X_{sol} to 2.96±0.05 ps at $X_{acet} = 0.9$, which is nearly as fast as the reorientation of the OD-group of water molecules in neat HDO:H_2O ($\tau_{rot} = 2.5$ ps). For water-DMSO mixtures the water molecules forming hydrogen bonds to the S=O group show a much slower reorientation with a time constant that decreases from 46±14 ps at $X_{DMSO} = 0.33$ to 12±2 ps at $X_{DMSO} = 0.95$. The large difference in reorientation time constant of the solute-bound water for DMSO and acetone can be explained from the fact that the hydrogen bond between water and the S=O group of DMSO is much stronger than the hydrogen bond between water and the C=O group of acetone.

The main topic of Chapters 6 - 8 is the determination of the conformation of biomolecules. Chapter 6 covers the dynamical aspects, namely the energy transfer between two vibrational modes associated with secondary structural elements of a protein, while Chapters 7 and 8 concern static aspects of molecular conformation. In Chapter 7, the structure of a salt-bridge, a type of ion-pair encountered in polypeptides formed between charge-bearing side chains of amino acids, is inferred from the coupling between the vibrations of the amino acid side chains. In Chapter 8, we show how non-linear optical spectroscopy can be used as a chirality-sensitive technique and allows for the distinction between molecules that are mirror images (enantiomers) of each other.

VIBRATIONAL ENERGY EXCHANGE IN A TYPE III AFP In Chapter 6 we report on a study of the vibrational dynamics of the amide I vibration of a type III antifreeze protein. In this study we found evidence for the presence of two distinct subbands with lifetimes of 1.09 ± 0.01 ps and 3.21 ± 0.02 ps. It was furthermore found that the two bands are coupled and exchange population with a rate of $k_{B\rightarrow A}$= (7.1 ± 0.2 ps)$^{-1}$. Based on this observation, we have assigned the observed components to the $\alpha(+)$ and $\alpha(-)$-modes of β-sheets, which are associated with the in-phase and out-of-phase movement, respectively, of amide oscillators on adjacent strands of the β-sheets. The population exchange is likely enabled by the fast, (sub-)picosecond conformational fluctu-

ations of the β-sheets. The exchange rate constant shows little variation over a temperature interval from 2 to 20°C. This finding indicates that the protein backbone is flexible, even at temperatures near the freezing point (3.8°C, D_2O), which might reconcile previous contradictory observations about the secondary structure content of this protein (by X-ray diffraction and circular dichroism).

MODEL SYSTEMS FOR PROTEIN SALT BRIDGES In Chapter 7, we study the structure and dynamics of model compounds for protein salt bridges, namely methylguanidinium ($MeGd^+$) and trifluoroacetate (TFA^-). For methylguanidinium we probe the CN stretching vibrations, for TFA^- we probe the antisymmetric COO stretching vibration. We find that $MeGd^+$ and TFA^- have a strong tendency to form salt-bridge complexes both for solutions in D_2O and DMSO. In these complexes the C=O groups of TFA^- form strong hydrogen bonds to two N–D groups of $MeGd^+$. In DMSO the formation of the salt bridge leads to a strong acceleration of the vibrational relaxation of the antisymmetric COO vibration of TFA^-, from 3.4±0.4 ps to 0.9±0.1 ps. The anisotropy of the cross peaks of the 2D-IR spectrum shows that the transition dipole moments of the antisymmetric ν_{COO} mode of TFA^- and the CN stretching vibration at 1620 cm^{-1} are oriented at an angle of $\theta \approx 90°$. This CN mode involves the stretching of the CN bond to the $NDCH_3$ group in opposite phase to the symmetric stretching of the two CN bonds to the ND_2 groups of the $MeGd^+$ ion. This result shows that the salt-bridge complex of $MeGd^+$ and TFA^- has a preferred bidentate end-on configuration in which the two C=O groups of TFA^- form strong hydrogen bonds to the two ND_2 groups of $MeGd^+$.

CHIRALITY AT INTERFACES The last chapter of this thesis concerns the discrimination of enantiomeric molecules with high surface-specificity. We have used the technique of vibrational sum-frequency generation (VSFG) to study an interfacial layer of the (L)- and (D)-forms of an α-helical peptide with a polarization combination that selectively probes chiral molecules. The real and imaginary part of the second-order susceptibility $\chi^{(2)}$ are determined by an interferometric detection scheme, and the complex nature of $\chi^{(2)}$ directly reflects the absolute configuration of the chiral molecules. By comparison of the phase of the detected sum-frequency light with reference sum-frequency light with a well-known phase, generated from a z-cut quartz crystal, it is unambiguously determined that the signal originates from interfacial molecules. The method allows for the distinction between surface bound type I antifreeze peptides with left- and right-handed helices, and generally allows to distinguish enantiomers of chiral molecules with surface specificity, which up to now could not be achieved with other spectroscopic techniques.

Samenvatting

In dit proefschrift hebben we de moleculaire dynamica van water en biologische (model) systemen bestudeerd met geadvanceerde niet-lineaire optische technieken. In hoofstukken 4 - 5 hebben we femtoseconde infrarood pomp-probe spectroscopie gebruikt om de energieoverdracht en het reoriënteren van watermoleculen in oplossingen met verschillende opgeloste stoffen te bestuderen. In hoofdstuk 6 hebben we tweedimensionale infrarood spectroscopie gebruikt om de snelheid van energieoverdracht tussen C=O-groepen in de ruggengraat van een antivrieseiwit te bestuderen. In hoofdstuk 7 werd dezelfde techniek gebruikt om de geometrie van een zoutbrug model complex in oplossing te bepalen. Het laatste hoofdstuk van dit proefschrift laat zien hoe som-frequentie generatie spectroscopie kan worden toegepast om de absolute configuratie van chirale (bio) moleculen aan grensvlakken te bepalen. De belangrijkste resultaten van de afzonderlijke hoofdstukken zijn samengevat in het volgende.

Förster-type energieoverdracht In hoofdstuk 4 hebben we het relaxatiemechanisme van de OH-rekvibratie in waterige natriumjodide (NaI) oplossingen met verschillende isotopenverhoudingen bestudeerd. We vinden dat bij een lage fractie van waterstofatomen de vibratierelaxatie op twee verschillende tijdschalen plaatsvindt. Een verhoging van de waterstoffractie leidt tot een snelle Förster-energieoverdracht van de vibrationele excitatie tussen de watermoleculen in de solvatieschil van de I^- ionen en watermoleculen in de bulkfase. De resonante energieoverdracht naar H_2O moleculen vormt een extra relaxatiemechanisme voor HDO moleculen in de hydratatieschil van de I^- ionen, wat tot een versnelling van van de relaxatie leidt. Voor $f_H > 0.25$ wordt de Förster-energieoverdracht sneller dan de intrinsieke vibratierelaxatie, waardoor een enkele snelheidsconstante wordt waargenomen die een gewogen gemiddelde is van de verschillende soorten watermoleculen. We hebben waargenomen dat de Förster-energieoverdracht langzamer wordt als de zoutconcentratie verhoogd wordt. Dit leidt tot een vermindering van de Förster radius van 2.5 ± 0.2 Å voor een oplossing met een zoutconcentratie van 1m NaI tot 2 ± 0.2 Å voor een oplossing met 6m NaI. Dat is waarschijnlijk het resultaat van de toename van de gemiddelde afstand tussen de watermoleculen, welke op zijn beurt weer het gevolg is van de aanwezigheid van de Na^+ and I^- ionen.

De dynamica van water moleculen in waterige oplossingen van DMSO en aceton In hoofdstuk 5 beschrijf ik een studie van de dynamica van de vibratierelaxatie en reoriëntatie van watermoleculen in water-DMSO en water-aceton mengsels. We vinden dat de reoriëntatie van een deel van de watermoleculen in allebei de oplossingen sterk wordt vertraagd. Bij lage concen-

traties van de opgeloste stoffen vinden we dat de vertraging van de reoriëntatie wordt veroorzaakt door de hydrophobe methylgroepen. In oplossingen van aceton in water is de fractie langzaam water duidelijk lager dan in oplossingen van DMSO in water van dezelfde concentratie. Hieruit volgt dat minder watermoleculen worden beïnvloed door de hydrophobe methylgroepen van aceton dan door de methylgroepen van DMSO. Deze waarneming wijst erop dat acetonmoleculen al bij lage concentraties de neiging hebben om nano-clusters te vormen.
Het aantal watermoleculen dat met een waterstofbrug gebonden is aan het opgeloste molecuul is aanmerkelijker lager in oplossingen van aceton dan in oplossingen van DMSO. Dit duidt erop dat water nano-clusters vormt in water-aceton mengsels. De watermoleculen, die zwak waterstof gebrugd zijn met de C=O-groep van aceton, tonen een relatief snelle reoriëntatie met een tijdsconstante die afneemt met toenemende X_{sol} tot 2.96±0.05 ps voor $X_{acet} = 0.9$. Dat is bijna net zo snel als de reoriëntatie van de OD-groep van watermoleculen in een pure HDO:H_2O oplossing ($\tau_{rot} = 2.5$ ps). In water-DMSO mengsels hebben de watermoleculen die met een waterstofbrug aan de S=O-groep gebonden zijn, een veel tragere reoriëntatie met een tijdsconstante die afneemt van 46±14 ps bij $X_{DMSO} = 0.33$ tot 12±2 ps bij $X_{DMSO} = 0.95$. Het grote verschil in reoriëntatietijdsconstante tussen watermoleculen die aan DMSO gebonden zijn, en watermoleculen die aan aceton gebonden zijn, kan worden verklaard uit het feit dat de waterstofbrug tussen water en DMSO veel sterker is dan de waterstofbrug tussen water en de C=O-groep van aceton.

Het centrale thema van hoofdstukken 6 - 8 is de bepaling van de conformatie van biomoleculen. Hoofdstuk 6 beschrijft de dynamica van de energieoverdracht tussen vibraties die gerelateerd zijn aan de secundaire stuktuur van eiwitten. In hoofdstuk 7 worden experimenten beschreven die laten zien hoe de ruimtelijke structuur van een zoutbrug eruitziet. In het laatste hoofdstuk worden experimenten beschreven waaruit blijkt hoe niet-lineaire spectroscopie kan worden gebruikt om spiegelbeeldisomeren (enantiomeren) van elkaar te onderscheiden.

ENERGIEOVERDRACHT IN EEN ANTIVRIESEIWIT In hoofdstuk 6 hebben we de vibratiedynamica van de amide I trillingen van een type III antivrieseiwit bestudeerd. De resultaten lieten zien dat er twee verschillende amide I trillingen zijn met verschillende levensduren van 1.09 ± 0.01 ps en 3.21 ± 0.02 ps. Daarnaast hebben we waargenomen dat er energieoverdacht tussen deze twee trillingen plaatsvindt met een tijdsconstante van 7.1 ± 0.2 ps. Op basis van deze waarnemingen kunnen we de twee trillingen aan de $\alpha(+)$ en de $\alpha(-)$-modes van β-sheets toekennen. Deze vibraties vormen de in-fase en uit-fase beweging van amide I oscillatoren. De energieoverdracht wordt mogelijk gemaakt door snelle fluctuaties van de β-sheet conformatie op een tijdschaal van (sub)picoseconden. De snelheid van de energieoverdracht hangt nauwelijks af van de temperatuur in een interval van 2 tot 20°C. Dit resultaat wijst erop dat de ruggengraat van het eiwit heel flexibel is, zelfs bij temperaturen nabij het vriespunt. Deze interpretatie wordt ondersteund door de afwezigheid van meetbare secundaire structuur

in circular dichroïsme spectroscopie.

MODEL SYSTEEM VOOR ZOUTBRUGGEN IN EIWITTEN In hoofdstuk 7 beschrijf ik hoe we met tweedimensionale infrarood spectroscopie methylguanidinium ($MeGd^+$) en trifluoroacetate (TFA^-) hebben bestudeerd. Dit systeem vormt een model voor de zoutbrug interacties die in eiwitten een belangrijke rol spelen in de bepaling van de secundaire structuur. We zagen dat $MeGd^+$ en TFA^- in DMSO en in water een sterke neiging tot vorming van zoutbruggen hebben, waarbij de C=O-groepen van TFA^- een sterke waterstofbrug met de twee N–D-groepen van $MeGd^+$ vormen. De vorming van dit complex leidt tot een versnelling van de vibratierelaxatie van de antisymmetrische COO strekvibratie van TFA^-, de levensduur neemt af van 3.4±0.4 ps naar 0.9±0.1 ps. Uit de anisotropie van de cross-peaks in het tweedimensionale IR-spectrum hebben we de hoek tussen de overgangsdipoolmomenten van de antisymmetrische COO strekvibratie en de CN strekvibratie met een resonantie frequentie van 1620 cm^{-1} bepaald. We vonden dat de overgangsdipoolmomenten van deze vibraties onder een hoek van $\theta \approx 90°$ met elkaar staan. Dit resultaat toont aan dat het complex uit $MeGd^+$ en TFA^- bij voorkeur een geometrie aanneemt, waarin de twee C=O-groepen van TFA^- waterstofbruggen met de twee ND_2-groepen van $MeGd^+$ vormen (een zogenoemde "end-on" configuratie).

CHIRALITEIT AAN GRENSVLAKKEN Het laatste hoofdstuk van dit proefschrift gaat over het onderscheiden van spiegelbeeldisomeren (enantiomeren) aan grensvlakken. Met behulp van vibrationele som-frequentie generatie (VSFG) spectroscopie hebben we een monolaag van een α-helicale peptide aan het lucht-water grensvlak bestudeerd. De peptides zijn opgebouwd uit of (L)- of (D)-aminozuren. Wij gebruikten een polarisatiecombinatie die alleen gevoelig is voor chirale moleculen en geen signal opleveren van achirale moleculen zoals bijvoorbeeld water. Met behulp van interferometrische detectie hebben we het reele en het imaginaire deel van de $\chi^{(2)}$-tensor bepaald. Deze waarden zijn direct gerelateerd aan de absolute conformatie van het chirale molecuul. Door de fase van het gedetecteerde SFG-licht te vergelijken met de fase van het SFG-licht gegenereerd met behulp van een z-gesneden quartz kristal, kon ondubbelzinning worden vastgesteld dat het signaal van peptide moleculen aan het water-lucht grensvlak afkomstig is, en niet van moleculen in de bulk van de oplossing. Daarmee hebben we laten zien dat onze methode kan worden gebruikt om peptides met links- en rechtsdraaiende helices aan grensvlakken te onderscheiden. Dit is niet mogelijk met andere spectroscopische methoden.

Acknowledgements

This thesis is the product of several years of work and it could not have been written without the help of many people, to whom I would like to express my gratitude.
First off, I would like to thank my supervisor Huib Bakker. I have learned a lot from you during this time, from developing a critical eye for experimental data to developing a more pragmatic approach towards getting things done. Thank you for leaving me freedom in developing my own projects, and more importantly not losing trust in them.
The initial steps during an experimental PhD are always accompanied by a lot of pitfalls, and I'm therefore very grateful to those who taught me the first steps in the world of ultrafast spectroscopy and nonlinear optics. In particular, I would like to thank Nuria, Ellen and Sietse for their help in the lab during my first months at Amolf. I'd like to thank Matthijs Panman for teaching me a lot of valuable tricks in setting up the 2D-IR experiments. Jan, thank you for your advice on all aspects of the SFG-spectroscopy and our good collaboration on the chiral SFG-project. Thanks also for keeping our laser systems always in good shape. Artem, thank you for always finding a way to efficiently share the beam-time for the Viktor-setup. Hinco, thank you for designing and fabricating countless invaluable items & gadgets for the lab, from rotating sample cells to the most unusual temperature controllers. Many experiments would not have been possible without them! I would also like to thank Ilja Voets and Luuk Olijve from the TU/e for our collaborations on the antifreeze-projects, which I really enjoyed and which resulted in Chapters 6 and 8 of this thesis.
I would like to thank the members of the Bakker-group that I have had the chance to work with over the past years for the good atmosphere and the cakes, cookies & drinks that were shared on various occasions: Carien, Christina, Eliane, Klaas-Jan, Konrad, Liyuan, Łukasz, Niklas, Simona, Wilbert. Thanks also to the members of Sander Woutersen's group at the UvA, Adriana, Heleen, Sergio, Steven, Tibert, for our joint work discussions, which were always enjoyable and from which I learned a great deal, and to the members of Yves's group, Lianne, Niels & Oleg, for sharing their knowledge and experience (and setup when needed). I wish you all the best in the future!
I have also benefitted a lot from Amolf's support departments: thank you to the E & I guys, in particular Marco and Sjoerd for developing the control software for our setups, as well as Henk, Duncan and Idsard for solving all kind of electronics-related problems. Thanks also to Juanita, Lenny & Valeska for taking care of all housing-related issues.
There's certainly more to life than work, and I am very grateful to the people

that provided the distraction from science that was sometimes badly needed. I would like to thank my friends, close-by and far, for the good times spent together, be it on evenings & weekends or on holidays, the annual snowboard-trips and many other occasions. It made life a lot more fun and often helped me to put things in perspective. Thank you Felipe, Jochen, Jeanette, Lutz, Nuria, Oleg, Cristina, Simona, Sophie, Chris, Christoph, Jogi, Simon, Olli, Jens, Tobi, Christian, Florian, Frank, Federico. To my flatmates from the Middenweg, Jochen, Lutz and Nicola: thank you for providing a friendly and relaxed living atmosphere. Thanks also to my Thursday-evening-football buddies for the many enjoyable matches.
Before I close, I would like to thank Zofia for her patience and encouragement during the times we had together, and I am very grateful to my parents for their support throughout the years. Mama, die restlichen 150 Seiten sind vielleicht ein wenig unverständlich, trotzdem hast Du zum Gelingen viel beigetragen und ich bin dir für Deine Unterstüztung sehr dankbar. Papa, danke auch Dir für Dein stetes Interesse an meiner Arbeit.